

DE-FG05-80ET-53088-661

IFSR #661

**Particle Dynamics and Collisionless Conductivity of the
Plasma Sheet in the Geomagnetic Tail**

(Dissertation)

JOSE VALENTE HERNANDEZ OCHOA
Institute for Fusion Studies
The University of Texas at Austin
Austin, Texas 78712

May 1994

PARTICLE DYNAMICS AND COLLISIONLESS CONDUCTIVITY OF THE PLASMA SHEET IN THE GEOMAGNETIC TAIL

by

JOSE VALENTE HERNANDEZ OCHOA, FIS.

Abstract

A recurrent theme in magnetospheric research is that of the origin and quantification of the finite, collisionless electrical conductivity of the central plasma sheet in the geomagnetic tail. Outside the quasineutral layer the charged particle orbits are described by the guiding center classical theory and the plasma dynamics is given by ideal MHD theory. In the interior region where the magnetic field is weak and rapidly changing in direction, the particle orbits are complex, nonadiabatic, and receive a net acceleration from the dawn to dusk electric field (E_y) over the correlation time τ_c . *Lyons and Speiser* [1985] take τ_c to be the time that the particles spend in the quasineutral layer and approximate this time by one half of the cyclotron period in the minimum of the magnetic field. On the other hand, *Horton and Tajima* [1990, 1991] take τ_c to be the finite velocity correlation time produced by intrinsic orbital stochasticity in the quasineutral layer. The present work develops the theory and applications of the decay of the velocity correlations approach. The spectral velocity correlations formalism is described and used to extend conductivity formulae to new regimes. The spectral velocity correlations formalism is shown to provide a systematic framework to derive conductivity formulae in collisionless plasmas and is particularly useful in situations when the charged particle motion is a mixture of both chaotic and integrable motion or when the motion is integrable, but it is impractical to perform an analytical calculation of the conductivity.

**PARTICLE DYNAMICS AND COLLISIONLESS
CONDUCTIVITY OF THE PLASMA SHEET
IN THE GEOMAGNETIC TAIL**

Approved by

Dissertation Committee:

Wendell Horton

Philip A. Uman

[Signature]

James W. VanDam

R. D. [Signature]

PARTICLE DYNAMICS AND COLLISIONLESS
CONDUCTIVITY OF THE PLASMA SHEET
IN THE GEOMAGNETIC TAIL

by

JOSE VALENTE HERNANDEZ OCHOA, FIS.

DISSERTATION

Presented to the Faculty of the Graduate School of

The University of Texas at Austin

in Partial Fulfillment

of the Requirements

for the Degree of

DOCTOR OF PHILOSOPHY

THE UNIVERSITY OF TEXAS AT AUSTIN

May, 1994

To my wife Verónica,
my son José Daniel,
and my parents Arnulfo and Alicia

Acknowledgments

I would like to thank my advisor Prof. Wendell Horton for his guidance, patience, inspiration, and support. He has certainly made an impression in the way I approach a new problem. Having worked for him has been both a privilege and a great pleasure.

I have also enjoyed my frequent discussions with Prof. Toshi Tajima. His rather different views have been very educational. I also thank Prof. Philip Morrison, Dr. James Van Dam, and Prof. Roger Broucke for their constant interest in the progress of my work and for having served on my dissertation committee.

I am very grateful to the Universidad Nacional Autónoma de México (UNAM) for awarding me a scholarship to pursue my graduate studies at The University of Texas. I would also like to thank the Institute for Fusion Studies for providing me with a research assistantship that allowed me to complete this work.

Going way back, during my UNAM years, I had the help and guidance of Mariano Bauer, Julio Herrera, and Marcos Rosenbaum. I am grateful to all of them. They left their marks on my career.

Many IFS staff members helped me at several stages of this work. I would like to specially thank Suzy Mitchell for the countless occasions she helped me with my \LaTeX writeups. I would also like to thank Ed Bailey for his assistance with computing.

Having reached this point has been a team effort. I thank my wife Verónica for her unconditional love and support, for having adjusted to my unusual schedule, and for our son. I would like to thank my parents Arnulfo and Alicia, who always encouraged me to search for a better education. Thanks to my brothers, sister, and family for their support. Thanks to my friends for their companionship.

JOSE VALENTE HERNANDEZ OCHOA

The University of Texas at Austin

May, 1994

Table of Contents

Acknowledgments	iv
Table of Contents	viii
List of Tables	ix
List of Figures	x
1. Chapter 1. Introduction and Magnetic Field Models	1
1.1 Introduction	1
1.2 Magnetic Field Models	7
1.2.1 Vlasov-Maxwell Equations	7
1.2.2 Harris Sheet Model	11
1.2.3 Parabolic-Like Magnetic Field Reversals	13
1.2.4 Sheared Parabolic Magnetic Field Reversals	19
2. Chapter 2. Particle Dynamics in Magnetic Field Reversals	21
2.1 Particle Dynamics in Straight Magnetic Field Reversals	21
2.1.1 Integration of the Equations of Motion	28
2.2 Particle Motion in Parabolic Magnetic Field Reversals: Chaotic Motion	33
2.2.1 Guiding Center Motion	35
2.2.2 Numerical Integration of the Motion, Current Sheet Ac- tion, and Orbit Classification	36

2.2.3	Surface of Section Plots and Orbit Classification	47
2.3	Liapunov Exponents	49
2.3.1	Tangent Flow	51
2.3.2	Benettin et al. Method	53
2.3.3	Standard Mapping	54
2.3.4	Hénon-Heiles System	58
2.3.5	Local Instability for Parabolic Field Reversals	60
2.4	Motion in Sheared Parabolic Magnetic Field Reversals	68
3.	Chapter 3. Decay of the Correlations, Power Spectrum, and Chaotic Motion	78
3.1	Velocity Correlations and Power Spectra for Single Particle Motion	79
3.2	Velocity Correlations and Power Spectrum in the Presence of Collisions	84
3.3	Decay of the Correlations and the Collisionless Conductivity in the Geomagnetic Tail	88
4.	Chapter 4. Collisionless Conductivity	93
4.1	The Dielectric Tensor	97
4.1.1	Longitudinal Response Function	99
4.1.2	Energy Dissipation and Stored Energy	100
4.2	Collisionless Conductivity in Magnetic Field Reversals	103
4.2.1	Conductivity Formula	110
4.2.2	Frequency Sum Rule	113
4.2.3	Summary	114
4.3	Collisionless Conductivity and Fluctuation Dissipation Relations	114
4.4	Conductivity for an Unmagnetized Plasma	119

4.4.1	Conductivity from Kubo's Formula	119
4.4.2	Conductivity from the Spectral Velocity Correlations Formalism	123
4.5	Kaufman Conductivity for Inhomogeneous Systems	125
5.	Chapter 5. Conductivity for the Central Plasma Sheet with Applications to Tearing Modes	129
5.1	Collisionless Conductivity for the Harris Sheet	129
5.2	Collisionless Conductivity for Parabolic-Like Magnetic Field Reversals	135
5.3	Collisionless Conductivity for Sheared Parabolic Magnetic Field Reversals	139
5.4	Results of Parametric Studies to Verify the $\mathbf{B}_y - \kappa$ Dependence of the Mobility Formula	149
6.	Chapter 6. Conclusions and Discussion	152
	References	156
	Vita	

List of Tables

1.1	Reference Parameters.	8
2.1	Expansion Rates for Instability Bursts.	66
5.1	Sensitivity of Numerical Results.	142
5.2	Low Frequency Limit of Correlation Time	145
5.3	Conductivities and Tearing Mode Growth Rates.	149

List of Figures

1.1	Cross section of the geomagnetic tail.	3
1.2	Straight magnetic field reversal	14
1.3	Parabolic field reversal.	15
1.4	Sheared parabolic field reversal.	20
2.1	Effective potential and phase space diagram for $qP_y > 0$	23
2.2	Effective potential and phase space diagram for $qP_y < 0$	24
2.3	Charged particle trajectories for straight field reversals.	26
2.4	Dispersion of orbital frequencies for straight magnetic field reversals.	32
2.5	Effective potential $V(x, z)$ for the parabolic field model.	38
2.6	Three-dimensional view of a trapped orbit in the modified Harris sheet model.	40
2.7	Planar projections of a trapped orbit in configuration space.	41
2.8	Three-dimensional view of a transient orbit.	42
2.9	Planar projections of a transient orbit in configuration space.	43
2.10	Three-dimensional view of a quasi-trapped orbit.	44
2.11	Planar projections of a quasi-trapped orbit in configuration space.	45
2.12	Plot of $f_C(k)$ for $k < 1$ and of $f_N(k)$ for $k > 1$	47

2.13	Surface of section plot for the parabolic field reversal.	48
2.14	Evolution of the separation vector $\delta\mathbf{y}(t)$ in phase space.	50
2.15	Numerical calculation of the largest Liapunov exponent.	54
2.16	Eigenvalues of \mathbf{K} for the standard mapping.	57
2.17	Potential U for the Hénon and Heiles problem.	59
2.18	Roots of the characteristic equation (2.111).	63
2.19	Local instability index $\nu_m^2(x, z)$ for parabolic field reversals.	64
2.20	Ensemble averaged exponential divergence rate.	67
2.21	Ring orbit in the sheared parabolic magnetic field of Eq. (2.126).	72
2.22	Surface of section plot for $B_y/B_z = 5$ and $\kappa = 0.18$	76
2.23	Surface of section plot for $B_y/B_z = 1$ and $\kappa = 0.18$	77
3.1	Single particle velocity correlation function and power spectrum for a ring orbit.	82
3.2	Single particle velocity correlation function and power spectrum for a cucumber orbit.	83
3.3	Velocity auto-correlation function and power spectrum for a par- ticle executing cyclotron motion.	86
3.4	Velocity auto-correlation function and power spectrum in the presence of collisions	87
3.5	Plot of $\langle \ln \hat{C}(\tau) \rangle$ as a function of $\ln(\omega_{bz}\tau)$	90
3.6	Plot of $\langle \hat{C}(\omega) \rangle$ as a function ω/ω_{bz}	92

4.1	Integration Contour for (4.38).	102
4.2	Conductivity for unmagnetized plasma.	124
5.1	Conductivity for the Harris sheet: $ z/L_z < 1$	131
5.2	Conductivity for the Harris sheet: $3 \leq z/L_z \leq 4$	133
5.3	Plot of $\tau_c(\omega; \kappa, b_y, b_z)$ as a function of b_y/b_z	143
5.4	Qualitative behavior of the conductivity of Eq. (5.40) for both ions and electrons.	147

Chapter 1

Chapter 1. Introduction and Magnetic Field Models

1.1 Introduction

The magnetosphere is the magnetic cavity formed around the Earth due to the interaction of the magnetized solar wind with the planetary dipolar magnetic field. In this interaction mass, momentum, and energy are transferred from the solar wind to the planetary field, stretching it in the direction of the solar wind.

The size and shape of the magnetosphere are determined by the balance between the Earth's magnetic energy density and the solar wind kinetic pressure. The shape of the magnetosphere is compressed on the day side and elongated on the night side.

The system of stretched field lines and plasma in the nightside magnetosphere is called the geomagnetic tail. The geomagnetic tail extends downstream beyond $200 R_E$, where $1 R_E = 6380$ km is the earth radius. The tail has a diameter of about $40 R_E$, and is filled with reversed magnetic fluxes with mean values of ± 20 nT. The geomagnetic tail plays a primordial role in the storage and release of energy. There are several regions in the magnetic tail. In particular, the lobe is the region of open field lines, the central plasma sheet (CPS) is the region of closed field lines, and the plasma sheet boundary layer is the region which separates the lobe and the CPS. A cross section view of

the magnetotail computed from a standard magnetic field model is shown in Fig. 1.1.

One of the most important problems in magnetospheric research is the origin and dynamics of magnetospheric substorms. Magnetospheric substorms are large scale disturbances of the magnetic field and of the currents in the magnetosphere-ionosphere system produced as a response to changes in the solar wind density, velocity, and magnetic field. The most evident manifestations of substorms are the auroral displays which occur at high ($\sim 70^\circ$) magnetic latitudes and during which a huge amount of power (10^{18} erg/sec) is delivered into the atmosphere. Based on measurements of fluctuations in the horizontal component of the Earth's magnetic field at ground stations located near the equator, three phases of a geomagnetic storm can be identified [Tsurutani and Gonzalez, 1994]. In the initial phase the deviation of the horizontal component from the ambient level increases to values of the order of tens of nanoTeslas with a time scale ranging from minutes to hours. In the main phase the deviation of the horizontal component reaches values of minus hundreds of nanoTeslas with a duration from half-hour up to several hours. In the recovery phase, which lasts from hours to a week, the field gradually returns to its ambient level.

At a human scale, magnetospheric substorms are important because the resulting fluctuating magnetic fields affect the performance of magnetometers (used in navigation systems and in geophysical exploration), and induce currents in power lines, train tracks, pipelines, etc., leading to equipment failures. In addition, the energized flows of magnetospheric ions and electrons heat the upper atmosphere, producing density changes which affect the perfor-

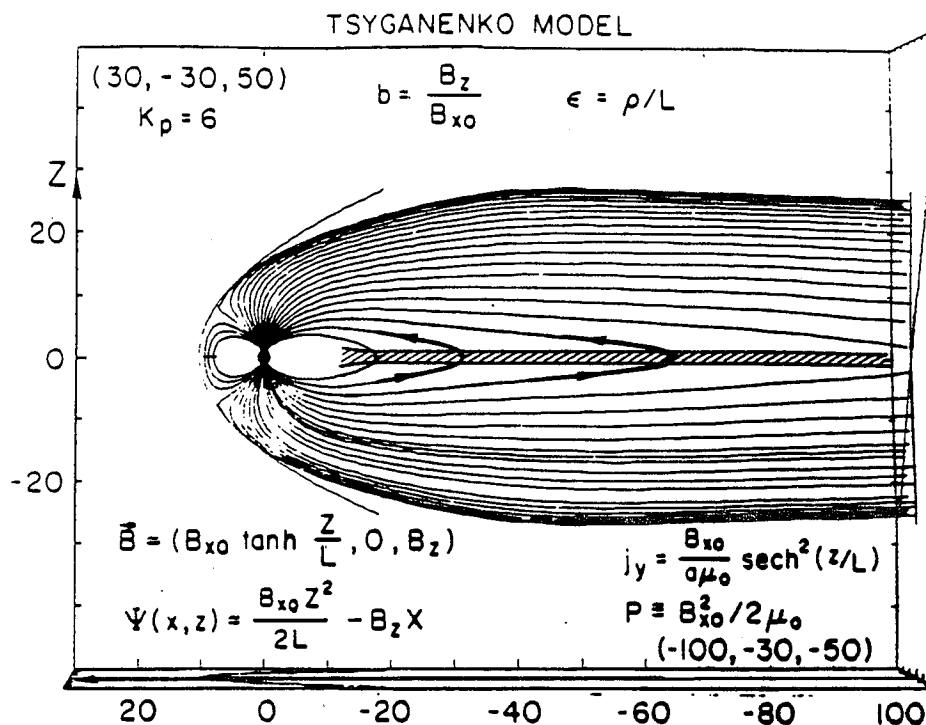


Figure 1.1: Cross section of the geomagnetic tail.

mance of radars and satellite communications and which can lead to changes in satellite orbits.

The development of magnetospheric substorms is associated with the appearance of a dawn-to-dusk electric field E_y and with the equatorward drift of the auroral arc. There are several physical processes associated with magnetospheric substorms. These processes include magnetic reconnection at the magnetopause and the geomagnetic tail, intensification and generation of ionospheric and field aligned currents, and convection and energization of magnetospheric plasmas.

There are several models for magnetospheric substorms (see *Lui* [1991])

and references therein for a review). The most popular and best developed substorm model is the near-Earth-neutral line model [eg., *Hones, 1979; Cowley, 1982*] and variations of that model. In the near-Earth-neutral line model, the magnetospheric disturbance is initiated by a southward turning of the interplanetary magnetic field (IMF) which merges with the northward magnetospheric field at the dayside magnetopause and forms a magnetic X -line. The open field lines are convected by the solar wind towards the geomagnetic tail, leading to an increase in the size and strength of the tail lobe, and to the formation of an X -line in the CPS with the subsequent energization of plasma in the vicinity of the X -point.

Magnetic reconnection or merging in the field reversal regions of the geomagnetic tail was first proposed by *Dungey [1961]*. Magnetic reconnection may happen as a consequence of the tearing instability, which was first considered by *Furth et al. [1963]* for resistive MHD. The possibility of collisionless tearing instability was suggested by *Coppi et al. [1966]*. Growth rates for resistive tearing modes consistent with substorm growth time scales require a magnetic Reynolds number $S = v_A L / \eta$ in the 100 – 300 range [*Birn and Hesse, 1990*]. These values of S require an anomalously low conductivity; however, the geomagnetic tail is a highly collisionless environment with collisional times $\tau_c \sim 1$ year and mean free paths from Coulomb collisions on the order of $\lambda_{mfp} \sim 10^9 R_E$. Thus, it is necessary to look for alternative sources of the collisionless resistivity.

Currently there are two approaches to looking for sources of the collisionless resistivity in the CPS: the wave turbulence approach and the particle dynamics approach. In the wave turbulence approach the momentum of the

particles is scattered by turbulent wave activity. In the particle dynamics approach the resistive time corresponds to the time during which the charged particles are coherently accelerated by the dawn-dusk electric field E_y .

Several turbulent wave processes have been suggested [*Huba et al.*, 1978; *Coroniti*, 1980; *Esarey and Molvig*, 1987] as possible candidates for the generation of a collisionless resistivity. These approaches include lower hybrid drift wave turbulence and broad band electrostatic noise. However, measurements from the ISEE 1 and ISEE 2 satellites have shown [*Anderson*, 1984] that turbulent wave activity is negligible at the center of the current sheet and that the wave amplitudes in the CPS are not enough to explain the expected reconnection rates.

Alternatively, from the particle dynamics point of view, there are several proposed models for the generation of the collisionless resistivity in the current sheet of the CPS. These models include the inertial or gyroresistivity of *Lyons and Speiser* [1985], where the resistive time is determined by the residence time of transient orbits in the current sheet, chaotic electron motion [*Martin*, 1986], and the decay of the velocity correlations from chaotic ion orbits [*Horton and Tajima* 1990].

The present work develops the formalism and extends to new regimes the decay of the velocity correlations approach of *Horton and Tajima* [1990, 1991a,b]. Here we present a systematic framework to derive conductivity formulae in collisionless plasmas. This approach is particularly useful in situations when the charged particle motion is chaotic or when the motion is integrable, but it is impractical to perform an analytic calculation of the conductivity. We show that the conductivity formulae obtained from the application of the

formalism to tail-like magnetic field reversals reduce to previous models in the appropriate limits. Then we apply the formalism to the derivation of a conductivity formula for the case of a sheared parabolic magnetic field reversal and use the resulting expression to estimate growth rates for collisionless tearing modes.

Current sheets and their resulting magnetic field reversals occur in both space (geomagnetic tail, magnetopause, solar flares, etc.) and laboratory (field reversal configuration) plasmas. In particular, the current sheet plasma of the central plasma sheet in the night-side geomagnetic tail plays a major role in energy storage and particle energization during magnetospheric substorms. In the next section we introduce several magnetic field models which are widely used in the literature to describe plasma behavior in the presence of current sheets. We divide these models into straight magnetic field reversals, parabolic-like field reversals, and sheared parabolic-like magnetic field reversals.

In Chapter 2 we discuss single particle dynamics in each one of the magnetic field models and present several tools (surface of section plots and Liapunov exponents) which are used in the study of chaotic particle dynamics.

In Chapter 3 the analogy between chaotic particle dynamics and collisional processes is discussed within the framework of velocity correlations and power spectra, and the decay of the velocity correlations approach for the derivation of the collisionless conductivity is introduced.

In Chapter 4 the spectral velocity correlations formalism is presented and applied to several well known cases, and its relationship to the fluctuation-dissipation theorem is established.

Finally, in Chapter 5 the formalism is applied to the study of the conductivity in tail-like magnetic field reversals. In particular, the collisionless conductivity for sheared parabolic field reversals is derived and applied to the estimation of tearing mode growth rates.

1.2 Magnetic Field Models

We are interested in modeling the transport properties of the plasma trapped in the field-reversal region of the nightside geomagnetic tail or central plasma sheet (CPS). In this work we use the so-called magnetospheric coordinate system with the x -axis along the Earth-Sun line and pointing towards the Sun, the y -axis pointing from dawn-to-dusk, and the z -axis along the south-north direction. Typical field and plasma parameters for the CPS in the mid-tail region ($x \sim 20 - 50 R_E$) are lobe field $B \approx B_x \sim 20$ nT, normal field $B_z \sim 1$ nT, particle density $n \sim 1 \text{ cm}^{-3}$, ion temperature $T_i \sim 1 - 10$ keV, and electron temperature $T_e \sim 0.1 - 1$ keV. We denote by L_x , L_y , and L_z the characteristic spatial scales of the plasma sheet along x , y , and z , respectively. In the mid-tail region, we take $L_x \sim 20 R_E$, $L_y \sim 40 R_E$, and $L_z \sim 1 R_E$. Thus, we assume that in equilibrium $\partial_x/\partial_z \sim L_z/L_x \ll 1$ and $\partial/\partial y = 0$.

A set of reference parameters typical of the geotail plasma and similar to those found in the literature are given in Table 1.1. Now we consider the traditional mathematical description of such a collisionless equilibrium.

1.2.1 Vlasov-Maxwell Equations

For collisionless plasmas the equilibrium distribution function $f_j(\mathbf{x}, \mathbf{v}, t)$, where j labels particle species, evolves according to the Vlasov equa-

Table 1.1: Reference Electromagnetic Field and Plasma Parameters.

Parameter	Value
B_{x0}	20 nT
B_z	1 nT
E_y	1 mV/m=1V/km
L_z	$R_E = 6380$ km
T_i	$T_i = T_e = 1$ keV
n	$B_{x0}^2/2\mu_0(T_i + T_e) = 0.5 \times 10^6$ m ⁻³
$2\pi/\omega_{cx0}$	3 s
$2\pi/\omega_{bz}$	20 s
$2\pi/\omega_{cz}$	1min
v_z	$E_y/B_{x0} = 50$ km/s
L_z/v_z	2 min
ϵ_i	$\rho_i/L_z = 0.0235$
κ_i	0.314
ϵ_e	$\rho_e/L_z = 0.000591$
κ_e	2.06

tion

$$\frac{\partial f_j}{\partial t} + \mathbf{v} \cdot \frac{\partial f_j}{\partial \mathbf{x}} + \frac{q_j}{m_j} (\mathbf{E} + \mathbf{v} \times \mathbf{B}) \cdot \frac{\partial f_j}{\partial \mathbf{v}} = 0. \quad (1.1)$$

The electric and magnetic fields $\mathbf{E}(\mathbf{x}, t)$ and $\mathbf{B}(\mathbf{x}, t)$ are determined self-consistently from Maxwell's equations

$$\nabla \cdot \mathbf{E} = \frac{1}{\epsilon_0} (\rho + \rho_{ext}), \quad (1.2)$$

$$\nabla \times \mathbf{E} = -\frac{\partial \mathbf{B}}{\partial t}, \quad (1.3)$$

$$\nabla \cdot \mathbf{B} = 0, \quad (1.4)$$

$$\nabla \times \mathbf{B} = \mu_0 (\mathbf{J} + \mathbf{J}_{ext}) + \frac{1}{c^2} \frac{\partial \mathbf{E}}{\partial t}, \quad (1.5)$$

where we have allowed for the possibility of having external charge and current sources, $\rho_{ext}(\mathbf{x}, t)$ and $\mathbf{J}_{ext}(\mathbf{x}, t)$. In practice, it is convenient to express the fields \mathbf{E} and \mathbf{B} in terms of the scalar potential $\Phi(\mathbf{x}, t)$ and the vector potential $\mathbf{A}(\mathbf{x}, t)$,

$$\mathbf{E} = -\nabla\Phi - \frac{\partial \mathbf{A}}{\partial t}, \quad (1.6)$$

$$\mathbf{B} = \nabla \times \mathbf{A}. \quad (1.7)$$

In the following sections we will use the Coulomb gauge which satisfies $\nabla \cdot \mathbf{A} = 0$.

The Vlasov-Maxwell equations are nonlinear because $f_j(\mathbf{x}, \mathbf{v}, t)$ is modified by the self-generated fields, which in turn evolve as the distribution function changes. The plasma charge and current densities, $\rho(\mathbf{x}, t)$ and $\mathbf{J}(\mathbf{x}, t)$, are given in terms of the distribution function by

$$\rho = \sum_j q_j \int d^3v f_j \quad (1.8)$$

and

$$\mathbf{J} = \sum_j q_j \int d^3v \mathbf{v} f_j. \quad (1.9)$$

When solutions to the Vlasov equation (1.1) are sought, it is convenient to interpret the left side of Eq. (1.1) as the total time derivative of f_j along a particle orbit; that is, Eq. (1.1) can be written as

$$\frac{d}{dt} f_j(\mathbf{x}, \mathbf{v}, t) = 0. \quad (1.10)$$

Suppose now that f_j is a function of the constants of motion $\{C_i(\mathbf{x}, \mathbf{v}, t)\}$ along the trajectory of the particle. Then,

$$\frac{d}{dt} f_j(\{C_i(\mathbf{x}, \mathbf{v}, t)\}) = \sum_i \frac{\partial f_j}{\partial C_i} \frac{dC_i}{dt} = 0, \quad (1.11)$$

which is the Vlasov equation. Thus, any distribution that is a function of the constants of the motion is a solution of the Vlasov equation.

We are interested in steady-state solutions to the Vlasov-Maxwell system for tail-like magnetic field reversals in the absence of external sources. In this case the equilibrium analysis of the Vlasov-Maxwell system proceeds by setting $\partial/\partial t = 0$ and looking for stationary solutions $f_j(\mathbf{x}, \mathbf{v})$, $\Phi(\mathbf{x})$, and $\mathbf{A}(\mathbf{x})$ that satisfy the equations

$$\mathbf{v} \cdot \frac{\partial f_j}{\partial \mathbf{x}} + \frac{q_j}{m_j} (\mathbf{E} + \mathbf{v} \times \mathbf{B}) \cdot \frac{\partial f_j}{\partial \mathbf{v}} = 0, \quad (1.12)$$

$$\nabla^2 \Phi = -\frac{1}{\epsilon_0} \sum_j q_j \int d^3v f_j, \quad (1.13)$$

$$\nabla^2 \mathbf{A} = -\mu_0 \sum_j q_j \int d^3v \mathbf{v} f_j, \quad (1.14)$$

1.2.2 Harris Sheet Model

A class of solutions to the equilibrium Vlasov equation is given by [Harris, 1962; Lembége and Pellat, 1982]

$$f_j = n_{0j} \left(\frac{m_j}{2\pi T_j} \right)^{3/2} \exp \left(-\frac{1}{T_j} [H_j - U_{yj} P_{yj}] \right), \quad (1.15)$$

where the particles of type j have mass m_j , temperature T_j , charge q_j , canonical momentum P_{yj} , energy H_j , and drift velocity U_{yj} . The distribution function (1.15) is a function of the constants of motion H_j and P_{yj} defined by

$$H_j = \frac{1}{2} m_j v^2 + q_j \Phi(z) \quad (1.16)$$

and

$$P_{yj} = m_j v_y + q_j A_y(z). \quad (1.17)$$

Substituting (1.16) and (1.17) into (1.15) we have that the charge density is given by

$$\rho_j(z) = q_j n_{0j} \exp[q_j (U_{yj} A_y - \Phi)/T_j] \quad (1.18)$$

and that the current density is given by

$$J_y(z) = \sum_j q_j n_{0j} U_{yj} \exp[q_j (U_{yj} A_y - \Phi)/T_j]. \quad (1.19)$$

In order to have $\Phi = 0$ we require

$$\sum_j q_j n_{0j} = 0 \quad (1.20)$$

and

$$\frac{q_j U_{yj}}{T_j} = \text{const.} = \frac{q U_y}{T}. \quad (1.21)$$

Ampère's law (1.14) is given by

$$\begin{aligned} \frac{d^2 A_y}{dz^2} &= -\mu_0 \left(\sum_j q_j n_{0j} U_{yj} \right) \exp[qU_y A_y / T] \\ &= -\mu_0 \frac{qU_y}{T} \left(\sum_j n_{0j} T_j \right) \exp[qU_y A_y / T]. \end{aligned} \quad (1.22)$$

Eq. (1.22) is readily integrated for $A_y(z)$ by using the conservation law obtained by multiplying by dA_y/dz and integrating to obtain

$$\frac{1}{2} \left(\frac{dA_y}{dz} \right)^2 + \mu_0 \left(\sum_j n_{0j} T_j \right) \exp\left(\frac{qU_y A_y}{T}\right) = \text{const.} = \frac{1}{2} \left(\frac{dA_y(\infty)}{dz} \right)^2 \equiv \frac{B_{x0}^2}{2}. \quad (1.23)$$

Eq. (1.23) is consistent with the boundary conditions

$$\left(\frac{dA_y}{dz} \right)_{z=0} = 0, \quad A_y \rightarrow \mp B_{x0} z \text{ for } z \rightarrow \pm\infty \quad (1.24)$$

and gives the pressure balance condition

$$\frac{B_{x0}^2}{2\mu_0} = \sum_j n_{0j} T_j. \quad (1.25)$$

Integrating the conservation law (1.23),

$$\int_0^{A_y} \frac{dA_y}{B_{x0} \sqrt{1 - \exp\left[\frac{qU_y A_y}{T}\right]}} = \int dz = z, \quad (1.26)$$

we obtain the Harris sheet model

$$A_y(z) = -L_z B_{x0} \ln \left[\cosh \left(\frac{z}{L_z} \right) \right], \quad (1.27)$$

where we define the characteristic space length L_z by

$$\frac{1}{L_z} \equiv \left(\frac{qU_y}{T} \right) \frac{B_{x0}}{2} = \left(\frac{\sum_j q_j U_{yj}}{\sum_j T_j} \right) \frac{B_{x0}}{2}. \quad (1.28)$$

For the Harris sheet model (1.27) the magnetic field is given by

$$\mathbf{B} = B_x(z)\hat{\mathbf{e}}_x = B_{x0} \tanh\left(\frac{z}{L_z}\right) \hat{\mathbf{e}}_x, \quad (1.29)$$

the number density is

$$n_j(z) = n_{0j} \operatorname{sech}^2\left(\frac{z}{L_z}\right), \quad (1.30)$$

the pressure is

$$p(z) = \frac{B_{x0}^2}{2\mu_0} \operatorname{sech}^2\left(\frac{z}{L_z}\right), \quad (1.31)$$

and the current density is

$$j_y(z) = \frac{B_{x0}}{\mu_0 L_z} \operatorname{sech}^2\left(\frac{z}{L_z}\right). \quad (1.32)$$

Fig. 1.2 is a plot of the variation of B and n across the current sheet and of the magnetic field configuration for the Harris sheet model. In the Harris sheet model (1.27)–(1.32) the magnetic field changes sign at the center ($z = 0$) of the current sheet where both the current density and the pressure reach maximum values. For $|z| \gg 1$, that is, in the tail lobes, the magnetic field tends asymptotically to a constant value $\pm B_{x0}$, and the pressure and the current density vanish.

1.2.3 Parabolic-Like Magnetic Field Reversals

From satellite observations it is well known that a small magnetic field component B_z exists. Thus, commonly used models for the magnetic field in the CPS are the modified Harris sheet model

$$\mathbf{B} = B_{x0} \tanh\left(\frac{z}{L_z}\right) \hat{\mathbf{e}}_x + B_z \hat{\mathbf{e}}_z; \quad \frac{B_z}{B_{x0}} \ll 1, \quad (1.33)$$

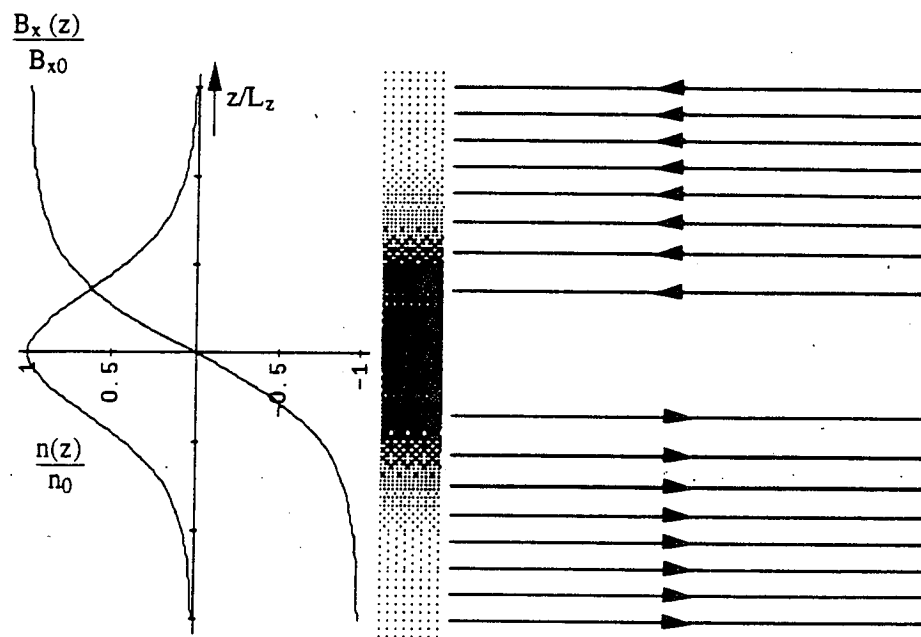


Figure 1.2: Straight magnetic field reversal. Variation of B and n as a function of z , and magnetic field lines for the Harris sheet model

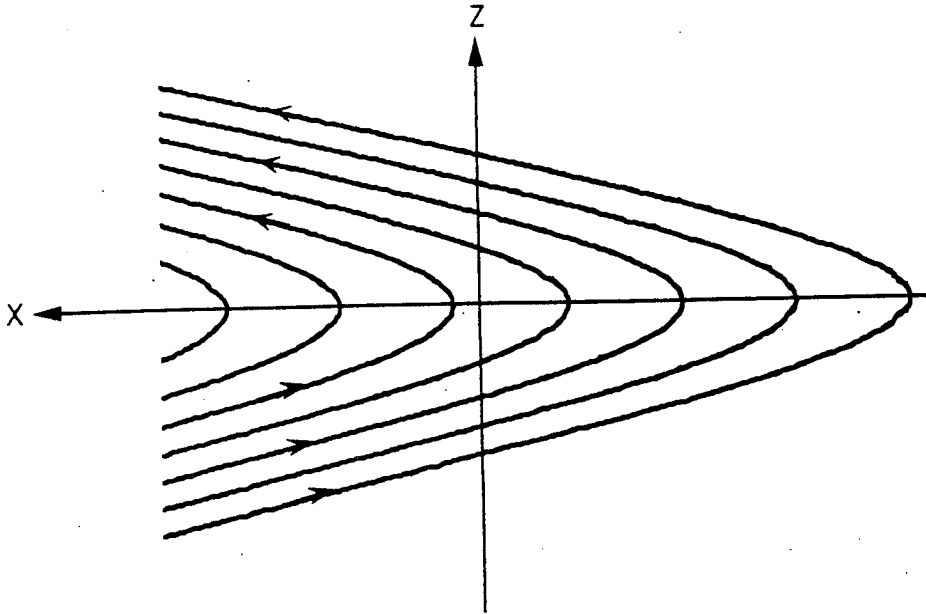


Figure 1.3: Parabolic field reversal. Magnetic field lines and coordinate system for the parabolic field model of Eq. (1.34)

where B_z is constant; and the parabolic field model

$$\mathbf{B} = B_{z0} \left(\frac{z}{L_z} \right) \hat{\mathbf{e}}_x + B_z \hat{\mathbf{e}}_z, \quad (1.34)$$

valid for $z/L_z \ll 1$. Both the model of Eq. (1.33) and that of Eq. (1.34) are not self-consistent equilibria; however, they are useful in the study of charged particle dynamics in the CPS of the geomagnetic tail. The magnetic field lines for model (1.34) and the coordinate system used throughout this work are shown in Fig. 1.3.

Force balance in a steady-state equilibrium requires a balance between the Lorentz force and the divergence of the particle momentum stress tensor,

$$\mathbf{J} \times \mathbf{B} = \nabla \cdot \mathbf{P}, \quad (1.35)$$

where the pressure tensor is given in terms of the distribution function by

$$P_{\alpha\beta} = \sum_j m_j \int d^3v (v_\alpha - U_\alpha)(v_\beta - U_\beta) f_j. \quad (1.36)$$

In the Harris sheet model (1.29) the assumption of isotropic plasma has been made and the force balance (1.35) is replaced by

$$\mathbf{J} \times \mathbf{B} = \nabla p, \quad (1.37)$$

where p is the scalar pressure. From (1.37) we have that

$$\mathbf{B} \cdot \nabla p = 0 \quad (1.38)$$

and

$$\mathbf{J} \cdot \nabla p = 0, \quad (1.39)$$

that is, the $p = \text{const.}$ surfaces are both magnetic surfaces and current surfaces. On the other hand,

$$\mathbf{B}(x, z) = \nabla A_y(x, z) \times \hat{\mathbf{e}}_y, \quad (1.40)$$

which implies that

$$\mathbf{B} \cdot \nabla A_y = 0, \quad (1.41)$$

that is, $A_y(x, z)$ is a magnetic flux function.

From (1.38) and (1.41) we have that the scalar pressure p is a function of A_y , $p = p(A_y)$ and that the force balance condition (1.37) can be written as

$$\nabla^2 A_y + \mu_0 \frac{dp}{dA_y} = 0 \quad (1.42)$$

with the current density

$$J_y(A_y) = \frac{dp(A_y)}{dA_y}. \quad (1.43)$$

The pressure function $p(A_y)$ is a free function and under the assumption of local thermodynamic equilibrium (1.15), $p(A_y)$ takes the form

$$p(A_y) = \frac{B_{x0}^2}{2\mu_0} \exp[2A_y(x, z)/L_z B_{x0}]. \quad (1.44)$$

In the mid and far regions of the geomagnetic tail, the characteristic gradient scale length L_x in the tailward direction is much larger than the characteristic gradient scale length L_z in the z -direction,

$$\delta \equiv \frac{L_z}{L_x} \ll 1. \quad (1.45)$$

The relevant definition of L_x is

$$\frac{1}{L_x} = \frac{\partial}{\partial x} \ln(B_z(x, 0, 0)) \quad (1.46)$$

and of L_z is

$$\begin{aligned} \frac{1}{L_z} &= \left(\frac{\partial}{\partial z} \ln B_x(x, 0, z) \right)_{z=0} \\ &= \frac{1}{B_{x0}} \left(\frac{\partial B_x}{\partial z} \right)_{z=0} \\ &= \frac{\mu_0 j_y}{B_{x0}}, \end{aligned} \quad (1.47)$$

where B_{x0} is a typical lobe field value.

Under the approximation (1.45), an asymptotic class of x -dependent solutions to

$$\nabla^2 A_y(x, z) = -\frac{B_{x0}}{L_z} \exp[2A_y/L_z B_{x0}] \quad (1.48)$$

is given by [Schindler, 1972; Birn et al., 1975; Lembége and Pellat, 1982; Zwiggmann, 1983]

$$A_y(x, z) = -B_{x0} L_z \ln \left\{ \frac{\cosh \left[\left(\frac{z}{L_z} \right) G(x) \right]}{G(x)} \right\} + \mathcal{O}(\delta^2), \quad (1.49)$$

where the function $G(x)$ is arbitrary, as long as (1.45) is satisfied. From (1.49) we have that the magnetic field components are given by

$$B_x(x, z) = B_{x0}G(x) \tanh \left[\left(\frac{z}{L_z} \right) G(x) \right] \quad (1.50)$$

and

$$B_z(x, z) = L_z B_{x0} \frac{G'(x)}{G(x)} \left(1 - G(x) \frac{z}{L_z} \tanh \left[\left(\frac{z}{L_z} \right) G(x) \right] \right), \quad (1.51)$$

the current density is given by

$$J_y(x, z) = \frac{B_{x0}}{\mu_0 L_z} G^2(x) \operatorname{sech}^2 \left[\left(\frac{z}{L_z} \right) G(x) \right], \quad (1.52)$$

and the pressure is given by

$$p(x, z) = \frac{B_{x0}^2}{2\mu_0} G^2(x) \operatorname{sech}^2 \left[\left(\frac{z}{L_z} \right) G(x) \right]. \quad (1.53)$$

Several functional forms of $G(x)$ have been used by various authors. The case of $G(x) = 1$ corresponds to the Harris sheet model (1.27). *Lembége and Pellat* [1982] have used

$$G_1(x) = \exp \left(b_z \frac{x}{L_z} \right) \quad (1.54)$$

and

$$G_2(x) = b_z \frac{x}{L_z} \exp \left(b_z \frac{x}{L_z} \right), \quad (1.55)$$

where

$$b_z \equiv \frac{B_z}{B_{x0}}. \quad (1.56)$$

Zwingmann [1983] has used the power law model

$$G_3(x) = \left(1 - b_z \frac{x}{\nu L_z} \right)^{-\nu}, \quad (1.57)$$

with $\nu = 0.6$ determined from the best fit to the data.

1.2.4 Sheared Parabolic Magnetic Field Reversals

In order to account for the component of the interplanetary magnetic field which soaks into the magnetosphere along the dawn-dusk direction, we add a constant B_y to the tail-like magnetic field reversals of the previous section. From satellite observations [Fairfield, 1979; Akasofu *et al.*, 1978; Cattell *et al.*, 1986] it is well known that a finite dawn-dusk magnetic field component B_y exists and that it may be comparable to the magnetic field component normal to the current sheet B_z .

The simplest model of a sheared tail-like magnetic field reversal is given by

$$\mathbf{B} = B_{x0} \frac{z}{L_z} \hat{\mathbf{e}}_x + B_y \hat{\mathbf{e}}_y + B_z \hat{\mathbf{e}}_z, \quad (1.58)$$

where $B_y = \text{const.}$ Fig. 1.4 is a plot of the magnetic field lines for the field model (1.58) with $B_y = B_z$. As observed from Fig. 1.4, the effects of the dawn-dusk magnetic field component are (1) to introduce a tilt on the field lines away from the meridian and (2) to increase the effective field line length in the quasineutral layer with the subsequent reduction of the particle oscillation frequency along the field lines.

A general theory of three-dimensional magnetostatic equilibrium has been developed by Birn [1987] and applied to study the effect of B_y on the magnetotail equilibrium configuration [Birn, 1990]. The sheared parabolic magnetic field reversal of Eq. (1.58) has been used in charged particle motion studies by Karimabadi *et al.* [1990] and Horton *et al.* [1992], and in collisionless tearing mode studies by Wang *et al.* [1990], Büchner *et al.* [1991], and Hernández *et al.* [1993].

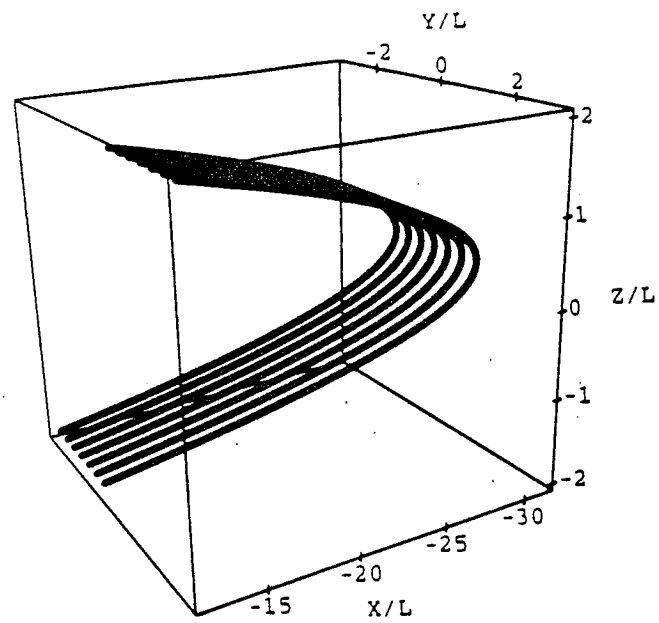


Figure 1.4: Sheared parabolic field reversal. Magnetic field lines for the sheared parabolic field model of Eq. (2.126).

Chapter 2

Chapter 2. Particle Dynamics in Magnetic Field Reversals

In this chapter we discuss single particle dynamics in the different magnetic field reversals and introduce surface of section plots and Liapunov exponents, which are used in the study of chaotic particle dynamics.

2.1 Particle Dynamics in Straight Magnetic Field Reversals

The simplest example of a local current sheet is provided by the magnetic field model

$$\mathbf{B}(z) = B_{x0} \frac{z}{L_z} \hat{e}_x. \quad (2.1)$$

This model applies for $|z|$ sufficiently small that the current density $J_y = B_{x0}/\mu_0 L_z = \text{const}$. Particle trajectories in (2.1) were integrated analytically by *Speiser* [1965] and their associated adabatic invariants are thoroughly discussed by *Sonnerup* [1971].

Particle dynamics in the magnetic field reversal of Eq. (2.1) is governed by the Hamiltonian

$$H = \frac{P_x^2}{2m} + \frac{P_z^2}{2m} + \frac{1}{2m} \left(P_y + qB_{x0} \frac{z^2}{2L_z} \right)^2. \quad (2.2)$$

Translational invariance in the x and y directions leads to conservation of the x and y components of the canonical momentum, P_x and P_y , respectively. On

the other hand, energy conservation, $E = mv^2/2 = \text{const.}$, is a consequence of time independence. Thus, we have a dynamical system with three degrees of freedom, three constants of motion (P_x , P_y , E) and the motion is integrable.

Since P_y is a constant of motion, it is convenient to introduce the effective potential

$$V(z) = \frac{1}{2m} \left(P_y + qB_{x0} \frac{z^2}{2L_z} \right)^2. \quad (2.3)$$

The topology of the potential well is controlled by the value of P_y . Fig. 2.1 is a plot of (a) the effective potential $V(z)$ and (b) the corresponding $z - P_z$ phase space diagram for $qP_y > 0$. The case with $qP_y < 0$ is shown in Fig. 2.2.

From Figs. 2.1 and 2.2 we observe that as P_y changes sign, $V(z)$ undergoes a bifurcation from the parabolic-like geometry shown in Fig. 2.1, with a stable O-point at the origin, to the bi-stable potential well shown in Fig. 2.2, with an unstable X-point at $z = 0$ and two elliptic O-points at $z = \pm z_0$, where $z_0 \equiv \sqrt{2L_z|P_y|/qB_{x0}}$. For $P_y < 0$, $V(z)$ has a separatrix (SX) which occurs when $E = E_0 \equiv P_y^2/2m$. The presence of the separatrix is very important since it separates regions with different dynamical behavior that reach altogether different regions of z and thus provides the seed for chaotic particle motion when the system is perturbed by magnetic or electric fields, as will be shown in the next section.

Fig. 2.3 shows the projection on the $y - z$ plane of charged ($q > 0$) particle trajectories which occur in the field reversal model of Eq. (2.1). We distinguish four cases:

- (a) $P_y > 0$. The potential $V(z)$ has the parabolic form shown in Fig. 2.1, the particles drift from dawn-to-dusk, that is, in the $+y$ -direction, and exe-

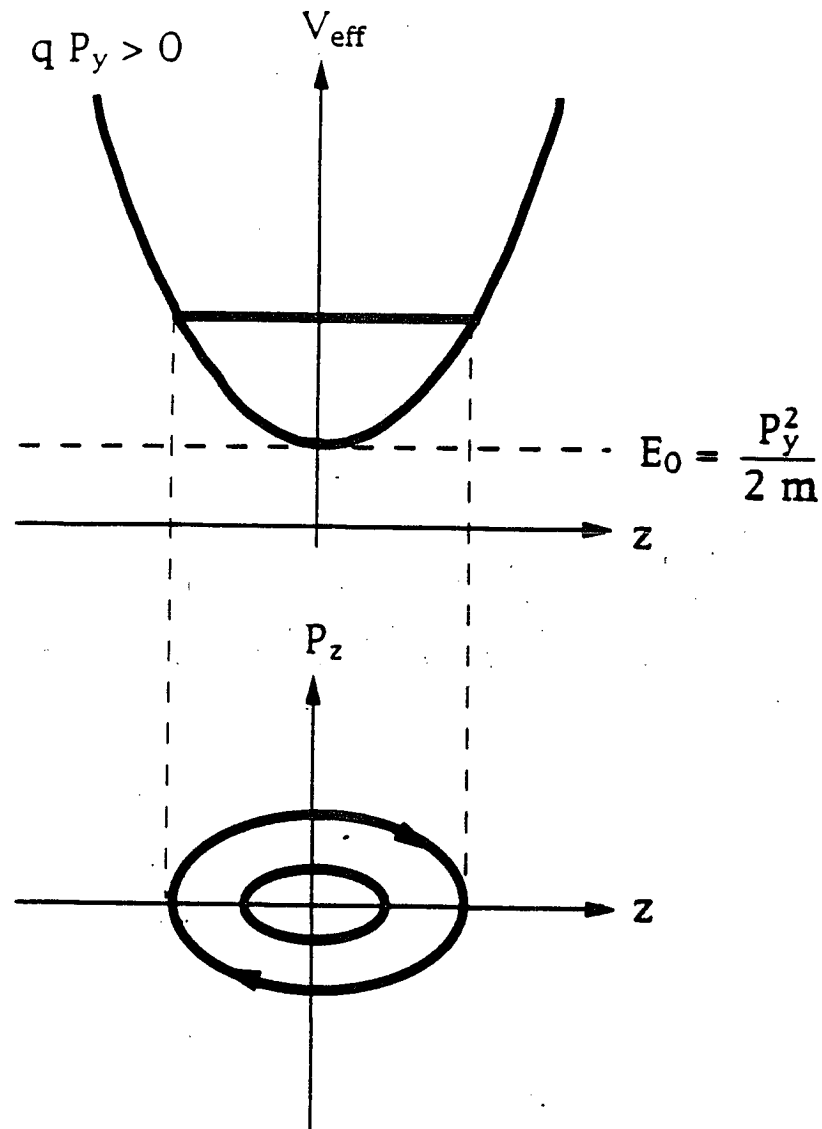


Figure 2.1: Effective potential and phase space diagram for $qP_y > 0$: (a) $V(z)$, (b) $z - P_z$ phase space diagram.

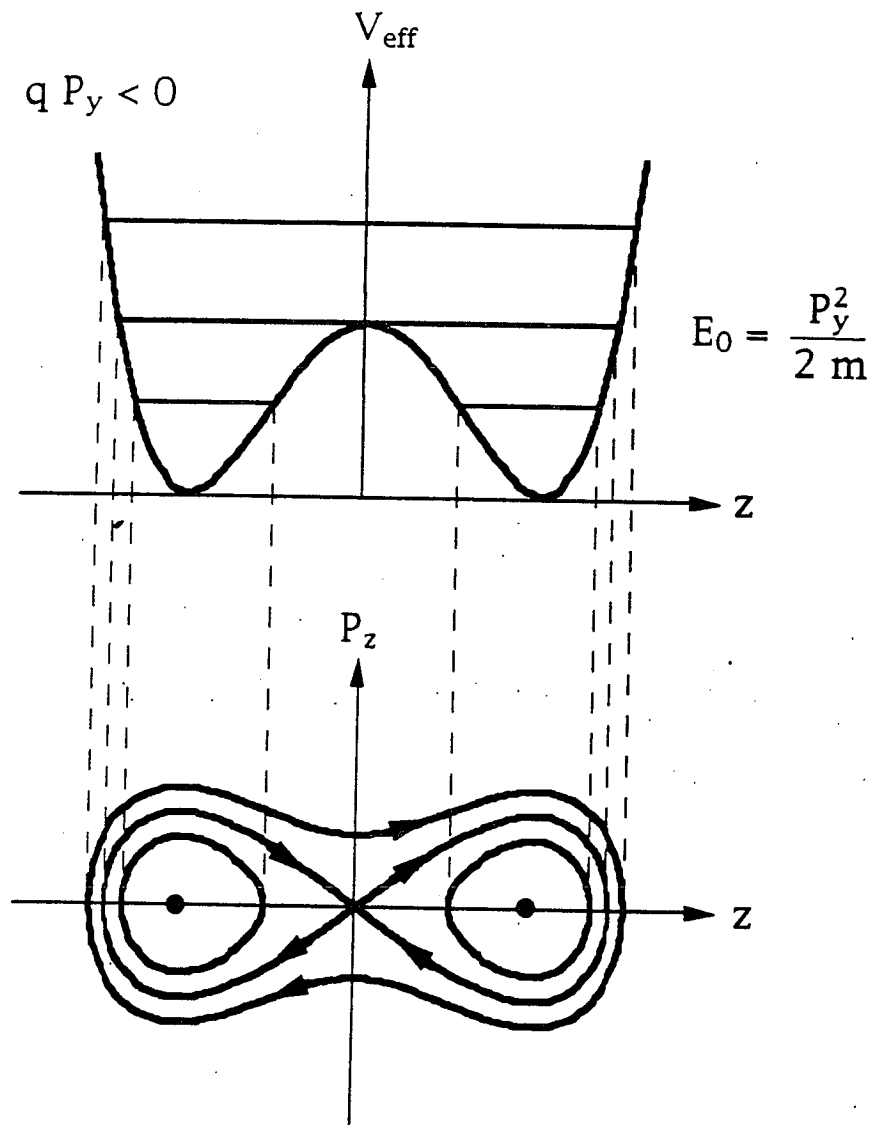


Figure 2.2: Effective potential and phase space diagram for $qP_y < 0$: (a) $V(z)$, (b) $z - P_z$ phase space diagram.

cute a north-south meandering motion about $z = 0$ with a characteristic oscillation frequency ω_{bz} , to be defined below.

- (b) $P_y < 0$, $E < E_0$. The effective potential has the double well shape shown in Fig. 2.2. The particles are trapped in the potential wells below the local maximum at $z = 0$, drift from dusk to dawn, and execute cyclotron motion with a substantial ∇B -drift and with cyclotron frequency

$$\omega_{cx} = \omega_{cx0} \frac{z_0}{L_z}, \quad (2.4)$$

where

$$\omega_{cx0} \equiv \frac{qB_{x0}}{m} \quad (2.5)$$

is the cyclotron frequency around the lobe magnetic field B_{x0} .

- (c) $P_y < 0$, $E = E_0$. This case corresponds to motion along the separatrix in phase space. The particles stream from dusk to dawn taking an infinite time to complete a single loop in the $y - z$ -plane.
- (d) $P_y < 0$, $E > E_0$. The energy of the particles is above the local potential maximum. The particles stream from dusk-to-dawn and execute meandering motion about $z = 0$.

The equations of motion for charged particles in the magnetic field reversal of Eq. (2.1) are given by

$$\dot{x} = \frac{P_x}{m}, \quad (2.6)$$

$$\dot{P}_x = 0, \quad (2.7)$$

$$\dot{y} = \frac{P_y}{m} + \omega_{cx0} \frac{z^2}{2L_z}, \quad (2.8)$$

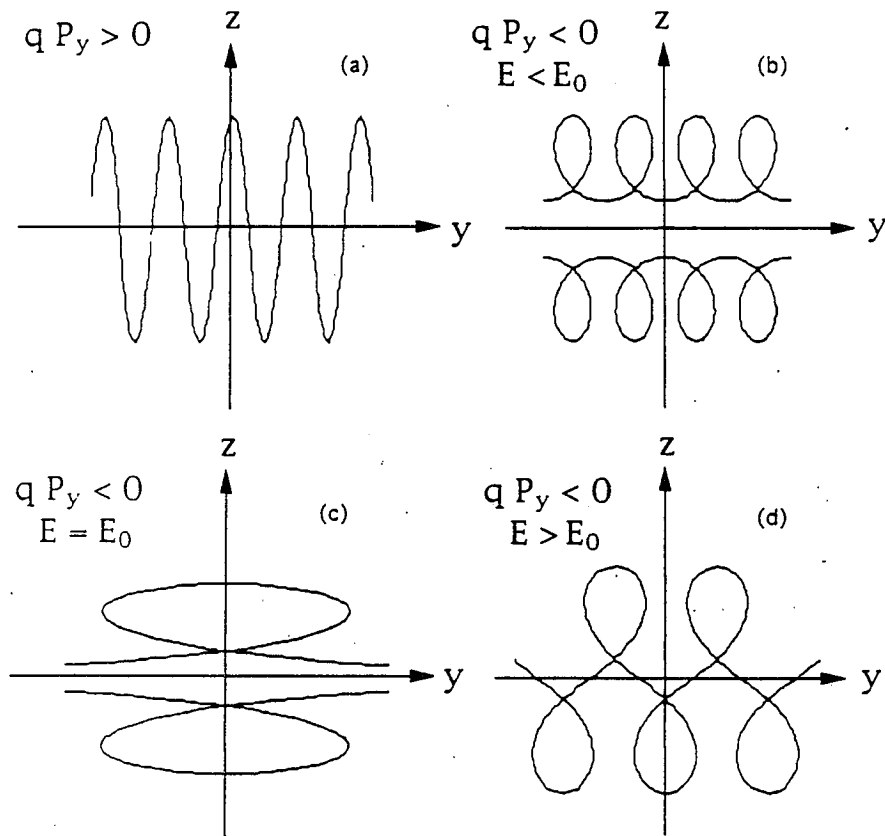


Figure 2.3: Charged particle trajectories for straight field reversals. Here we take $q > 0$ and note that for $q < 0$ the trajectories are the same but with the replacement $P_y \rightarrow -P_y$. (a) $P_y > 0$, (b) $P_y < 0$, $E < E_0$, (c) $P_y < 0$, $E = E_0$, (d) $P_y < 0$, $E > E_0$.

Figure 2.3: Charged particle trajectories for straight field reversals. Here we take $q > 0$ and note that for $q < 0$ the trajectories are the same but with the replacement $P_y \rightarrow -P_y$. (a) $P_y > 0$, (b) $P_y < 0$, $E < E_0$, (c) $P_y < 0$, $E = E_0$, (d) $P_y < 0$, $E > E_0$.

$$\dot{P}_y = 0, \quad (2.9)$$

$$\dot{z} = \frac{P_z}{m}, \quad (2.10)$$

$$\dot{P}_z = -\frac{1}{m} \left(P_y + qB_{x0} \frac{z^2}{2L_z} \right) qB_{x0} \frac{z}{L_z} = -m\omega_{cx0} v_y \frac{z}{L_z}. \quad (2.11)$$

For the meandering orbits across the $z = 0$ plane the excursions in z , Δz , are bounded by $|P_y + qB_{x0} \frac{z^2}{2L_z}| \leq (2mE_\perp)^{1/2}$, which implies

$$\Delta z \leq \left[\frac{2L_z(2mE_\perp)^{1/2}}{qB_{x0}} \right]^{1/2} = (2\rho L_z)^{1/2}, \quad (2.12)$$

where $E_\perp = E - P_x^2/2m = mv_\perp^2/2$, and ρ is the Larmor radius around the lobe magnetic field B_{x0} ,

$$\rho = \frac{v_\perp}{\omega_{cx0}}, \quad (2.13)$$

with $v_\perp = \sqrt{v_y^2 + v_z^2}$. On the other hand, from the equations of motion we have that the vertical oscillations across the current sheet are given by

$$\ddot{z} = -\omega_{bz}^2 z, \quad (2.14)$$

where

$$\omega_{bz}^2 \equiv \frac{\omega_{cx0} v_y}{L_z} \quad (2.15)$$

with v_y given by (2.8). If $v_y > 0$, then the particles oscillate about $z = 0$ and if $v_y < 0$, then the particles are ejected from the current sheet since $z(t)$ from (2.14) is exponentially growing. In an average sense, we will be using ω_{bz} defined by

$$\omega_{bz} = \left(\frac{v_\perp \omega_{cx0}}{L_z} \right)^{1/2} = \epsilon^{1/2} \omega_{cx0}, \quad (2.16)$$

where ϵ is the finite Larmor radius parameter,

$$\epsilon \equiv \frac{\rho}{L_z}. \quad (2.17)$$

In current sheet plasmas where the magnetic field reverses its direction over short distances, the finite Larmor radius parameter can be $\epsilon \lesssim 1$ and the guiding center approximation breaks down. Particle motion in current sheets can be separated into rapid gyromotion around \mathbf{B} in the lobe region and current sheet oscillations along the vertical direction.

2.1.1 Integration of the Equations of Motion

Particle motion in the magnetic field reversal (2.1) can be integrated by quadratures with the solutions given in terms of elliptic functions. Since P_x is a constant of the motion, it is convenient to work only with the perpendicular part of the Hamiltonian (2.2)

$$H_{\perp} = \frac{P_z^2}{2m} + \frac{1}{2m} \left(P_y + qB_{x0} \frac{z^2}{2L_z} \right)^2, \quad (2.18)$$

and drop the \perp subscript on the Hamiltonian for notational simplicity.

We first note that for $P_y < 0$ the minima of the effective potential are located at $\pm z_0 \equiv \pm \sqrt{2L_z |P_y| / qB_{x0}}$ and the energy at the separatrix is $E_0 = P_y^2 / 2m$. Introducing the notation

$$z_{\pm}^2 = z_0^2 (1 \pm h^{1/2}), \quad (2.19)$$

where $h \equiv E/E_0$, we have that for $P_y < 0$ and $E > E_0$ the bouncing points z_b are located at $z_b^2 = z_+^2$ and that for $P_y < 0$ and $E < E_0$ the bouncing points are located at $z_b^2 = z_{\pm}^2$.

Choosing the $t = 0$ reference time as the moment when $z(t)$ reaches the bouncing point we have, for $P_y < 0$ and $E > E_0$,

$$\pm bt = \int_{z_+}^z \frac{dz}{\sqrt{(z_+^2 - z^2)(z^2 - z_-^2)}} = -\frac{1}{\sqrt{z_+^2 - z_-^2}} F(\arccos \frac{z}{z_+} | m), \quad (2.20)$$

where

$$b = \frac{\omega_{cx0}}{2L_z}, \quad (2.21)$$

$$m = \frac{z_+^2}{z_+^2 - z_-^2} = \frac{1 + \sqrt{h}}{2\sqrt{h}}, \quad \frac{1}{2} \leq m \leq 1, \quad (2.22)$$

and $F(\phi|m)$ is the elliptic integral of the first kind defined by

$$F(\phi|m) = \int_0^\phi \frac{d\theta}{\sqrt{1 - m \sin^2 \theta}}. \quad (2.23)$$

From (2.20) we have that the motion is given by

$$z(t) = z_+ \operatorname{cn}(\sqrt{z_+^2 - z_-^2} bt|m) \quad (2.24)$$

with the period of the Jacobi elliptic function $\operatorname{cn}(u|m)$ being $4K(m)$, where $K(m) = F(\pi/2|m)$ is the complete elliptic integral of the first kind. Noting that

$$\sqrt{z_+^2 - z_-^2} b = \sqrt{2bz_0} h^{1/4} = \left(\frac{v\omega_{cx0}}{L_z} \right)^{1/2} = \omega_{bz}, \quad (2.25)$$

the frequency is given by

$$\Omega = \frac{\pi\omega_{bz}}{2K(m)}. \quad (2.26)$$

In the $h \gg 1$ limit we have, $m \rightarrow 1/2$, $K(m) \rightarrow \pi/2$, and $\Omega \rightarrow \omega_{bz}$.

In the limit $h \rightarrow 1$ we have, $m \rightarrow 1$, $K(m) \rightarrow \infty$, $\operatorname{cn} \rightarrow \operatorname{sech}$, and the separatrix motion is given by

$$z(t) = \sqrt{2}z_0 \operatorname{sech} \left(\frac{\omega_{cx0}z_0}{\sqrt{2}L_z} t \right). \quad (2.27)$$

In the $E < E_0$, $P_y < 0$ case, we have

$$\pm bt = -\frac{1}{z_+} F \left(\arcsin \sqrt{\frac{1 - z^2/z_+^2}{m}} |m \right), \quad (2.28)$$

where

$$m = \frac{z_+^2 - z_-^2}{z_+^2} = \frac{2\sqrt{h}}{1 + \sqrt{h}}, \quad 0 \leq m \leq 1, \quad (2.29)$$

and

$$z(t) = z_+ \operatorname{dn}(bz_+ t | m), \quad (2.30)$$

with the period of the Jacobi elliptic function $\operatorname{dn}(u|m)$ being $2K(m)$ or, from (2.30),

$$T = \frac{2K(m)}{bz_+}. \quad (2.31)$$

In the $h \ll 1$ limit we have, $m \ll 1$, $z_+ \approx z_0$,

$$z(t) = z_0 \left(1 - \frac{m}{4}\right) + \frac{m}{4} \cos(\omega_{cx} t), \quad (2.32)$$

and the rotation frequency reduces to

$$\Omega \rightarrow \omega_{cx} \equiv \omega_{cx0} \frac{z_0}{L_z}, \quad (2.33)$$

which is the cyclotron frequency at the bottom of the potential well.

For $P_y > 0$ the minimum of the potential occurs at the center of the current sheet $z = 0$, and $E \geq 0$. Introducing

$$z_{\pm}^2 = z_0^2 (h^{1/2} \pm 1), \quad (2.34)$$

the bouncing points are located at $z_b^2 = z_-^2$ and

$$\pm bt = \int_{z_-}^z \frac{dz}{\sqrt{(z_-^2 - z^2)(z^2 + z_+^2)}} = -\frac{1}{\sqrt{z_-^2 + z_+^2}} F\left(\arccos \frac{z}{z_-} | m\right), \quad (2.35)$$

where

$$m = \frac{z_-^2}{z_-^2 + z_+^2} = \frac{h^{1/2} - 1}{2h^{1/2}}, \quad 0 \leq m \leq \frac{1}{2}. \quad (2.36)$$

From (2.35) we get

$$z(t) = z_- \operatorname{cn}(\omega_{bz} t | m), \quad (2.37)$$

with frequency

$$\Omega = \frac{\pi\omega_{bz}}{K(m)}. \quad (2.38)$$

Note that in the limit $h \rightarrow 1$ we have, $m \rightarrow 0$, $K(m) \rightarrow \pi/2$, $\Omega \rightarrow \omega_{bz}$, and $\text{cn} \rightarrow \cos$.

From (2.34)–(2.38) we have that the $P_y = 0$ case corresponds to $m = 1/2$,

$$z(t) = (2\rho L_z)^{1/2} \text{cn}(\omega_{bz}t|1/2), \quad (2.39)$$

and

$$\Omega = \frac{\pi\omega_{bz}}{2K(1/2)} = 0.847\omega_{bz}. \quad (2.40)$$

One of the basic characteristics of nonlinear motion is the dispersion of the frequency as a function of the constants of the motion, $\Omega = \Omega(H, P_y)$. For the straight magnetic field reversal of Eq. (2.1) the dispersion of the frequency is given by Eqs. (2.26), (2.31), (2.38), and (2.40). Fig. 2.4 is a plot of Ω/ω_{cx0} as a function of $\hat{H} \equiv H/mv_0^2$, where $v_0 \equiv \omega_{cx0}L_z$, for $\hat{P}_y \equiv P_y/mv_0 = 0.5$, 0, and -0.5 . The dashed line corresponds to $\hat{\omega}_{bz} \equiv \omega_{bz}/\omega_{cx0} = (2\hat{H})^{1/4}$. For $\hat{P}_y > 0$ the frequency is given by Eq. (2.38), and when $\hat{H} \rightarrow \hat{P}_y^2/2 = 0.125$ we have, $\hat{\Omega} \rightarrow \hat{\omega}_{bz} = (2\hat{H})^{1/4}$. For $\hat{P}_y < 0$ and $\hat{H} > \hat{P}_y^2$ the frequency is given by Eq. (2.26), and when $\hat{H} \gg \hat{P}_y^2$, we find $\hat{\Omega} \approx 0.84\hat{\omega}_{bz} = 0.84(2\hat{H})^{1/4}$. When $\hat{H} \rightarrow \hat{P}_y^2/2$ the system takes the separatrix motion and $\hat{\Omega} \rightarrow 0$. For $\hat{P}_y < 0$ and $\hat{H} < \hat{P}_y^2/2$, the frequency is given by Eq. (2.31), and when $\hat{H} \ll \hat{P}_y^2/2$, that is, near the bottom of the potential well, we have $\hat{\Omega} \rightarrow z_0/L_z = \sqrt{2|\hat{P}_y|}$.

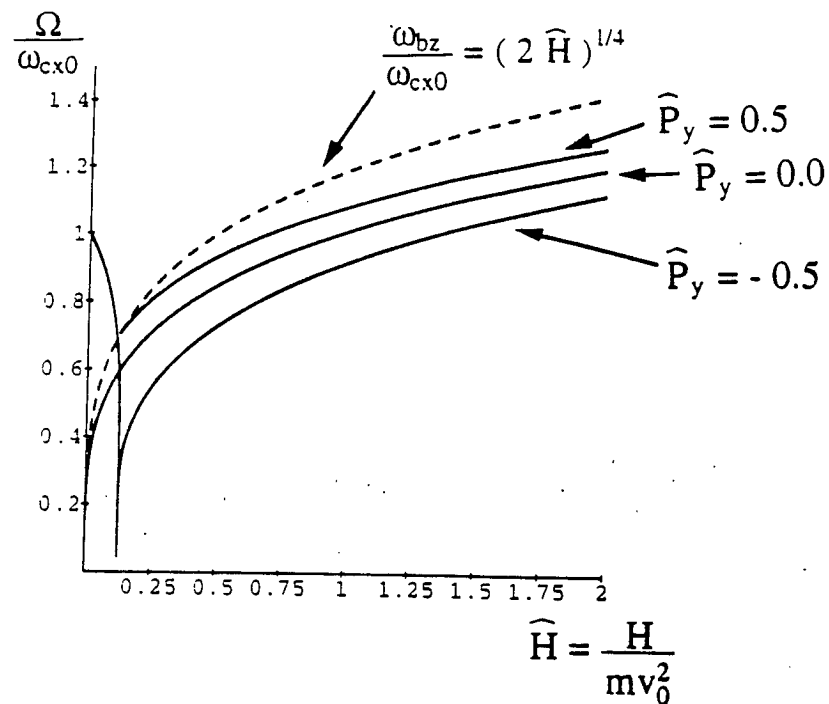


Figure 2.4: Dispersion of orbital frequencies for straight magnetic field reversals. Plot of Ω/ω_{cx0} as a function of $\hat{H} \equiv H/mv_0^2$, where $v_0 \equiv \omega_{cx0}L_z$, for $\hat{P}_y \equiv P_y/mv_0 = 0.5, 0, -0.5$. The dashed line corresponds to $\hat{\omega}_{bz} \equiv \omega_{bz}/\omega_{cx0} = (2\hat{H})^{1/4}$ and is included for reference.

2.2 Particle Motion in Parabolic Magnetic Field Reversals: Chaotic Motion

In order to account for the small but finite magnetic field component normal to the current sheet of the CPS, it is common practice to add a constant magnetic field component normal to the current sheet, $B_z \neq 0$. The introduction of a constant B_z has important consequences because particles with small pitch angles, $\alpha = \sin^{-1}(v_{\perp}/v) \ll 1$, can freely cross the $z = 0$ -plane, connecting the reversed $B_x(z)$ fields on the two sides of the current sheet.

Our model Hamiltonian has the form

$$H = \frac{P_x^2}{2m} + \frac{P_z^2}{2m} + \frac{1}{2m}(P_y - qA_y(x, z))^2, \quad (2.41)$$

where

$$\begin{aligned} A_y(x, z) &= -L_z B_{x0} \ln \left[\cosh \left(\frac{z}{L_z} \right) \right] + B_z x \\ &\approx -B_{x0} \frac{z^2}{2L_z} + B_z x; \quad z/L_z \ll 1. \end{aligned} \quad (2.42)$$

There are now two constants of motion (H, P_y); the motion is not integrable, that is, no closed form solution exists; and particle motion may be chaotic. Chaotic particle motion in parabolic-like magnetic field reversals was first studied by *Büchner and Zelenyi* [1986] and *Chen and Palmadesso* [1986]. Thorough reviews of nonlinear particle dynamics in current sheets are given in *Chen* [1992] and *Dusenbery and Martin* [1994].

With the coordinate transformation

$$x \rightarrow x + \frac{P_y}{qB_z}, \quad (2.43)$$

the Hamiltonian for the parabolic field model takes the form

$$\begin{aligned} H &= \frac{P_x^2}{2m} + \frac{P_z^2}{2m} + \frac{m}{2} \left(\omega_{cx0} \frac{z^2}{2L_z} - \omega_{cz} x \right)^2 \\ &= H_x(P_x, x) + H_z(P_z, z) - \alpha x z^2. \end{aligned} \quad (2.44)$$

Here

$$H_x(P_x, x) = \frac{P_x^2}{2m} + \frac{m}{2} \omega_{cz}^2 x^2 \quad (2.45)$$

describes the $x - P_x$ cyclotron motion around B_z with cyclotron frequency ω_{cz} defined by

$$\omega_{cz} \equiv \frac{qB_z}{m}, \quad (2.46)$$

and

$$H_z(P_z, z) = \frac{P_z^2}{2m} + \frac{m}{2} \omega_{cx0}^2 \frac{z^4}{4L_z^2} \quad (2.47)$$

is the quartic harmonic oscillator with characteristic vertical bounce frequency ω_{bz} defined in Eq. (2.16). Both oscillators are nonlinearly coupled by the term $-\alpha x z^2$, where

$$\alpha \equiv m \omega_{cx0} \omega_{cz} / 2L_z^2. \quad (2.48)$$

Reference values for particle and field parameters are listed in Table 1.1.

Following *Büchner and Zelenyi* [1986] we introduce the parameter

$$\kappa \equiv \frac{\omega_{cz}}{\omega_{bz}} = \frac{b_z}{\epsilon^{1/2}}, \quad (2.49)$$

where

$$b_z \equiv \frac{B_z}{B_{x0}} \quad (2.50)$$

and ϵ is the finite Larmor radius parameter (2.17). Thus, κ has the meaning of the amount of rotation around B_z in one vertical bounce period. For particle

and field parameters such that $\kappa \gg 1$ ($\omega_{cz} \gg \omega_{bz}$), the magnetic moment $\mu = v_{\perp}^2/2B(z)$ is an adiabatic invariant and particle motion can be described in terms of the guiding center approximation. For $\kappa \ll 1$ ($\omega_{cz} \ll \omega_{bz}$), we have fast vertical oscillations and the current sheet action,

$$I_z(H_{\perp}, x) = \frac{1}{2\pi} \oint \dot{z} dz, \quad (2.51)$$

is an adiabatic invariant. Finally, for $\kappa \approx 1$ ($\omega_{cz} \approx \omega_{bz}$), there are no adiabatic invariants and chaotic particle motion is found. Wide spread chaotic motion occurs for values of κ in the range $0.1 \lesssim \kappa \lesssim 2$. The detailed calculation of I_z in terms of elliptic integrals is given in Eqs. (2.71)–(2.76).

2.2.1 Guiding Center Motion

The κ parameter can also be written in terms of the minimum radius of curvature of the magnetic field lines R_{min} and the maximum Larmor radius ρ_{max} . To see this we introduce the curvature vector κ_c derived from the tangent field $\mathbf{b}(\mathbf{x}) \equiv \mathbf{B}(\mathbf{x})/B$ by

$$\kappa_c = (\mathbf{b} \cdot \nabla)\mathbf{b} = \frac{b_z^2 \left(b_z \hat{\mathbf{e}}_x + \frac{z}{L_z} \hat{\mathbf{e}}_z \right)}{L_z \left(b_z^2 + \frac{z^2}{L_z^2} \right)^{3/2}}. \quad (2.52)$$

The minimum radius of curvature occurs at the equatorial plane $z = 0$ where

$$\kappa_c = \frac{\hat{\mathbf{e}}_x}{R_{min}} = \frac{\hat{\mathbf{e}}_x}{b_z L_z}. \quad (2.53)$$

Away from the reversal layer $|\kappa_c(z)|$ decreases as $1/|z|^3$. At $z = 0$ the magnetic field reaches its minimum value, $B_{min} = B_z$, and the Larmor radius reaches its maximum value

$$\rho_{max} = \frac{v}{\omega_{cz}} = \frac{1}{b_z} \frac{v}{\omega_{cx0}} = \frac{\rho}{b_z}. \quad (2.54)$$

Comparing Eqs. (2.53) and (2.54) with Eq. (2.49) we obtain the relation

$$\kappa = \frac{\omega_{cz}}{\omega_{bz}} = \left(\frac{R_{min}}{\rho_{max}} \right)^{1/2}. \quad (2.55)$$

The guiding center approximation is valid if the Larmor radius is everywhere small compared to the curvature radius. This condition is satisfied for $\kappa \gg 1$.

In the guiding center picture, particle motion corresponds to cyclotron motion around the magnetic field lines distorted by the curvature drift

$$\begin{aligned} \mathbf{v}_c &= \frac{mv_{\parallel}^2}{qB} (\mathbf{b} \times \boldsymbol{\kappa}_c) \\ &= \frac{v_{\parallel}^2}{\omega_{cx0} L_z} \frac{b_z^2}{\left(\frac{z^2}{L_z^2} + b_z^2 \right)^2} \hat{\mathbf{e}}_y, \end{aligned} \quad (2.56)$$

and by the ∇B -drift

$$\begin{aligned} \mathbf{v}_{\nabla B} &= \frac{mv_{\perp}^2}{2qB} \frac{\mathbf{b} \times \nabla B}{B} \\ &= -\frac{v_{\perp}^2}{2\omega_{cx0} L_z} \frac{z^2/L_z^2}{\left(\frac{z^2}{L_z^2} + b_z^2 \right)^2} \hat{\mathbf{e}}_y. \end{aligned} \quad (2.57)$$

Thus, the curvature drift is strongly peaked at $z = 0$ with the width $|z| \leq R_{min} = b_z L_z$ whereas the ∇B -drift is peaked at $|z| = R_{min} = b_z L_z$.

2.2.2 Numerical Integration of the Motion, Current Sheet Action, and Orbit Classification

To integrate numerically the equations of motion it is convenient to introduce dimensionless variables appropriate for the current sheet. For a given value of $H = \frac{1}{2}mv^2$ we transform the (x, t) variables by

$$x \rightarrow (\rho L_z)^{1/2} x \quad \text{and} \quad t \rightarrow t/\omega_{bz}. \quad (2.58)$$

The dimensionless Hamiltonian,

$$h = \frac{H}{m\rho L_z \omega_{bz}^2}, \quad (2.59)$$

for the modified Harris sheet takes the form

$$h = \frac{P_x^2}{2} + \frac{P_z^2}{2} + \frac{1}{2} \left(\frac{1}{\epsilon} \ln[\cosh(\epsilon^{1/2} z)] - \kappa x \right)^2 = \frac{1}{2}, \quad (2.60)$$

which is a function of the two parameters ϵ and κ or ϵ and b_z . For the parabolic magnetic field the dimensionless Hamiltonian is

$$h = \frac{P_x^2}{2} + \frac{P_z^2}{2} + \frac{1}{2} \left(\frac{z^2}{2} - \kappa x \right)^2 = \frac{1}{2}, \quad (2.61)$$

which is a function of only one parameter κ . In the rescaled coordinates Eq. (2.58) the relevant spatial parameters are given by

$$\rho = \epsilon^{1/2} \quad \text{and} \quad L_z = \frac{1}{\epsilon^{1/2}}, \quad (2.62)$$

and the relevant frequencies are given by

$$\omega_{cz} = \kappa, \quad \omega_{bz} = 1, \quad \text{and} \quad \omega_{cx0} = \frac{1}{\epsilon^{1/2}}. \quad (2.63)$$

Another widely used coordinate transformation, introduced by *Chen and Palmadesso* [1986], is given by

$$x \rightarrow b_z L_z x, \quad t \rightarrow t/\omega_{cz}. \quad (2.64)$$

The dimensionless Hamiltonian

$$\hat{H}_{CP} = \frac{H}{m b_z^2 L_z^2 \omega_{cz}^2} \quad (2.65)$$

plays the role of the chaos parameter and is related to κ through the relationship

$$\hat{H}_{CP} = \frac{1}{2\kappa^4}. \quad (2.66)$$

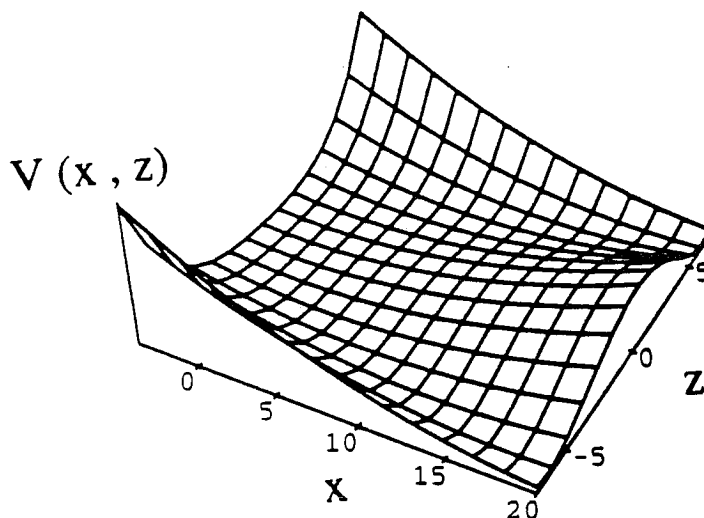


Figure 2.5: Effective potential $V(x, z)$ for the parabolic field model.

From (2.61) we have that particle motion in the parabolic magnetic field can be described in terms of the effective potential

$$V(x, z) = \frac{1}{2} \left(\frac{z^2}{2} - \kappa x \right)^2. \quad (2.67)$$

For a given value of x , $V(x, z)$ has the same topology as $V(z)$ of Section 2.1 with κx as the bifurcation parameter. Fig. 2.5 is a plot of the potential $V(x, z)$. As x is changed, $V(x, z)$ suffers a bifurcation from a parabolic-like shape for $x \leq 0$ to a double potential well for $x > 0$.

For $x \leq 0$ the potential $V(x, z)$ reaches its minimum value at $z = 0$ and all the orbits cross the $z = 0$ plane. For $x > 0$ we can have both crossing (C) and noncrossing (N) types of motion. Type C motion occurs when

$$h_z > \frac{1}{2} \kappa^2 x^2 \quad (2.68)$$

and type N motion occurs when

$$h_z < \frac{1}{2}\kappa^2 x^2, \quad (2.69)$$

where

$$h_z = \frac{P_z^2}{2} + \frac{1}{2} \left(\frac{z^2}{2} - \kappa x \right)^2. \quad (2.70)$$

The transition from crossing to noncrossing motion occurs when $h_z = \kappa^2 x^2 / 2$. This dynamical separatrix is termed the CNC separatrix [Burkhart *et al.*, 1991].

The type C and type N motions can be used to classify the different kinds of orbits:

- Trapped orbits correspond to type C orbits which never cross the CNC separatrix. Trapped orbits can be periodic if they close on themselves or quasiperiodic if they never close on themselves. Trapped orbits are also termed ring or bounded integrable orbits.
- Speiser orbits are orbits which cross the separatrix twice. Speiser orbits are injected into the current sheet (N \rightarrow C) where they execute type C motion before being finally ejected (C \rightarrow N) from the current sheet. Speiser orbits are also known as transient orbits.
- Quasi-trapped orbits perform multiple crossings from the separatrix, that is, their motion alternates between type C and type N motion and eventually they are ejected from the separatrix. Quasi-trapped orbits are also termed unbounded stochastic or cucumber orbits.

Fig. 2.6 is a three-dimensional plot of a trapped orbit for the modified Harris sheet model of Eq. (2.60) with $\kappa = 0.18$ and $b_z = 0.05$. The projection of

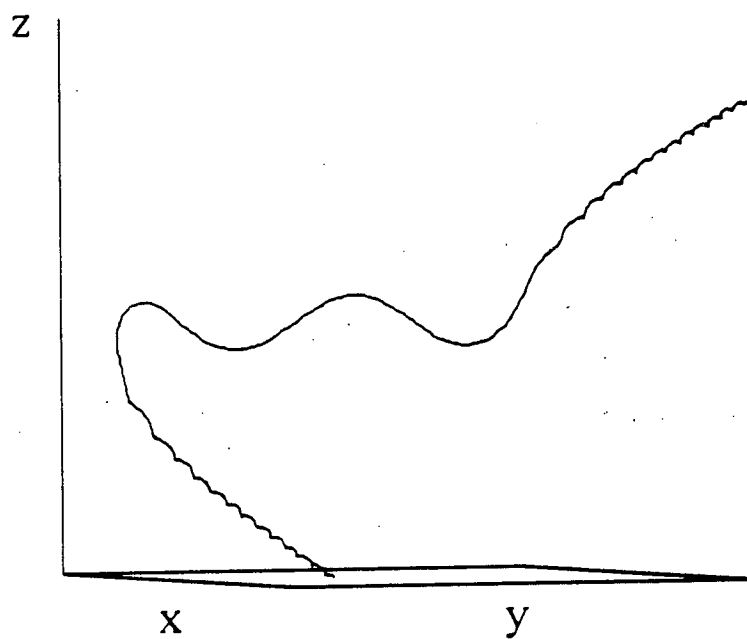


Figure 2.8: Three-dimensional view of a transient orbit with $\kappa = 0.18$ and $b_z = 0.05$.

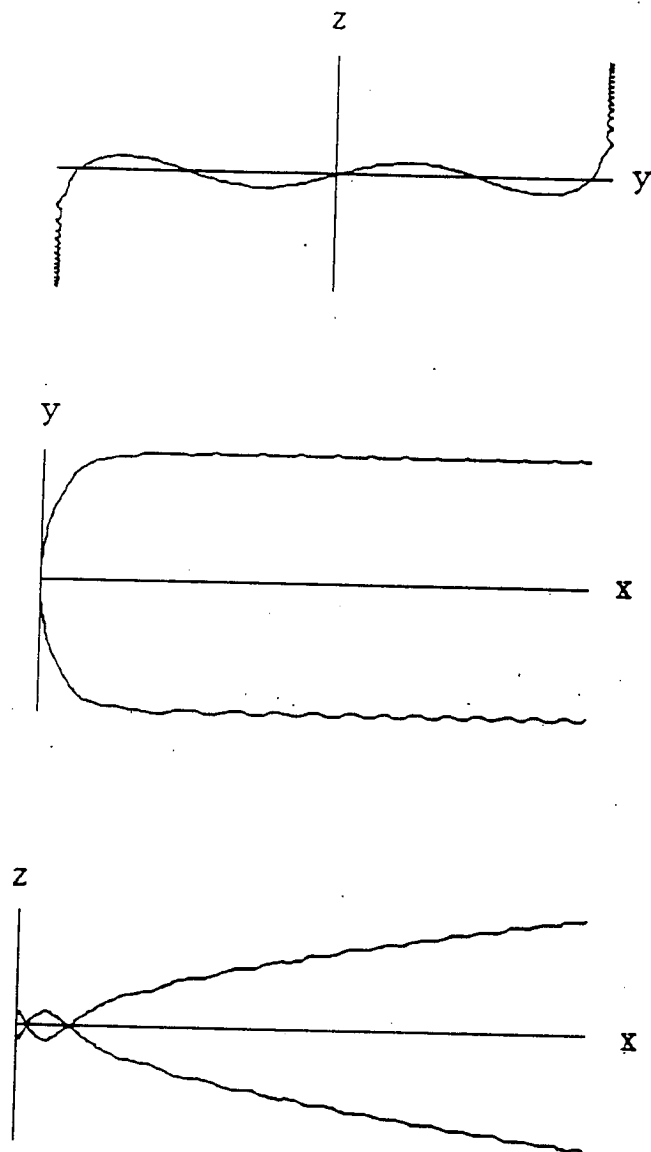


Figure 2.9: Planar projections of a transient orbit in configuration space: (a) $y-z$ projection, (b) $x-y$ projection, and (c) $x-z$ projection.

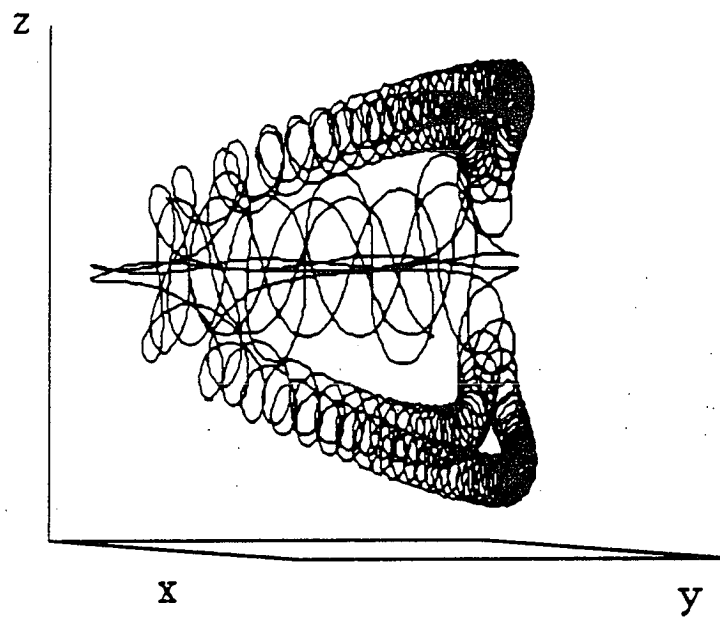


Figure 2.10: Three-dimensional view of a quasi-trapped orbit with $\kappa = 0.18$ and $b_z = 0.05$.

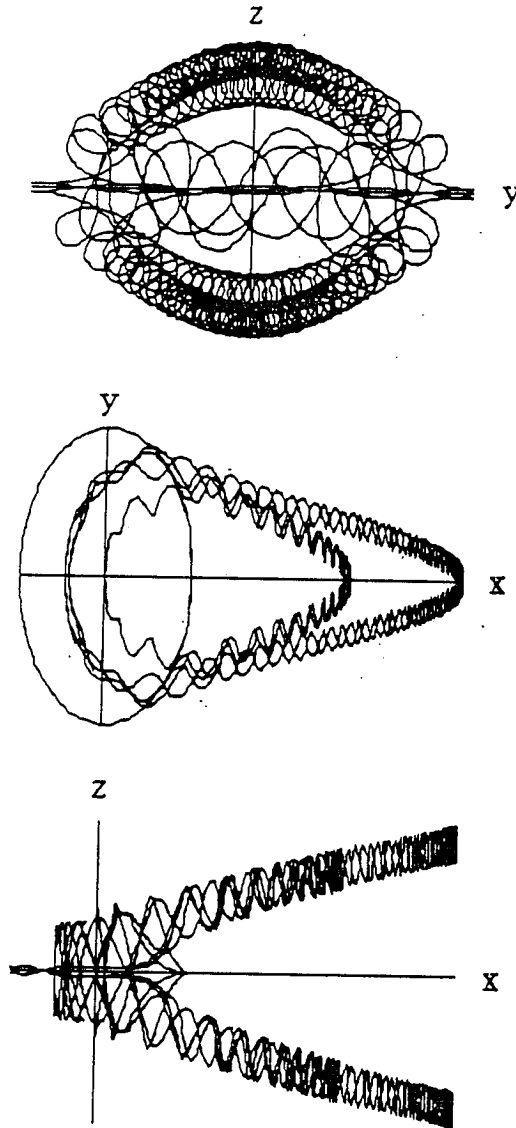


Figure 2.11: Planar projections of a quasi-trapped orbit in configuration space: (a) $y-z$ projection, (b) $x-y$ projection, and (c) $x-z$ projection.

Sonnerup, 1971] the existence of the current sheet adiabatic invariant

$$I_z = \frac{1}{2\pi} \oint P_z dz, \quad (2.71)$$

where the integral is taken over one complete oscillation. The results [*Büchner and Zelenyi, 1989*] for type C and for type N motion are

$$I_C = \frac{8}{3\pi} \kappa (2h_z)^{2/3} f_C(k), \quad (2.72)$$

$$I_N = \frac{4}{3\pi} \kappa (2h_z)^{2/3} f_N(k), \quad (2.73)$$

$$f_C(k) = (1 - k^2)K(k) + (2k^2 - 1)E(k), \quad (2.74)$$

$$f_N(k) = 2(1 - k^2)kK(1/k) + (2k^2 - 1)kE(1/k), \quad (2.75)$$

$$k = \sqrt{\frac{1}{2} \left(1 + \frac{\kappa x}{\sqrt{2h_z}} \right)}, \quad (2.76)$$

where h_z is defined in (2.70), and where $K(k)$ and $E(k)$ are the complete elliptic integrals of the first and of the second kind, respectively. The form parameter k for crossing motion satisfies $k < 1$, for separatrix motion satisfies $k = 1$, and for noncrossing motion satisfies $k > 1$. Fig. 2.12 is a plot of $f_C(k)$ for $k < 1$ and of $f_N(k)$ for $k > 1$.

For $\kappa \ll 1$ the current sheet action (2.71) is a good adiabatic invariant for both crossing and noncrossing motion. When the cyclotron frequency becomes comparable to the nonlinear oscillation frequency ($\kappa \sim 1$) it is no longer possible to define an adiabatic invariant and the system is chaotic.

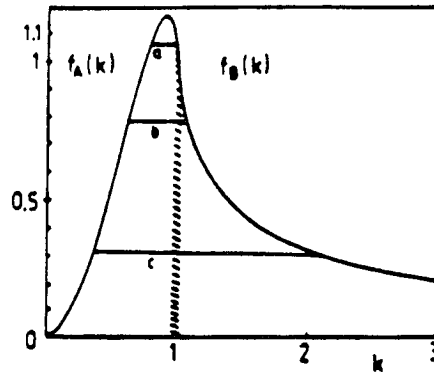


Figure 2.12: Plot of $f_C(k)$ for $k < 1$ and of $f_N(k)$ for $k > 1$ (from *Büchner and Zelenyi* [1989]).

2.2.3 Surface of Section Plots and Orbit Classification

Surface of section plots or Poincaré sections are a powerful tool for obtaining a geometrical description of the phase space structure of low-dimensional dynamical systems. Fig. 2.13 is a surface of section plot for the modified Harris sheet model with $\kappa = 0.18$ ($\hat{H}_{CP} = 500$). The plot was generated by direct numerical integration of the motion for a set of $N = 1000$ particles, which at $t = 0$ were uniformly distributed along the x -axis with $z = 0$, with a dot in the $x - P_x$ plane each time a particle crossed the equatorial plane. Surface of section plots for the modified Harris sheet were first obtained by *Chen and Palmadesso* [1986].

The salient feature of the surface of section in Fig. 2.13 is the partitioning of the phase space into three different regions: A, B, and C. Trajectories in region A are bounded integrable or ring orbits. Integrable orbits are confined to the current sheet region, never cross the separatrix, and their orbital excur-

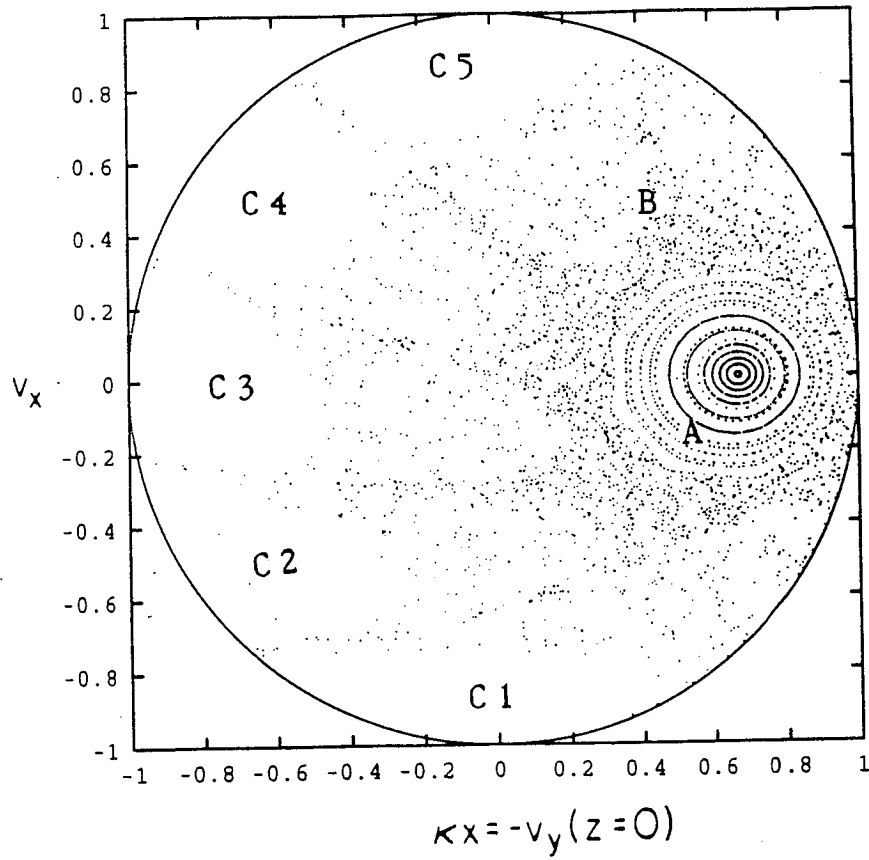


Figure 2.13: Surface of section plot for the parabolic field reversal with $b_z = 0.05$ and $\kappa = 0.18$ ($\hat{H}_{CP} = 500$).

sions along the z -axis are bounded by the constraint $|\Delta Z| \leq (2\rho L_z)^{1/2}$. Orbits in region B are unbounded stochastic or cucumber orbits. These orbits enter and leave the midplane several times before being finally ejected away from the midplane. Orbits in the escape region C are transient or Speiser orbits and they enter and leave the midplane only once, that is, they cross the separatrix only twice. Escape regions such as C are a characteristic of unbounded Hamiltonian systems. The outer circle in Fig. 2.13 corresponds to the intersection of the energy surface $H = E$ and the surface of section $z = 0$.

2.3 Liapunov Exponents

Surface of section plots are geometrical tools useful for gaining qualitative insight on the phase space structure of low-dimensional dynamical systems. Using this approach we can explore the regions that exhibit regular and chaotic motion, we can find out whether or not to expect additional constants of motion, and we can determine the values of the parameters that signal the onset of widespread chaos. However, surface of section plots do not provide us with quantitative information on the “degree of stochasticity” of the system.

It is well known that the separation between two trajectories with nearby initial conditions grows roughly linearly for integrable motion and exponentially for chaotic motion. In fact, this sensitivity to the initial conditions limits our predictive power about the future state of the system. A widely used approach to quantify the degree of stochasticity of a given dynamical system is the method of Liapunov characteristic exponents (see *Lichtenberg and Lieberman* [1983] and references therein).

Consider a dynamical system governed by the system of d coupled

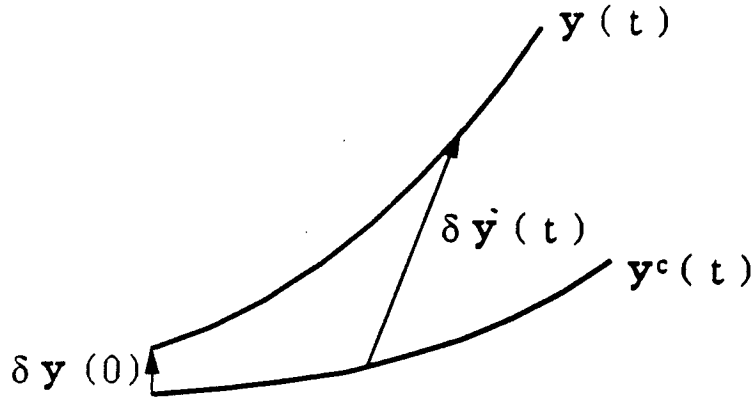


Figure 2.14: Evolution of the separation vector $\delta y(t)$ in phase space.

ordinary differential equations

$$\dot{y}_i = f_i(y), \quad i = 1, \dots, d. \quad (2.77)$$

We want to describe the evolution of the separation (tangent) vector $\delta y(t)$ between the reference or central phase space trajectory $y^c(t)$ with initial conditions $y^c(t=0) = y_0^c$ and another trajectory (or bundle of trajectories) $y(t)$ with nearby initial conditions $y(t=0) = y_0^c + \delta y_0$, as illustrated in Fig. 2.14. The (largest) Liapunov exponent λ is given by the average exponential separation rate between two trajectories with nearby initial conditions

$$\lambda(y_0^c, \delta y) = \lim_{t \rightarrow \infty} \frac{1}{t} \ln \frac{\|\delta y(t)\|}{\|\delta y(0)\|}. \quad (2.78)$$

2.3.1 Tangent Flow

Substituting $\mathbf{y}(t)$ and $\mathbf{y}^c(t)$ into (2.77) and linearizing the difference, we obtain

$$\delta\dot{\mathbf{y}}(t) = \mathbf{K}(t) \cdot \delta\mathbf{y}(t), \quad (2.79)$$

where

$$\mathbf{K}(t) = \left(\frac{\partial \mathbf{f}}{\partial \mathbf{y}} \right)_{\mathbf{y}=\mathbf{y}^c(t)} \quad (2.80)$$

is the Jacobian matrix of \mathbf{f} .

The formal solution to (2.79) is

$$\delta\mathbf{y}(t) = \left[\hat{\mathbf{T}} \exp \int_0^t dt' \mathbf{K}(t') \right] \delta\mathbf{y}(0) \equiv \mathbf{U}(t) \delta\mathbf{y}(0), \quad (2.81)$$

where the time ordering operator $\hat{\mathbf{T}}$ [*e.g.*, Sakurai, 1985] has to be introduced because the matrices $\mathbf{K}(t)$ and $\mathbf{K}(t')$ do not commute in general for $t \neq t'$. The Liapunov characteristic exponents $\lambda_1, \dots, \lambda_d$ are defined as

$$(\lambda_1, \lambda_2, \dots, \lambda_d) = \lim_{t \rightarrow \infty} \frac{1}{t} \ln \|\text{eigenvalues of } \mathbf{U}(t)\|. \quad (2.82)$$

Expanding $\delta\mathbf{y}(0)$ in terms of the eigenvectors $\{\hat{\mathbf{e}}_j\}$ of $\mathbf{U}(t)$,

$$\delta\mathbf{y}(0) = \sum_{j=1}^d a_j \hat{\mathbf{e}}_j; \quad a_j = \delta\mathbf{y}(0) \cdot \hat{\mathbf{e}}_j, \quad (2.83)$$

we obtain from (2.81)

$$\|\delta\mathbf{y}(t)\| = \left\| \sum_{j=1}^d a_j e^{(\lambda_j + i\theta_j)t} \right\| \propto e^{\lambda t} \text{ for } t \rightarrow \infty, \quad (2.84)$$

where θ_j is the phase of the j -th eigenvalue of $\mathbf{U}(t)$. Let e^λ be the largest eigenvalue of $\mathbf{U}(t)$. The value $e^{\lambda t}$ dominates the sum (2.84) because the remaining terms decay as $\exp[-(\lambda - \lambda_j)t]$.

Since in the direction along the flow, $\delta\mathbf{y}(t)$ grows linearly with time, at least one of the Liapunov exponents must vanish. For Hamiltonian systems with N degrees of freedom, the Liapunov exponents have the following symmetry:

$$\lambda_j = -\lambda_{2N-j+1}, \quad j = 1, 2, \dots, 2N. \quad (2.85)$$

This symmetry is a consequence of the phase space volume-preserving property: if the system is expanding along one direction, then it must be contracting along a different direction. For Hamiltonian systems we have $\sum_{j=1}^{2N} \lambda_j = 0$, and for integrable Hamiltonian systems we have $\lambda_j = 0$ for all j .

The characteristic exponent λ is a global measure (computed for the whole trajectory $\mathbf{y}_c(t)$) of the instability of the system. However, λ does not provide us with information about the local stability of the system.

We introduce the local instability index $\nu_m(t)$ in the following way.

Assume

$$\delta\mathbf{y}(t) = \delta\mathbf{y}_0 \exp\left\{\int_0^t dt' \nu(t')\right\}. \quad (2.86)$$

Substituting (2.86) into (2.79) we find that the ν 's are the eigenvalues of the Jacobian matrix $\mathbf{K}(t)$. We define the local instability index $\nu_m(t)$ as the eigenvalue of $\mathbf{K}(t)$ with the largest real part. If $\nu_m(t)$ is purely imaginary, then $\mathbf{y}(t)$ is performing cyclotron-like motion about $\mathbf{y}^c(t)$. On the other hand, if $\text{Re } \nu_m(t) > 0$ (< 0), then the divergence (contraction) is exponential and the motion is locally unstable which can lead to overall chaotic motion.

When the central trajectory $\mathbf{y}^c(t)$ is a closed or periodic function of t with period T , $\mathbf{y}^c(t) = \mathbf{y}^c(t + T)$, the Jacobian matrix is a $d \times d$, T -periodic matrix. In this case, it can be shown that any solution of Eq. (2.79) can be

written in the form

$$\mathbf{X}(t) = \mathbf{A}(t)e^{t\mathbf{R}}; \quad \mathbf{A}(t) = \mathbf{A}(t + T), \quad (2.87)$$

where \mathbf{X} , \mathbf{A} , and \mathbf{R} are $d \times d$ matrices. From Eq. (2.87), we have

$$\mathbf{X}(t + T) = \mathbf{X}(t)e^{T\mathbf{R}}. \quad (2.88)$$

Thus, the evolution of the tangent flow in the neighborhood of the reference trajectory $\mathbf{y}^c(t)$ is determined by the eigenvalues of the constant matrix $e^{T\mathbf{R}}$. These eigenvalues are the characteristic Floquet multipliers [e.g., *Guckenheimer and Holmes*, 1983].

To compute λ , given an initial separation $\delta\mathbf{y}(0)$, Eq. (2.79) for $\delta\mathbf{y}(t)$ is integrated numerically, then the norm of the tangent vector $\|\delta\mathbf{y}(t)\|$ is obtained and the result is substituted into (2.78).

2.3.2 Benettin et al. Method

When the tangent flow method is applied, care must be exerted because numerical overflow can occur if $\|\delta\mathbf{y}(t)\|$ increases exponentially with t . In order to overcome this difficulty, a second method [*Benettin et al.*, 1976] can be used that is based on the original nonlinear equation (2.77). In this method one calculates the divergence of nearby trajectories by direct integration of (2.77) for finite time steps τ , renormalizes $\mathbf{y}(j\tau) - \mathbf{y}^c(j\tau)$, $j = 1, 2, \dots$, to unity after each time step, and takes the average

$$\lambda_N = \frac{1}{N\tau} \sum_{j=1}^N \ln \|\mathbf{y}(j\tau) - \mathbf{y}^c(j\tau)\|. \quad (2.89)$$

The *Benettin et al.* [1976] method is illustrated in Fig. 2.15.

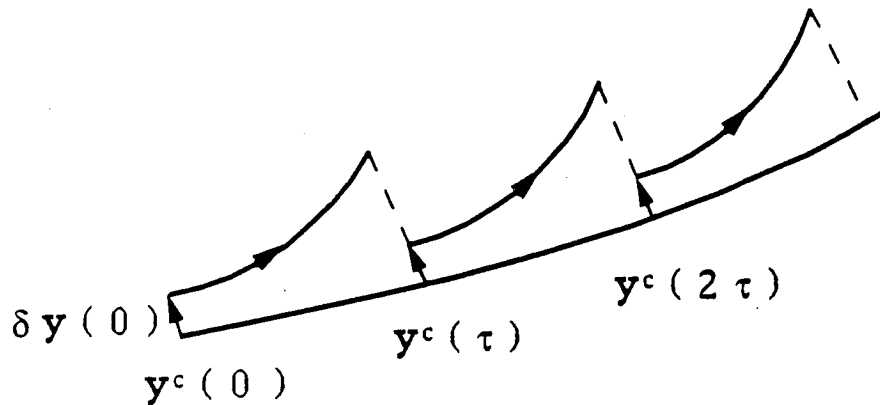


Figure 2.15: Numerical calculation of the largest Liapunov exponent (after *Benettin et al.* [1976]).

In the following sections we consider the Liapunov exponents and the local instability index for the standard mapping, for the *Hénon and Heiles* [1964] system, and for parabolic magnetic field reversal.

2.3.3 Standard Mapping

In order to show how the value of λ is computed, consider for example the standard mapping [*Chirikov*, 1979]

$$I_{n+1} = I_n + K \sin \theta_n,$$

$$\theta_{n+1} = \theta_n + I_{n+1}, \quad (2.90)$$

where K is the stochasticity parameter and the integer $n = 0, \pm 1, \pm 2, \dots$ labels the discrete time step.

The separation vector between two nearby points,

$$\delta \mathbf{y}_n = \begin{pmatrix} \delta I_n \\ \delta \theta_n \end{pmatrix}, \quad (2.91)$$

evolves according to the linearized mapping

$$\delta \mathbf{y}_{n+1} = \mathbf{K}(n) \cdot \delta \mathbf{y}_n, \quad (2.92)$$

where the Jacobian matrix is given by

$$\mathbf{K}(n) = \begin{pmatrix} 1 & K \cos \theta_n \\ 1 & 1 + K \cos \theta_n \end{pmatrix}. \quad (2.93)$$

The matrix $\mathbf{K}(n)$ describes the local linear stability of a fixed point if \mathbf{y}^c is a fixed point and determines λ if $\mathbf{y}^c(n)$ is a trajectory.

The eigenvalues of $\mathbf{K}(n)$ are given by

$$\mu_{\pm}(n) = 1 + \frac{k_n}{2} \pm \sqrt{k_n \left(1 + \frac{k_n}{4}\right)}, \quad (2.94)$$

where

$$k_n \equiv K \cos \theta_n, \quad (2.95)$$

and they satisfy the relation

$$\mu_+(n)\mu_-(n) = 1, \quad (2.96)$$

necessary to preserve the phase space volume. On the other hand, the eigenvalues (2.94) depend on the time step n ; that is, in order to determine the Liapunov characteristic exponents, it is necessary to solve for the evolution of θ_n . However, *Chirikov* [1979] considered the calculation of the Liapunov exponents for two special cases: fixed points and the $K \gg 1$ limit.

The standard mapping (2.90) has period-1 fixed points at $(I, \theta) = (2\pi n, 0)$ and $(2\pi n, \pi)$. At the period-1 fixed points the Jacobian matrix takes the form

$$\mathbf{K} = \begin{pmatrix} 1 & k \\ 1 & 1+k \end{pmatrix}, \quad (2.97)$$

with $k = K$ for the $\theta = 0$ fixed point and with $k = -K$ for the $\theta = \pi$ fixed point. The eigenvalues (2.94) of \mathbf{K} are now given by

$$\mu_{\pm} = 1 + \frac{k}{2} \pm \sqrt{k \left(1 + \frac{k}{4} \right)}. \quad (2.98)$$

For $-4 < k < 0$ the eigenvalues are complex numbers and $|\mu_{\pm}| = 1$, that is, the eigenvalues are located on the unit circle, which means that the motion is locally stable. For $k > 0$ the eigenvalues lie on each side of the unit circle with $|\mu_{+}| > 1$ and $|\mu_{-}| < 1$, and the motion is locally unstable. Both situations are illustrated in Fig. 2.16.

For the period-1 fixed points the tangent vector is given in terms of the eigenvectors \hat{e}_{\pm} of \mathbf{K} by

$$\delta \mathbf{y}_n = u_n \hat{e}_+ + v_n \hat{e}_- \quad (2.99)$$

with

$$u_n = u_0 \mu_+^n = u_0 e^{n\lambda_+}, \quad v_n = v_0 \mu_-^n = v_0 e^{n\lambda_-}. \quad (2.100)$$

For $|\mu_{+}| > 1$ and $|\mu_{-}| < 1$ the eigenvectors \hat{e}_+ and \hat{e}_- define the directions of dilation and contraction, respectively.

For $K \gg 1$ *Chirikov* [1976] pointed out that $k = K \cos \theta$ is large except in narrow stable phase intervals, made the approximation $|\mu_{+}| \approx |k| =$

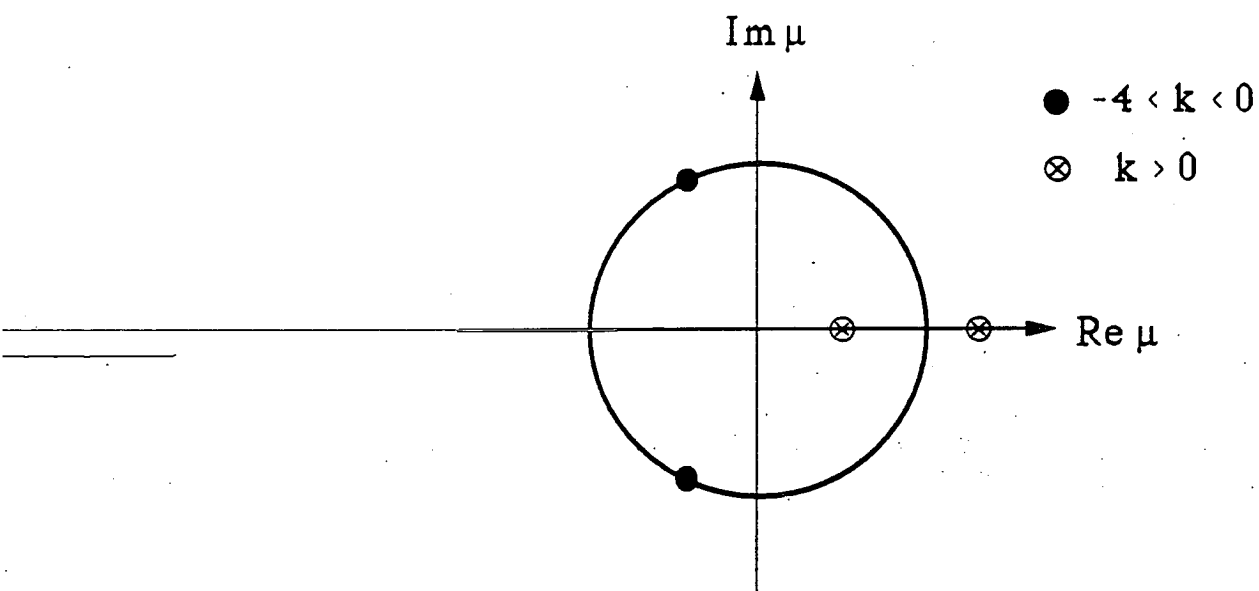


Figure 2.16: Eigenvalues of \mathbf{K} for the standard mapping. For $-4 < k < 0$ the eigenvalues of \mathbf{K} for the period-1 fixed points are located on the unit circle (dots). For $k > 0$ the motion is locally unstable and the eigenvalues are located on both sides of the unit circle.

$K|\cos\theta|$, and estimated the value of the largest Liapunov exponent by averaging $\ln|\mu_+(\theta)|$ over the phase:

$$\lambda_+ = \langle \ln|\mu_+(\theta)| \rangle = \frac{1}{2\pi} \int_0^{2\pi} d\theta \ln(K|\cos\theta|) = \ln \frac{K}{2}. \quad (2.101)$$

Chirikov [1976] found good agreement between Eq. (2.101) and the numerically calculated λ_+ for $K \gtrsim 4$. In particular, for $K = 6.21$ the theoretical estimated value obtained from (2.101) is $\lambda_{+T} = 1.133$ and the numerically obtained value is $\lambda_+ = 1.164$, giving a ratio $\lambda_+/\lambda_{+T} = 1.027$.

2.3.4 Hénon-Heiles System

In order to illustrate the usefulness of the local instability index, consider the *Hénon and Heiles* [1964] system with the Hamiltonian given by

$$H = \frac{P_x^2}{2} + \frac{P_y^2}{2} + \frac{1}{2} \left(x^2 + y^2 + 2x^2y - \frac{2}{3}y^3 \right). \quad (2.102)$$

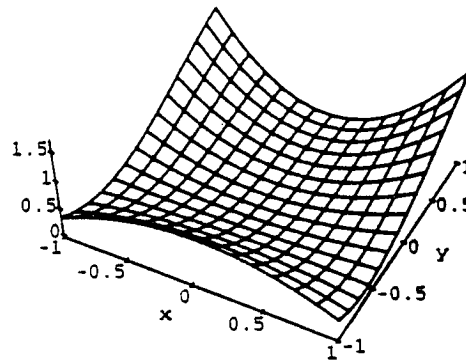
The *Hénon and Heiles* potential is shown in Fig. 2.17: curve (a) shows the functional dependence of U on x and y , and curve (b) the isopotential lines for U .

For the system (2.102) the equations of motion are given by

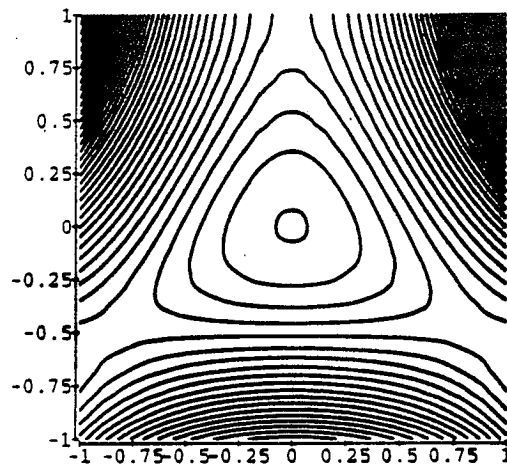
$$\dot{\mathbf{y}} = \begin{pmatrix} \dot{x} \\ \dot{P}_x \\ \dot{y} \\ \dot{P}_y \end{pmatrix} = \begin{pmatrix} P_x \\ -x - 2xy \\ P_y \\ -x^2 - y + y^2 \end{pmatrix} \quad (2.103)$$

and the Jacobian matrix is

$$\mathbf{K} = \begin{pmatrix} 0 & 1 & 0 & 0 \\ -1 - 2y & 0 & -2x & 0 \\ 0 & 0 & 0 & 1 \\ -2x & 0 & -1 + 2y & 0 \end{pmatrix} \quad (2.104)$$



(a)



(b)

Figure 2.17: Potential U for the Hénon and Heiles problem: (a) The Hénon and Heiles potential, (b) contour lines for U .

with the eigenvalues given by

$$\nu(t) = \pm(-1 \pm 2r(t))^{1/2}, \quad (2.105)$$

where

$$r(t) \equiv \sqrt{x^2(t) + y^2(t)}. \quad (2.106)$$

From (2.105) we have that the motion is neutral for $r \leq 1/2$ and that local instability occurs for $r > 1/2$. Writing the *Hénon and Heiles* potential in polar coordinates

$$U(r, \theta) = \frac{r^2}{2} + \frac{r^3}{3} \sin(3\theta), \quad (2.107)$$

we have that for fixed r the potential has a minimum value at $\theta = 3\pi/2$. In particular, for $r = 1/2$ (the stability-instability border), we have $U_{min}(r = 1/2) = 1/12$. Thus, if the system exhibits chaotic motion, then its energy must be $E > 1/12$. Widespread chaotic motion in the *Hénon and Heiles* system occurs for $E \geq 1/8$ [*Hénon and Heiles*, 1964].

2.3.5 Local Instability for Parabolic Field Reversals

Consider now particle motion in the parabolic magnetic field model with the Hamiltonian of Eq. (2.61). With the vector \mathbf{y} defined as

$$\mathbf{y} = \begin{pmatrix} x \\ P_x \\ z \\ P_z \end{pmatrix}, \quad (2.108)$$

the equations of motion are given by

$$\dot{\mathbf{y}} = \begin{pmatrix} P_x \\ \kappa \left(\frac{z^2}{2} - \kappa x \right) \\ P_z \\ - \left(\frac{z^2}{2} - \kappa x \right) z \end{pmatrix}, \quad (2.109)$$

and the Jacobian matrix is given by

$$\mathbf{K} = \begin{pmatrix} 0 & 1 & 0 & 0 \\ -\kappa^2 & 0 & \kappa z & 0 \\ 0 & 0 & 0 & 1 \\ \kappa z & 0 & -\frac{3}{2}z^2 + \kappa x & 0 \end{pmatrix}. \quad (2.110)$$

The local eigenvalues of \mathbf{K} are the roots of the characteristic equation

$$\nu^4 + d\nu^2 + c = 0, \quad (2.111)$$

where

$$d(t) = \frac{3}{2}z^2 - \kappa x + \kappa^2 \quad (2.112)$$

and

$$c(t) = \kappa^2 \left(\frac{z^2}{2} - \kappa x \right) = \kappa^2 v_y(t). \quad (2.113)$$

The characteristic equation (2.111) has four roots,

$$\nu^2(t) = \frac{1}{2} \left[-d(t) \pm \sqrt{d^2(t) - 4c(t)} \right], \quad (2.114)$$

occurring in pairs $(\nu_1, -\nu_1)$ and $(\nu_2, -\nu_2)$ to preserve phase space volume, and the local instability index ν_m is given by the root with the largest real part

$$\nu_m^2(t) = \frac{1}{2} \left[-d(t) + \sqrt{d^2(t) - 4c(t)} \right]. \quad (2.115)$$

The condition for the system being unstable is $c(t) = \kappa^2 v_y(t) < 0$. This condition is in agreement with the equation of motion

$$\ddot{z} = -v_y(t)z, \quad (2.116)$$

which indicates that for $v_y(t) > 0$ the particle oscillates about $z = 0$ and for $v_y(t) < 0$ the particle is ejected from the current sheet. Fig. 2.18 is a plot

on the complex plane of the eigenvalues of \mathbf{K} for (a) $c > 0$, (b) $c = 0$, and (c) $c < 0$. In all the above cases we have used $\kappa = 0.18$ and $z = 0$. In case (a) we have computed the eigenvalues for $v_y = 1/2$, and in case (c), the unstable case, we use $v_y = -1/2$.

Fig. 2.19 is a plot of ν_m^2 as a function of x and z for $\kappa = 0.25$. The local instability index ν_m^2 can be positive only in the quasineutral layer (the unstable region) and reaches a maximum at $z = 0$ where separatrix crossing occurs.

In the $b_z \rightarrow 0$ limit the magnetic field configuration becomes a straight field reversal where the charged particle motion is integrable. In this limit $\kappa = b_z/\epsilon^{1/2} \rightarrow 0$ and from (2.112) and (2.113) we have that $c(t) \rightarrow 0$, $d(t) \rightarrow 3z^2(t)/2$. The characteristic equation (2.111) has two roots equal to zero and two purely imaginary roots given by $\nu(t) = \pm i\sqrt{\frac{3}{2}}|z(t)|$, as expected for integrable motion.

Now consider the local instability index or local divergence-contraction rate ν_m and the largest Liapunov exponent λ for the parabolic field reversal. We can find an upper bound for λ by noting that the maximum value of ν_m^2 occurs for $(\kappa x, z) = (1, 0)$ where $\nu_{max}^2 = 1$ (remember that we are using the rescaled variables of Eq. (2.58), where the time is given in units of $\omega_{b_z}^{-1}$ and where the spatial lengths are given in units of $(\rho L_z)^{1/2}$). In taking the bound on κx we are using that, for $z = 0$, the maximum possible value of κx in Eq. (2.61) occurs for $P_x = P_z = 0$. We can also obtain this result by noting that ν_m^2 can be positive only for $|z|/L_z \ll 1$ where $\nu_m \approx \sqrt{\kappa x}$ with $x > 0$. On the other hand, in the equatorial plane ($z = 0$) we have

$$\ddot{x} = -\kappa^2 x; \quad (2.117)$$

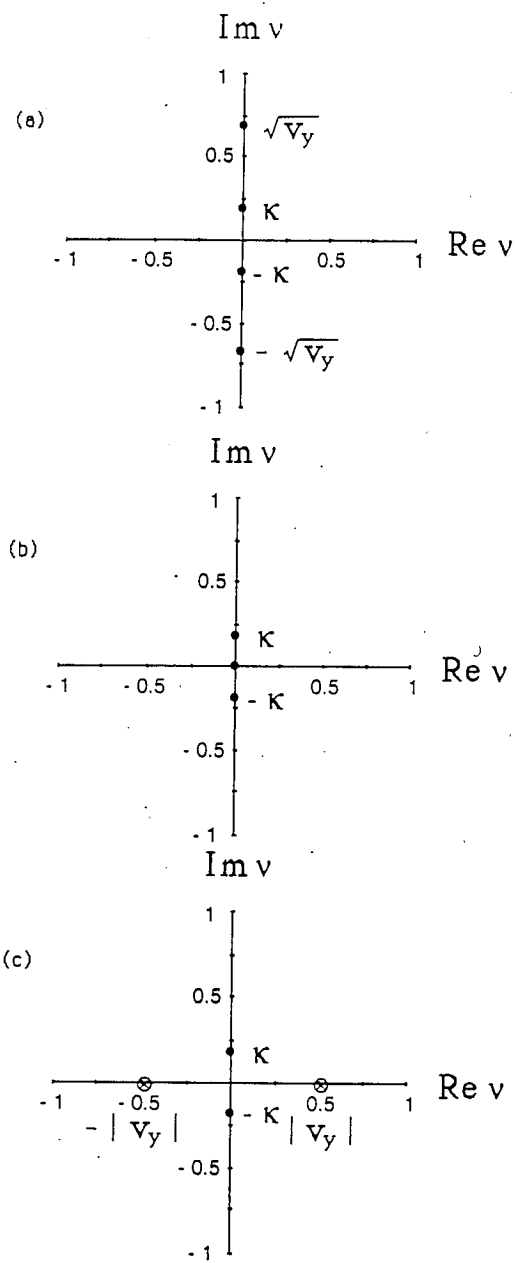


Figure 2.18: Roots of the characteristic equation (2.111). (a) $v_y = 1/2$, (b) $v_y = 0$, (c) $v_y = -1/2$. The eigenvalues are shown for $z = 0$ and $\kappa = 0.18$.

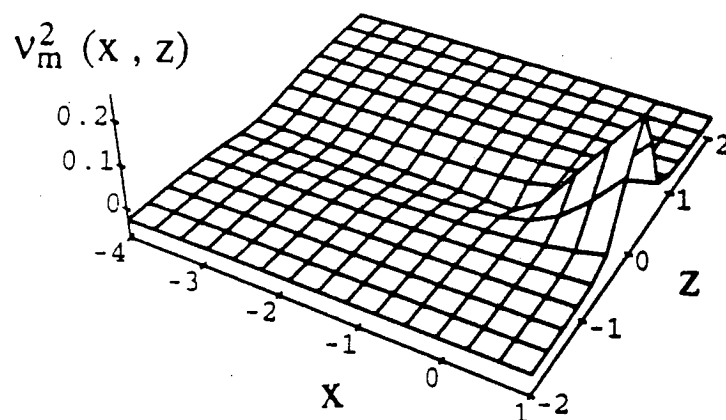


Figure 2.19: Local instability index $\nu_m^2(x, z)$ for parabolic field reversals. The plot was generated from (2.115) with $\kappa = 0.25$.

that is, at $z = 0$, the value of x alternates between x_{max} and $-x_{max}$, where $x_{max} > 0$, with period $\Delta T = 2\pi/\kappa$. Approximating

$$x_{max} \approx \frac{v}{\omega_{cz}} = \frac{\rho}{b_z} \quad (2.118)$$

and noting that in the dimensionless variables (2.58) $\rho \rightarrow \epsilon^{1/2}$, we have

$$x_{max} = \frac{1}{\kappa} \quad (2.119)$$

and

$$\nu_{max} = \sqrt{\kappa x_{max}} = 1. \quad (2.120)$$

The largest Liapunov exponent λ and the local instability index $\nu_m(t)$ are related by

$$\lambda = \lim_{T \rightarrow \infty} \int_0^T \frac{dt}{T} \nu_m(t) \leq \nu_{max} = 1. \quad (2.121)$$

Thus, if the motion is chaotic the upper bound for λ is $\lambda \leq 1$. For the reference parameters of Table 1.1 $\lambda \leq \omega_{bz} \leq (\pi/10)^{-1} \text{ s}^{-1}$.

It is important to note that local instability does not imply global chaos. However, if the motion is chaotic, an upper bound for the largest Liapunov exponent can be found if we can determine the maximum value of the local instability index. This way of estimating an upper bound for λ must be contrasted with the usual numerical calculation of λ by either the Benettin et al. method or by direct integration of Eq. (2.79).

In general, except for ring orbits, the charged particles do not remain indefinitely trapped in the current sheet, but stream towards the Earth after crossing the mid-plane ($z = 0$) several times. It is during these crossings of the equatorial plane that the local instability index can take finite values, that is, the spectrum of $\nu_m(t)$ exhibits periods of instability bursts. For this reason it is appropriate to describe the local instability of the system by estimating the number of e -foldings during one current sheet traversal, $\Lambda = \nu_m \Delta T$, where ΔT is the time during which the particles remain in the current sheet region, and by computing the quantity $\Sigma = \lambda \Delta T / \text{number of bursts during the time period } \Delta t = [t_1, t_2]$.

For the parabolic field model (1.34) the time spent in the unstable region can be estimated by the cyclotron period of gyration around B_z , $\Delta T = T_{cz} = 2\pi/\kappa$. Noting that $\nu_m(t) \leq \nu_{max} = 1$, we have

$$\Lambda_{max} = (\nu \Delta T)_{max} \leq \frac{2\pi}{\kappa}. \quad (2.122)$$

On the other hand, we have

$$\kappa = \frac{\omega_{cz}}{\omega_{bz}} = \frac{b_z}{(2H/mv_0^2)^{1/4}} \sim \frac{1}{H^{1/4}}, \quad (2.123)$$

Table 2.1: Expansion Rates for Instability Bursts.

Energy (keV)	Time length $t_2 - t_1$ (hour)	Λ	No. of bursts	Σ
1	0.9	~ 11	2	$\simeq 6$
3	0.8	~ 22	3	$\simeq 7$
30	0.4	~ 21	3	$\simeq 7$

where $v_0 \equiv L_z \omega_{cx0}$. Thus, from (2.122) and (2.123), we expect the local instability Λ to increase with increasing H .

Horton et al. [1991] have calculated Λ and Σ for protons with energies set at 1 keV, 3 keV, and 30 keV in the semi-empirical *Tsyganenko* [1987] model of the magnetosphere for quiet times ($K_p = 1$). The results are shown in Table 2.1. The time intervals $t_2 - t_1$ are chosen such that they are less than a few hours since larger Δt means that the protons are at the Earth region or the magnetopause boundary.

Horton et al. [1991] also computed $\lambda \Delta t$ and Σ for 30 keV protons with $K_p = 6$, which corresponds to a magnetic storm period, and Λ is found to be ~ 34 over half of an hour period and the corresponding $\Sigma \approx 11 \sim 12$, which is twice the expansion rate obtained in quiet times ($K_p = 1$).

Chen [1993] has estimated the local divergence of the particles during the scattering process by the current sheet in the modified Harris model (1.33) as a function of $\hat{H}^{1/4}$, where \hat{H} is defined in (2.65). For this purpose *Chen* introduces a finite-time analogue of the Liapunov exponent by

$$\lambda^* \equiv \frac{1}{\Delta\tau} \sum_{j=1}^L \ln \left(\frac{w_j}{w_0} \right), \quad (2.124)$$

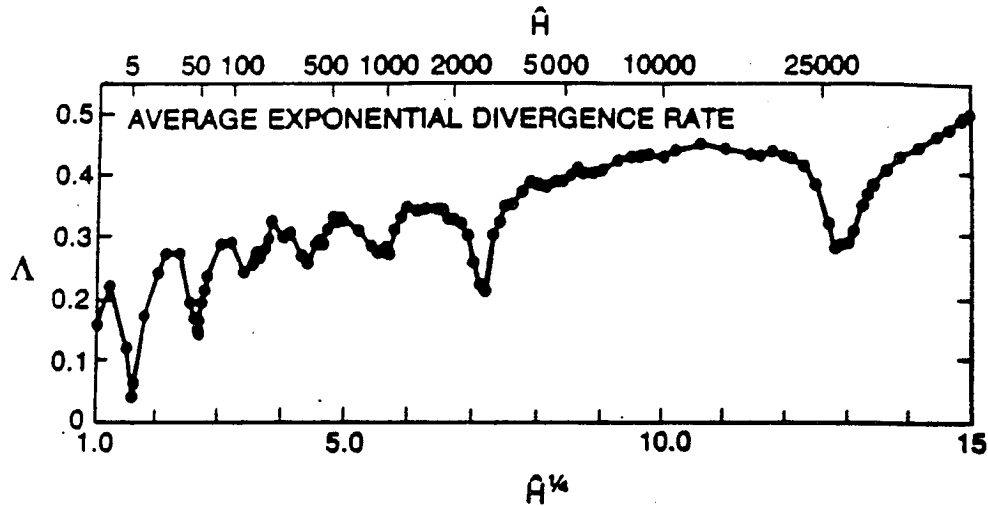


Figure 2.20: Ensemble averaged exponential divergence rate $\langle \lambda^* \rangle$ as a function of \hat{H} (from *Chen* [1993]).

where w_0 is the norm of the initial tangent vector, w_j is the norm of the tangent vector after the j -th time step, $\Delta\tau$ is the time step, and L is the total number of time steps from the first to the last crossing of the equatorial plane. The tangent vector is normalized to the initial norm w_0 after each time step.

Fig. 2.20 (from *Chen* [1993]) is a plot of $\langle \lambda^* \rangle$, where

$$\langle \lambda^* \rangle \equiv \frac{1}{M} \sum_m \lambda_m^*, \quad (2.125)$$

for ensembles of M stochastic particles ($M = 40 - 400$), as a function of $\hat{H}^{1/4}$ and for fixed $b_z = 0.1$.

2.4 Motion in Sheared Parabolic Magnetic Field Reversals

In order to account for the dawn-dusk magnetic field component, B_y , from the interplanetary magnetic field which soaks into the magnetosphere, consider the following model

$$\mathbf{B} = B_{x0} \frac{z}{L_z} \hat{\mathbf{e}}_x + B_y \hat{\mathbf{e}}_y + \hat{\mathbf{e}}_z, \quad (2.126)$$

where $B_y = \text{const.}$ Particle motion in the presence of the magnetic field of Eq. (2.126) has been considered by *Karimabadi et al.* [1990], *Horton et al.* [1991], *Büchner and Zelenyi* [1991], and *Hernández et al.* [1993].

The Hamiltonian for the system in the magnetic field of Eq. (2.126) is given by

$$H = \frac{P_z^2}{2m} + \frac{1}{2m} (P_x - qB_y z)^2 + \frac{1}{2m} \left(P_y + qB_{x0} \frac{z^2}{2L_z} - qB_z x \right)^2. \quad (2.127)$$

For vanishing B_z , the system has three constants of motion (H, P_x, P_y) and is integrable. However, for $B_z \neq 0$ there are only two constants of motion (H, P_y) and the system may become chaotic, depending on the value of B_z and on the total energy.

From (2.127) the equations of motion are given by

$$\dot{x} = \frac{P_x}{m} - \omega_{cy} z, \quad (2.128)$$

$$\frac{\dot{P}_x}{m} = \omega_{cz} \dot{y}, \quad (2.129)$$

$$\dot{y} = \frac{P_y}{m} + \omega_{cx0} \frac{z^2}{2L_z} - \omega_{cz} x, \quad (2.130)$$

$$\frac{\dot{P}_y}{m} = 0, \quad (2.131)$$

$$\dot{z} = \frac{P_z}{m}, \quad (2.132)$$

$$\frac{\dot{P}_z}{m} = \omega_{cy}\dot{x} - \omega_{cx0}\frac{z}{L_z}\dot{y}. \quad (2.133)$$

In particular, combining (2.130), (2.132), and (2.133) we get

$$\ddot{z} + \omega_{cx0} \left(\frac{P_y}{m} - \omega_{cz}x \right) \frac{z}{L_z} + \omega_{cx0} \frac{z^2}{2L_z^3} = \omega_{cy}\dot{x}, \quad (2.134)$$

which has the form of a nonlinear Mathieu equation with a driving term $\omega_{cy}\dot{x}$. The equations of motion (2.128)–(2.133) are symmetric under the simultaneous transformation

$$x \rightarrow x, \quad z \rightarrow -z \quad \text{and} \quad B_y \rightarrow -B_y. \quad (2.135)$$

Charged particle motion can be described in terms of the guiding center approximation when the magnetic field is slowly varying over the size of the orbit. Consider in particular the curvature vector κ_c . The curvature vector for the magnetic field lines is given by

$$\begin{aligned} \kappa_c &= \mathbf{b} \cdot \nabla \mathbf{b} \\ &= \frac{b_z}{L_z \left(\frac{z^2}{L_z^2} + b_y^2 + b_z^2 \right)^{3/2}} \left[(b_y^2 + b_z^2) \hat{\mathbf{e}}_x - b_y \frac{z}{L_z} \hat{\mathbf{e}}_y - b_z \frac{z}{L_z} \hat{\mathbf{e}}_z \right] \end{aligned} \quad (2.136)$$

and the minimum curvature radius, which occurs at the equatorial plane, is given by

$$\frac{1}{R_{min}} = \frac{b_z}{L_z(b_y^2 + b_z^2)}, \quad (2.137)$$

where

$$b_y \equiv \frac{B_y}{B_{x0}} \quad \text{and} \quad b_z \equiv \frac{B_z}{B_{x0}}. \quad (2.138)$$

On the other hand, the maximum Larmor radius is given by

$$\rho_{max} = \left(\frac{mv_{th}}{qB} \right)_{z=0} = \frac{v_{th}}{\omega_{cx0}} \frac{1}{\sqrt{b_y^2 + b_z^2}} = \frac{\rho}{\sqrt{b_y^2 + b_z^2}}. \quad (2.139)$$

Comparing (2.137) and (2.139) we have

$$\frac{\rho_{max}}{R_{min}} = \epsilon \frac{b_z}{(b_y^2 + b_z^2)^{3/2}} = \frac{1}{\kappa^2} \frac{b_z^3}{(b_y^2 + b_z^2)^{3/2}}. \quad (2.140)$$

The guiding center approximation is valid when

$$\frac{\rho_{max}}{R_{min}} \ll 1. \quad (2.141)$$

For particle and field parameters such that (2.141) is satisfied, charged particle motion can be described in terms of guiding center drifts. In particular, the curvature drift is given by

$$\begin{aligned} \mathbf{V}_c &= \frac{mv_{\parallel}^2}{qB} (\mathbf{b} \times \boldsymbol{\kappa}_c) \\ &= \frac{v_{\parallel}^2}{\omega_{cx0} L_z} \frac{b_z}{\left(\frac{z^2}{L_z^2} + b_y^2 + b_z^2 \right)^2} (b_z \hat{\mathbf{e}}_y - b_y \hat{\mathbf{e}}_z) \end{aligned} \quad (2.142)$$

and the ∇B -drift is given by

$$\begin{aligned} \mathbf{V}_{\nabla} &= \frac{mv_{\perp}^2}{2qB} \frac{\mathbf{b} \times \nabla B}{B} \\ &= \frac{v_{\perp}^2}{2\omega_{cx0} L_z} \frac{\frac{z}{L_z}}{\left(\frac{z^2}{L_z^2} + b_y^2 + b_z^2 \right)^2} \left(b_y \hat{\mathbf{e}}_x - \frac{z}{L_z} \hat{\mathbf{e}}_y \right). \end{aligned} \quad (2.143)$$

The constant cross-tail field component B_y introduces a north-south curvature drift component and a ∇B -drift along the x -direction.

The orbit classification into transient, quasi-trapped, and trapped orbits remains valid in the $B_y \neq 0$ case. Fig. 2.21 is a plot of an integrable

trajectory for $B_y = B_z$: (a) projection on the $y - z$ -plane, (b) projection on the $x - y$ -plane, and (c) projection on the $x - z$ -plane. As observed in Fig. 2.21, the particles tend to follow the tilted field lines spending longer times in the quasineutral layer, because of the increment on the effective field line length introduced by B_y . As shown in the previous sections, oscillations about the $z = 0$ -plane are bounded by $|z| \leq \Delta \equiv (\rho L_z)^{1/2}$. We can define an effective bound to excursions in the z -direction, Δ_{eff} , by

$$\Delta_{eff} = \int_0^\Delta dz \frac{B(z)}{B_z} \approx \frac{B(z=0)}{B_z} \Delta, \quad (2.144)$$

so that

$$\Delta_{eff} = \left(1 + \frac{b_y^2}{b_z^2}\right)^{1/2} \Delta. \quad (2.145)$$

Furthermore, we define L_{eff} through the relation

$$\Delta_{eff} = (\rho L_{eff})^{1/2}. \quad (2.146)$$

Comparing (2.145) and (2.146) we find

$$L_{eff} = \left(1 + \frac{b_y^2}{b_z^2}\right) L_z. \quad (2.147)$$

Under the above approximations, the effective bounce frequency along the tilted field lines is given by

$$\omega_{bz}^{eff} = \left(\frac{v_{th} \omega_{cz0}}{L_{eff}}\right)^{1/2} = \frac{\omega_{bz}}{\sqrt{1 + \frac{b_y^2}{b_z^2}}}, \quad (2.148)$$

and the cyclotron frequency at $z = 0$ is given by

$$\omega_c = \left(1 + \frac{b_y^2}{b_z^2}\right)^{1/2} \omega_{cz}. \quad (2.149)$$

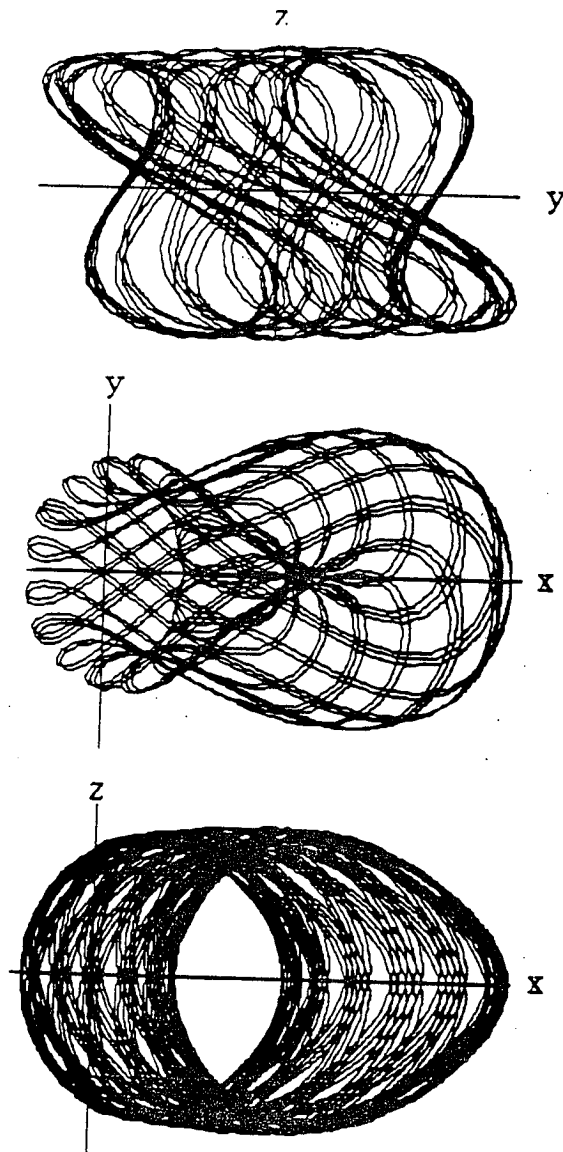


Figure 2.21: Ring orbit in the sheared parabolic magnetic field of Eq. (2.126) with $\kappa = 0.18$ and $b_y = b_z = 0.05$.

From (2.148) and (2.149) the effective nonadiabaticity parameter κ_{eff} is given by

$$\kappa_{eff} = \frac{\omega_c}{\omega_{bz}^{eff}} = \left(1 + \frac{b_y^2}{b_z^2}\right) \kappa. \quad (2.150)$$

In the rescaled variables of Eq. (2.58), the Hamiltonian of Eq. (2.127) takes the form

$$h = \frac{P_z^2}{2} + \frac{1}{2}(P_x - \kappa_y z)^2 + \frac{1}{2} \left(\frac{z^2}{2} - \kappa x \right)^2, \quad (2.151)$$

where

$$\kappa_y \equiv \frac{b_y}{\epsilon^{1/2}}. \quad (2.152)$$

The Jacobian matrix for the system is

$$\mathbf{K} = \begin{pmatrix} 0 & 1 & -\kappa_y & 0 \\ -\kappa^2 & 0 & \kappa z & 0 \\ 0 & 0 & 0 & 1 \\ \kappa z & \kappa_y & -\frac{3}{2}z^2 - \kappa_y^2 + \kappa x & 0 \end{pmatrix} \quad (2.153)$$

and the local eigenvalues of \mathbf{K} are found by solving the characteristic equation

$$\nu^4 + d(t)\nu^2 + c(t) = 0, \quad (2.154)$$

where

$$d(t) = \frac{3}{2}z^2 + \kappa_y^2 + \kappa^2 - \kappa x \quad (2.155)$$

and

$$c(t) = \left(\frac{z^2}{2} - \kappa x \right) \kappa^2 = \kappa^2 v_y(t). \quad (2.156)$$

Comparing Eqs. (2.154)–(2.156) with the corresponding results in Eqs. (2.111)–(2.113) for the case with $B_y = 0$, we observe that the only difference is in the $d(t)$ coefficient of the characteristic equations (2.111) and (2.154). Denoting

the $d(t)$ coefficient for the $B_y = 0$ case as $d_0(t)$, we have that $d(t)$ and $d_0(t)$ are related by

$$d(t) = d_0(t) + \kappa_y^2. \quad (2.157)$$

From (2.154) we have that the local instability index is given by

$$\nu_m^2 = \frac{1}{2} \left[-d(t) + \sqrt{d^2(t) - 4c(t)} \right] \quad (2.158)$$

and the motion is locally unstable if

$$c(t) = \kappa^2 v_y(t) < 0, \quad (2.159)$$

just as in the case with $B_y = 0$.

In the $\kappa \rightarrow 0$ limit, we have $c(t) \rightarrow 0$ and $d(t) \rightarrow \frac{3}{2}z^2 + \kappa_y^2$, and the characteristic equation (2.154) has two roots equal to zero and two purely imaginary roots $\nu(t) = \pm i\sqrt{\frac{3}{2}z^2 + \kappa_y^2}$, as expected for integrable motion.

The local instability index ν_m reaches a maximum value ν_{max} at $(\kappa x, z) = (1, 0)$ where

$$\nu_{max}^2 = \frac{1}{2} \left[1 - (\kappa^2 + \kappa_y^2) + \sqrt{(1 + \kappa^2 + \kappa_y^2)^2 - 4\kappa_y^2} \right]. \quad (2.160)$$

The maximum value of the local instability index can be used to estimate an upper bound of the largest Liapunov exponent λ by noting that

$$\lambda = \lim_{T \rightarrow \infty} \int \frac{dt}{T} \nu_m(t) \leq \nu_{max}, \quad (2.161)$$

where ν_{max} is given by Eq. (2.160). Consider for example the following two cases: (1) $(\kappa_y, \kappa) = (0, 0.18)$ and (2) $(\kappa_y, \kappa) = (5\kappa, \kappa)$, with $\kappa = 0.18$. Substituting these values of κ and κ_y into Eq. (2.160) we find that in the first case, $\nu_{max} = 1$ and in the second case, $\nu_{max} = 0.4$. These values of ν_{max} suggest

that the degree of stochasticity for the case with $B_y = 0$ and $\kappa = 0.18$ is larger than the degree of stochasticity for the case with $B_y = 5B_z$ and $\kappa = 0.18$. This statement can be tested by plotting the surface of section plot for the second case, which is shown in Fig. 2.22, and comparing it with the surface of section plot for the first case, which is shown in Fig. 2.13.

Fig. 2.23 is a Poincaré section in the equatorial ($z = 0$) plane for $b_y/b_z = 1$. The effect of $b_y \neq 0$ on the phase space structure can be accounted for in the following way: For $b_y \ll b_z$ the phase space structure remains the same as that described in Section 2.2 for $b_y = 0$. However, as b_y is increased the fraction of the phase space covered by chaotic orbits increases, reaches a maximum for $b_y \sim b_z$, and then starts to decrease, becoming negligible for $b_y \gg b_z$, where the adiabatic approximation can be used.

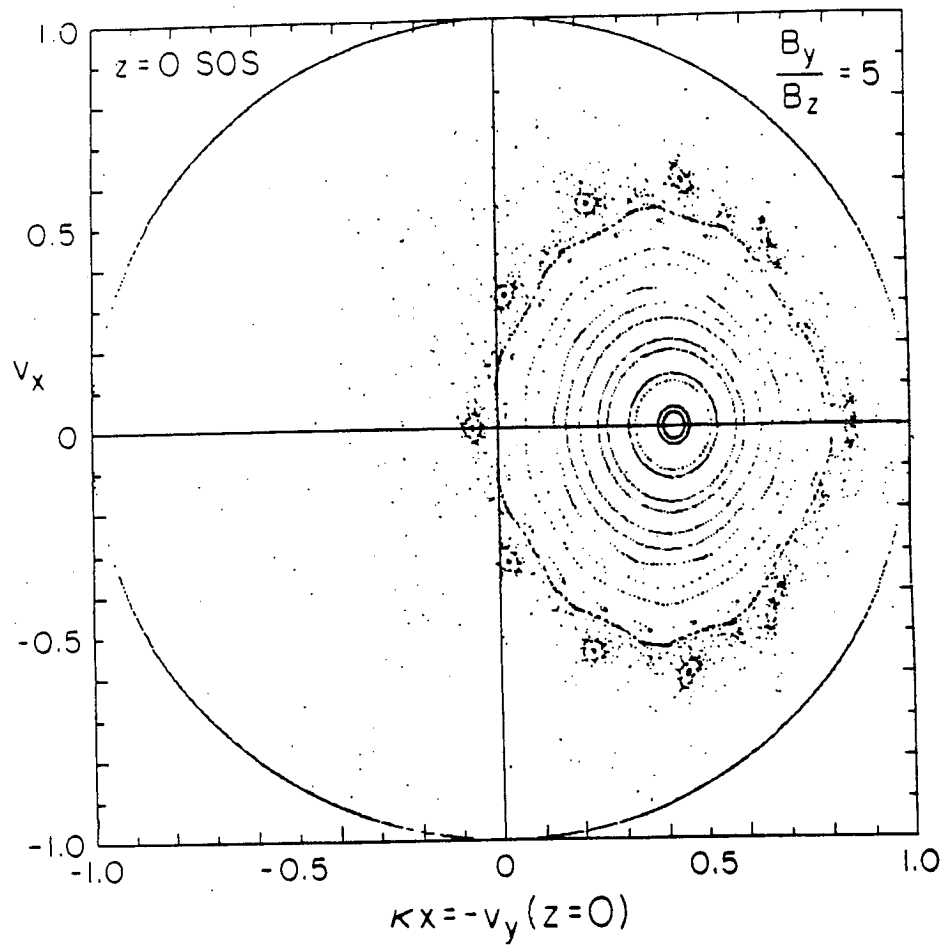


Figure 2.22: Surface of section plot for $B_y/B_z = 5$ and $\kappa = 0.18$.

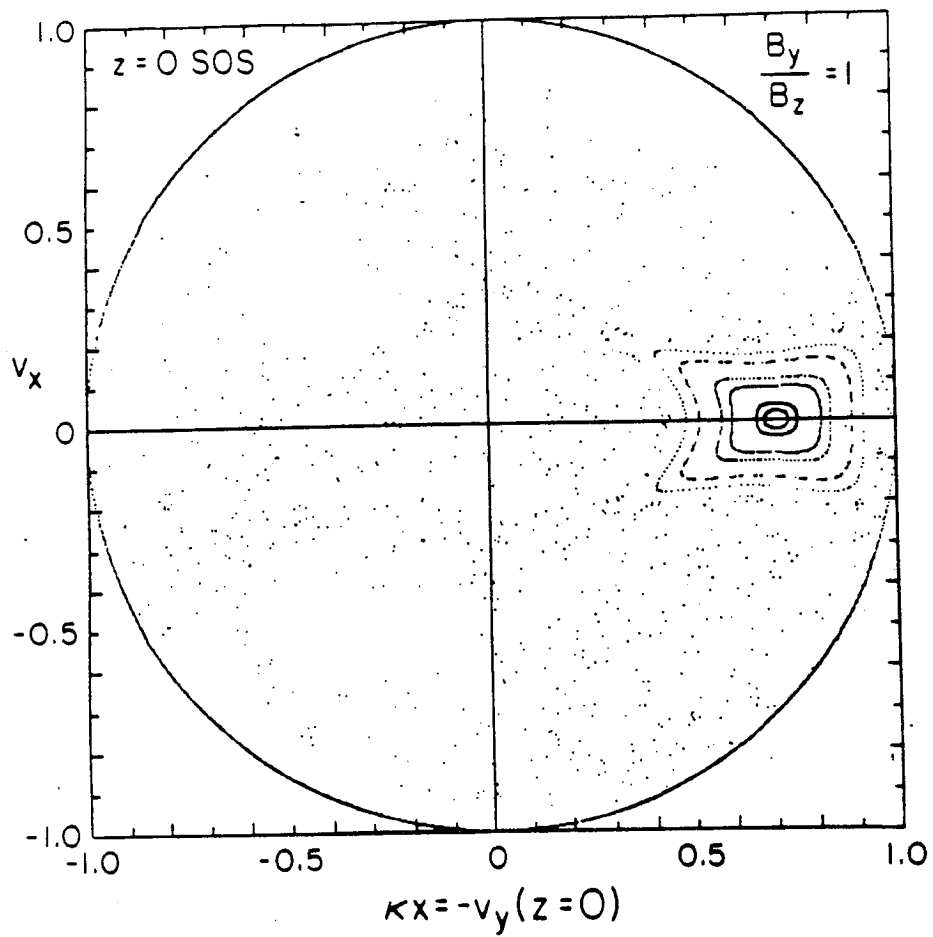


Figure 2.23: Surface of section plot for $B_y/B_z = 1$ and $\kappa = 0.18$.

Chapter 3

Chapter 3. Decay of the Correlations, Power Spectrum, and Chaotic Motion

In this chapter we introduce two quantities, the single particle two-time velocity correlation function $C(\tau)$ and the power spectrum $C(\omega)$, which are useful both for identifying chaotic motion in deterministic systems and for establishing an analogy between systems that exhibit deterministic chaos and collisional processes. The two-time velocity correlation tensor is the fundamental kernel of the statistical equilibrium transport matrix.

The correlation function $C(\tau)$ is defined as the time average of the product of two values of the velocity which are a time τ apart. On the other hand, the power spectrum $C(\omega)$, which is defined as the Fourier transform of $C(\tau)$, describes how the power in a signal is distributed over frequency.

Associated with $C(\tau)$ there is a memory, correlation, or coherence time τ_c . The correlation time should not be confused with the inverse of the Liapunov exponent λ^{-1} . Whereas the correlation time is a measure of how long it takes for a system to forget its past, the Liapunov exponent, which is the long time average rate of divergence for a bundle of neighboring trajectories in phase space, is a measure of the sensitivity of the system to its initial conditions, or to how fast the particle mixing occurs in phase space.

For collisionless motion, $C(\tau)$ and $C(\omega)$ have several properties. For integrable motion $C(\tau)$ oscillates without decay, the memory time τ_c is infinite,

and the power spectrum $C(\omega)$ consists only of discrete lines at the orbital frequencies. On the other hand, for chaotic motion, which displays an irregular and aperiodic behavior, $C(\tau)$ decays, the memory time τ_c is finite, and there is broad band noise in $C(\omega)$.

The analogy between collisional processes and chaotic motion can be established by comparison of the properties of $C(\tau)$, τ_c , and $C(\omega)$ in both cases. In the presence of collisions the correlation function decays, the correlation time corresponds to the collisional time, and the power spectrum is broad and due to the continuous mixing of orbital frequencies by the collisions.

The above analogy between chaotic motion and collisions led *Horton and Tajima* [1990] to postulate that in the collisionless environment of the geotail the finite conductivity, necessary to explain magnetic merging, is due to the decay of the velocity correlations produced by chaotic particle motion. Furthermore, for the parabolic field model and for the modified Harris sheet model, *Horton and Tajima* showed that $C(\tau)$ exhibits a power law decay $(\tau_c/\tau)^m$. This power law decay of the velocity correlations is reminiscent of the power law decay in molecular Lorentz gas scattering.

3.1 Velocity Correlations and Power Spectra for Single Particle Motion

Consider for simplicity (a general formulation will be given in the next chapter) the α -component of the velocity vector $v_\alpha(t)$. We define the single particle two-time velocity correlation function $C_{\alpha\alpha}(\tau)$ by

$$C_{\alpha\alpha}(\tau) = \overline{v_\alpha(t)v_\alpha(t-\tau)} = \lim_{T \rightarrow \infty} \int_{-T/2}^{T/2} \frac{dt}{T} v_\alpha(t)v_\alpha(t-\tau). \quad (3.1)$$

This function is also called the auto-correlation function for the time signal $v_\alpha(t)$. For a distribution of N particles that is ergodic the single particle correlation function in Eq. (3.1) is independent of the initial conditions and thus the same as the $\frac{1}{N} \sum_{i=1}^N$ ensemble averaged correlation function. In general the magnetospheric particles are not ergodic.

For non-stationary orbits due to slow variations of the equilibrium τ_{eq} or finite particle confinement time τ_{loss} , the approximation in (3.1) of a stationary correlation function $C(t, t') \approx C(t - t')$ is valid when the decay time τ_c is smaller than τ_{eq} and τ_{loss} .

Note that $C_{\alpha\alpha}(\tau = 0)$ is the mean square value of $v_\alpha(t)$. Normalizing the correlation function by its initial value,

$$\frac{C_{\alpha\alpha}(\tau)}{v_\alpha^2(t)} = \hat{C}_{\alpha\alpha}(\tau), \quad (3.2)$$

we introduce the correlation or memory time τ_c through the relation

$$\tau_c = \int_0^\infty d\tau \hat{C}_{\alpha\alpha}(\tau). \quad (3.3)$$

In this section we consider only the $\alpha\alpha$ -component of the velocity correlations and drop the $\alpha\alpha$ subscript. In the central plasma sheet of the geotail where there is a small dawn-dusk electric field, $E_y \sim 0.1$ mV/m, we are interested on the yy -component of the conductivity and take $C(\tau) \equiv C_{yy}(\tau)$.

Another useful quantity is the velocity power spectrum $\hat{C}(\omega)$, which is the Fourier transform of the velocity correlation function $\hat{C}(\tau)$,

$$\hat{C}(\omega) = \int_{-\infty}^{\infty} d\tau e^{i\omega\tau} \hat{C}(\tau). \quad (3.4)$$

It is important to note that $\hat{C}(\omega = 0)/2 = \tau_c$ because this value determines the dc conductivity, that is, the response of the magnetosphere to a constant uniform electric field E_y .

Fig. 3.1 is a plot, using the dimensionless variables of Eq. (2.58), of (a) the y -component of the velocity as a function of time $v_y(t)$, (b) the corresponding two-time velocity correlation function $\hat{C}(\tau)$, and (c) the velocity power spectrum $\hat{C}(\omega)$ for an integrable (ring) orbit in the parabolic field model of Eq. (1.34). Similarly, Fig. 3.2 is a plot of (a) $v_y(t)$, (b) $\hat{C}(\tau)$, and (c) $\hat{C}(\omega)$ for a chaotic (cucumber) orbit. The correlation time for the ring orbit is infinite and the correlation time for the chaotic orbit is $\tau_c \approx 2.4/\omega_{bz}$.

The velocity correlation for a single proton in the dawn-dusk direction for the *Tsyganenko* [1987] magnetosphere model has been calculated by *Horton et al.* [1991] for a 1 – 15 keV proton by assigning its initial position at $(-100 R_E, 0, 0)$. The rapid fall for the first 20 sec (roughly speaking) and the following power law decay for the correlation function is similar to that shown in Fig. 3.2. The power law fit to the correlation $C(\tau) \propto \frac{1}{\tau^S}$ gives the following results:

$$S = \begin{cases} \sim 0.5 & 1 \text{ keV} \\ \sim 0.6 & 3 \text{ keV} \\ \sim 0.7 & 6 \text{ keV} \\ \sim 0.8 & 15 \text{ keV}. \end{cases}$$

More energetic particles with a larger λ have a faster decay index.

As can be observed from Figs. 3.1 and 3.2 there are several qualitative differences, in terms of $\hat{C}(\tau)$ and $\hat{C}(\omega)$, between integrable and chaotic motion. The relevant properties of $\hat{C}(\tau)$ and $\hat{C}(\omega)$ are:

- Integrable motion: $\hat{C}(\tau)$ oscillates without decay, $\tau_c \rightarrow \infty$, and $\hat{C}(\omega)$ has

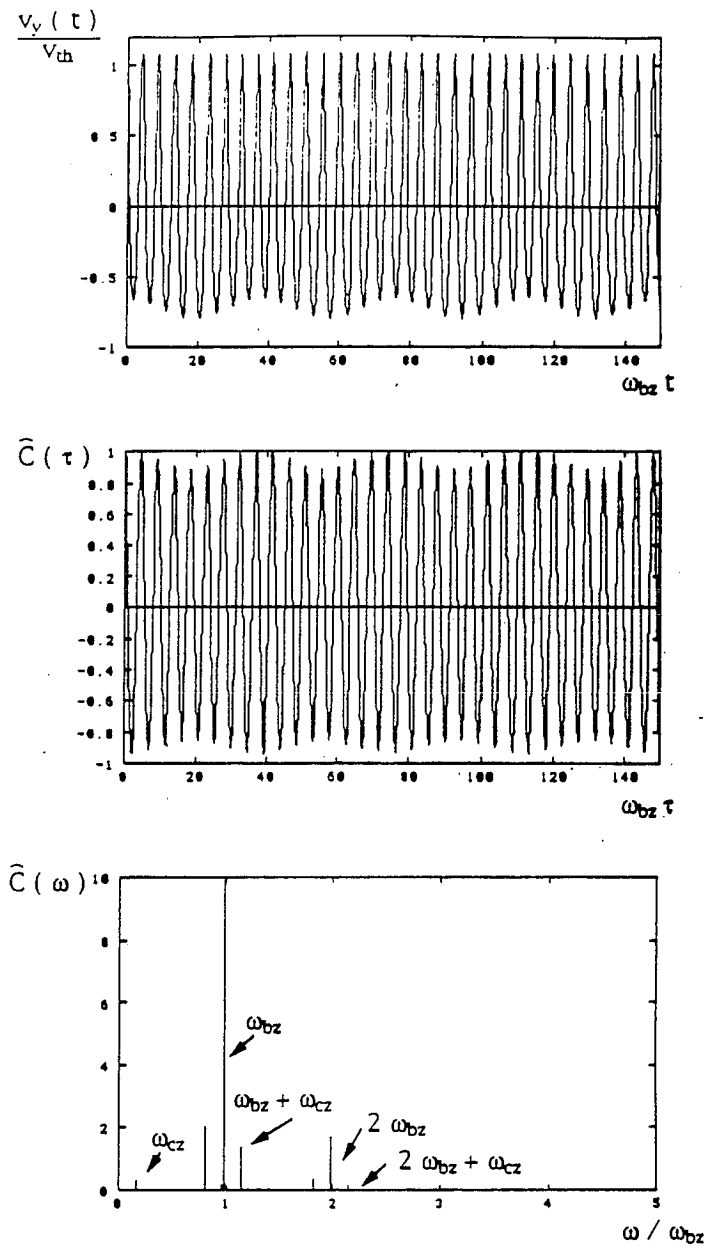


Figure 3.1: Single particle velocity correlation function and power spectrum for a ring orbit. (a) $v_y(t)$, (b) $\hat{C}(\tau)$, and (c) $\hat{C}(\omega)$.

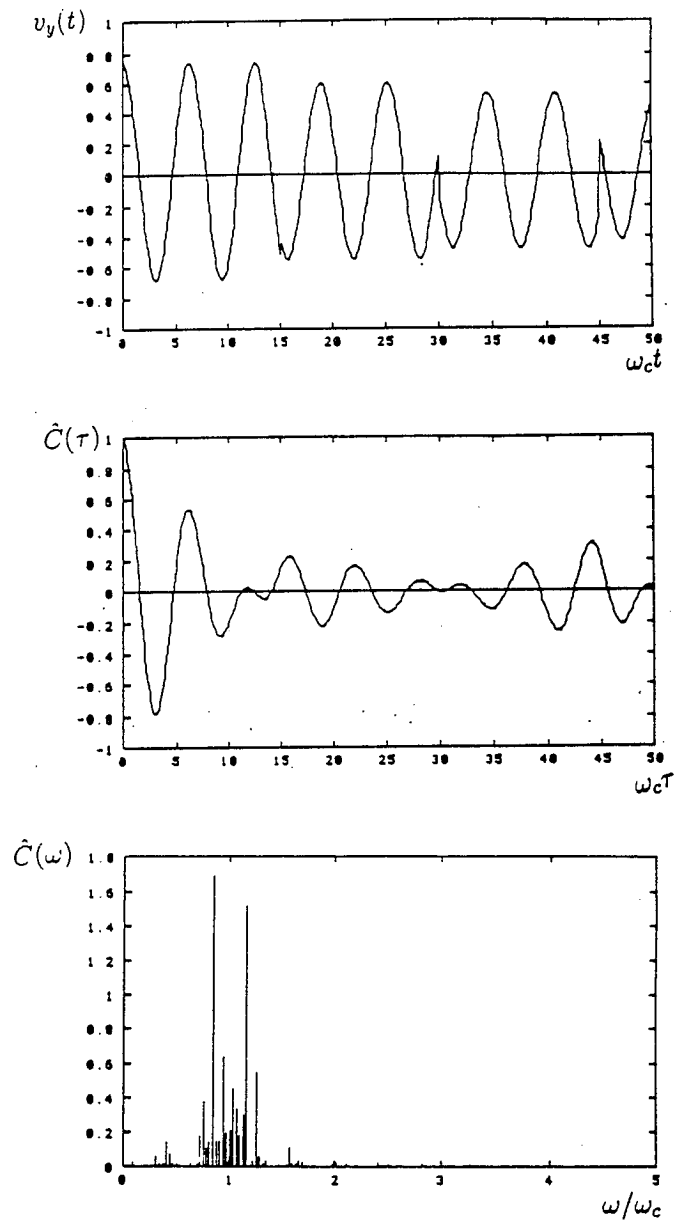


Figure 3.2: Single particle velocity correlation function and power spectrum for a cucumber orbit. (a) $v_y(t)$, (b) $\hat{C}(\tau)$, and (c) $\hat{C}(\omega)$.

spikes (δ -functions) at the orbital frequencies and their first harmonics;

- Chaotic motion: the velocity correlation function $\hat{C}(\tau)$ decays, τ_c is finite, and $\hat{C}(\omega)$ has a continuous grassy or noisy structure and there is a broad band of absorption frequencies.

The existence of a broad band spectrum for chaotic motion can be understood in the following way. In integrable systems the phase space trajectories lie on well defined invariant tori, and each torus is parametrized by the action variables \mathbf{I} with a well defined set of corresponding angular frequencies $\omega(\mathbf{I})$. However, when a perturbation is applied to the system so that motion becomes chaotic in some regions of phase space, the invariant tori are broken and there is an irregular broad band of absorption frequencies. The decay of the correlations for chaotic motion occurs due to the continuous mixing of the orbital frequencies.

3.2 Velocity Correlations and Power Spectrum in the Presence of Collisions

Let us now compare the results of the previous section for collisionless motion with the corresponding results for particle motion in the presence of collisions. In particular, consider Figs. 3.3 and 3.4.

Fig. 3.3 is a plot of (a) the projection on the y - z plane of the motion of a charged particle moving in the presence of a constant, uniform magnetic field B_z along the z -axis, (b) the yy -component of the two-time single particle velocity correlation function $\hat{C}(\tau)$, and (c) the velocity power spectrum $\hat{C}(\omega)$. Fig. 3.3 was generated by the integration of the equations of motion with the

Lorentz force,

$$\begin{aligned}\dot{v}_x &= \omega_c v_y, \\ \dot{v}_y &= -\omega_c v_x, \\ \dot{v}_z &= 0,\end{aligned}\tag{3.5}$$

where $\omega_c = qB_z/m$. As expected for integrable motion, the correlation function oscillates without decay and the power spectrum has a sharp spike at $\omega = \omega_c$.

The results for charged particle motion in a uniform, constant B_z in the presence of small-angle, energy conserving kicks are shown in Fig. 3.4. Fig. 3.4 was generated by the integration of the equations of motion (3.5) and changing the poloidal and azimuthal angles of the velocity vector by a small quantity,

$$\begin{aligned}\theta &\rightarrow \theta + \Delta\theta, \\ \phi &\rightarrow \phi + \Delta\phi,\end{aligned}\tag{3.6}$$

every time step $\Delta t = 15/\omega_c$. The increments in the angles are chosen from a uniform random distribution $-2\pi/360 \leq \Delta\theta, \Delta\phi \leq 2\pi/360$. As observed from Fig. 3.4, $\hat{C}(\tau)$ decays and $\hat{C}(\omega)$ has a broad band structure due to the collisions, and the collisional time is given by the correlation time of Eq. (3.3).

Comparing Figs. 3.1 and 3.2 with Figs. 3.3 and 3.4 we find that chaotic particle motion is similar to a collisional process, with the effective collisional time given by the characteristic velocity decorrelation time of Eq. (3.3).

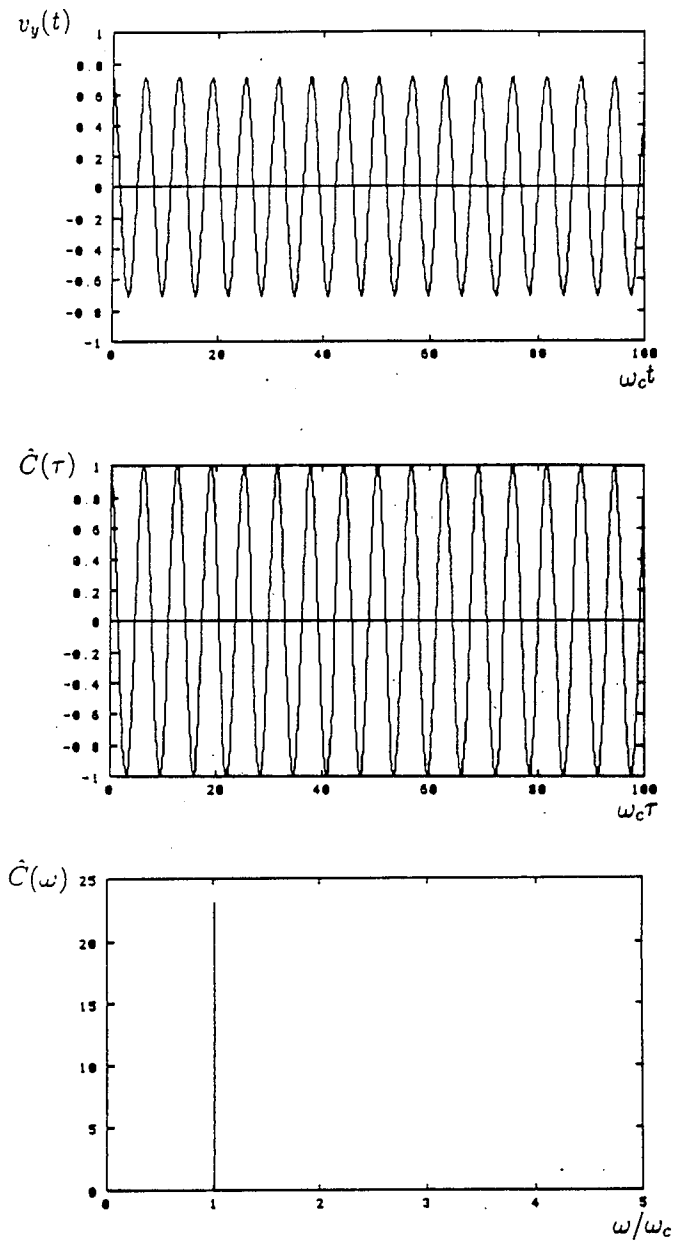


Figure 3.3: Velocity auto-correlation function and power spectrum for a particle executing cyclotron motion.

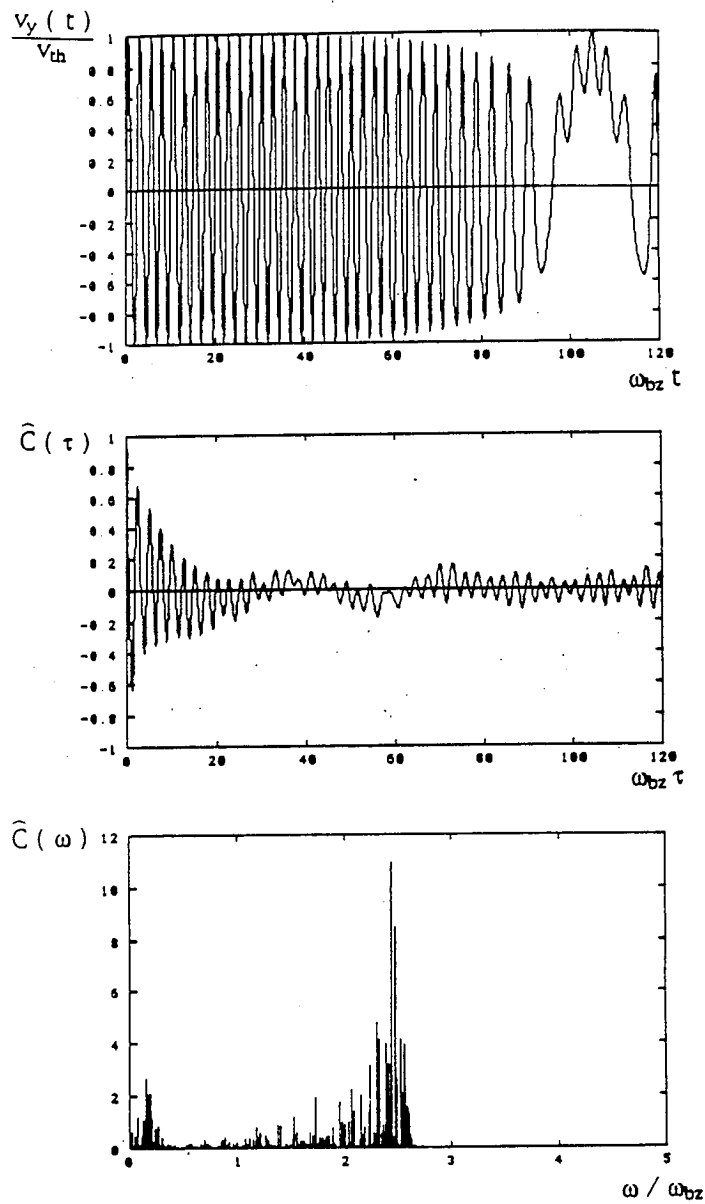


Figure 3.4: Velocity auto-correlation function and power spectrum in the presence of collisions.

3.3 Decay of the Correlations and the Collisionless Conductivity in the Geomagnetic Tail

The idea that the decay of the velocity correlations due to chaotic particle motion is similar to the decay of the velocity correlations due to collisions has been used by *Horton and Tajima* [1990, 1991] to explain the collisionless conductivity in the geomagnetic tail.

The electrical conductivity σ depends on the coherence time τ_c for acceleration of a particle by the electric field,

$$\sigma = \frac{nq^2}{m} \tau_c. \quad (3.7)$$

In kinetic theory τ_c is determined by the decay of the two-time velocity correlation function for the particle. In the presence of collisions this decay time is simply the mean time between collisions. In the presence of a turbulent spectrum of waves the decay time τ_c is the scattering time of the particle's momentum by the waves.

For integrable orbits and in the absence of waves or collisions, $\hat{C}(\tau)$ oscillates without decay showing the reversible and long-time memory of the particles. For chaotic motion the momentum of the particles is scattered by the Lorentz force, $\Delta \mathbf{p} = q \mathbf{v} \times \mathbf{B}(\mathbf{x}) \Delta t$, and $\hat{C}(\tau)$ decays showing that the particles have a finite memory just as in the case of collisions.

The procedure of *Horton and Tajima* [1990] for calculating the collisionless conductivity is: calculate the orbits of the particles and their single particle velocity correlations, and then average over ensembles of particles to obtain the proper weighting factors from the various kinds of orbits, that is,

with the effective correlation time given by

$$\tau_c = \left\langle \int_0^\infty d\tau \hat{C}(\tau) \right\rangle = \frac{1}{2} \langle \hat{C}(\omega = 0) \rangle. \quad (3.8)$$

Fig. 3.5 is a plot of $\langle \ln \hat{C}(\tau) \rangle$ as a function of $\ln(\omega_{bz}\tau)$, obtained for the sheared parabolic field model of Eq. (2.126) for a case with a net dawn-dusk magnetic field component. In Fig. 3.5 $\hat{C}(\tau)$ is normalized in such a way as to have $\hat{C}(\tau = 0) = 1$, no electric field E_y is actually present in the orbit calculation, and the parameters of the simulation are $\kappa = 0.18$, $b_y/b_z = 2$, $b_z = 0.05$, and $N = 1000$. The plots were generated by launching a Maxwellian distribution at $y = z = 0$. We observe that, as in the case with no cross-tail magnetic field, the ensemble-averaged correlation function behaves according to a power law with several decay indices m_ℓ with $0 < m_\ell \leq 1$,

$$\langle \hat{C}(\tau) \rangle = \sum_\ell \frac{c_\ell(\omega_\ell \tau)}{1 + \left(\frac{\tau}{\tau_\ell}\right)^{m_\ell}}; \ell = 1, 2, \dots, \quad (3.9)$$

where $c_\ell(\tau)$ are periodic or quasiperiodic functions of the orbital frequencies and strength such that $\sum_\ell c_\ell(0) = 1$ and the term with the smallest decay index, $m_{min} \approx 0.5$, dominates for large τ . Analytic expressions for the conductivity based on the power law decay of $\langle C(\tau) \rangle$ are given in *Horton and Tajima* [1991a,b].

Fig. 3.6 is a plot of the ensemble averaged power spectrum, $\langle \hat{C}(\omega) \rangle$, as a function of ω/ω_{bz} , with the same simulation parameters as in Fig. 3.5. In this plot there is a spike at $\omega/\omega_{bz} = \kappa$, which corresponds to the resonance from the cyclotron motion about the B_z component ($\omega = \omega_{cz} = qB_z/m$). The area below the power spectrum curve was obtained by using a composite Simpson's rule integration algorithm. The value obtained, 1.58, from the summation is in

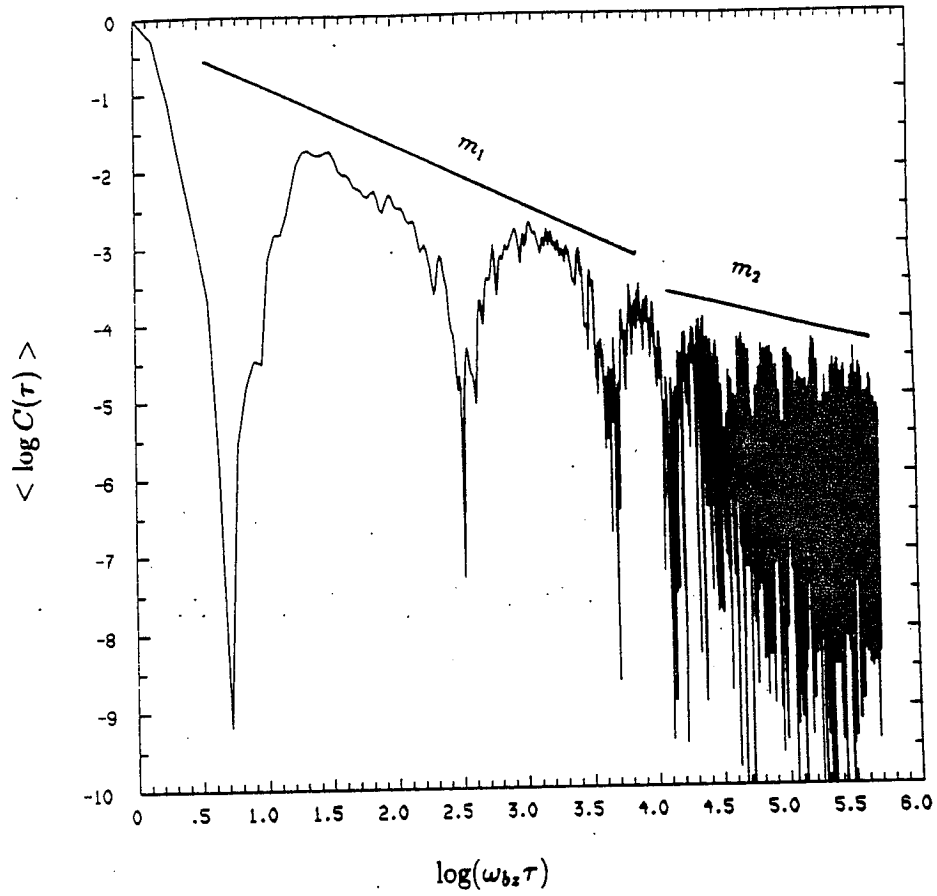


Figure 3.5: Plot of $\langle \ln \hat{C}(\tau) \rangle$ as a function of $\ln(\omega_{b_z} \tau)$. The parameters for the simulation are $\kappa = 0.18$, $b_y = 0.1$, and $b_z = 0.05$. The power-law decay of the velocity correlations is indicated by the straight lines. The slopes of these lines are the decay indices m_ℓ .

good agreement with the $\pi/2$ value required by the frequency sum rule (4.102). We obtained the power spectrum by first taking the Fourier transform of $v_y(t)$, then using the relation

$$\hat{C}(\omega) = \frac{\omega_{min}}{2\pi} |v_y(\omega)|^2, \quad (3.10)$$

which can be derived from the definition of the correlation function (3.1), from (3.4), and averaging the result of (3.10) over all the particles. In Eq. (3.10) the minimum frequency, ω_{min} , is defined by $\omega_{min} \equiv 2\pi/T$, where T is the total integration time ($T = 1200\omega_{bz}^{-1}$ in Figs. 3.5 and 3.6), and $\hat{C}(\omega)$ is evaluated at multiples of the minimum frequency $\omega_k = k\omega_{min}$ ($k = 0, 1, 2, \dots$). For the reference parameters $b_z = 0.05$ and $\kappa = 0.18$, the period T is approximately 40 min and $\omega_{min}/2\pi = 0.5$ mHz.

The power law decay of the velocity correlations is similar to that of the molecular gas scattering problem [Alder and Wainright, 1970; Dorfman and Cohen, 1970; and Ernst and Weyland, 1971] and is the primary justification for thinking of the chaotic particle dynamics as producing a collisionless momentum scattering. For scattering on fixed, recoilless scatters, the decay of the velocity correlations is given by $C^{LG}(\tau) = (\tau_c/\tau)^{(1+d/2)}$, where $d = 2$ or 3 for the two or three -dimensional system, respectively.

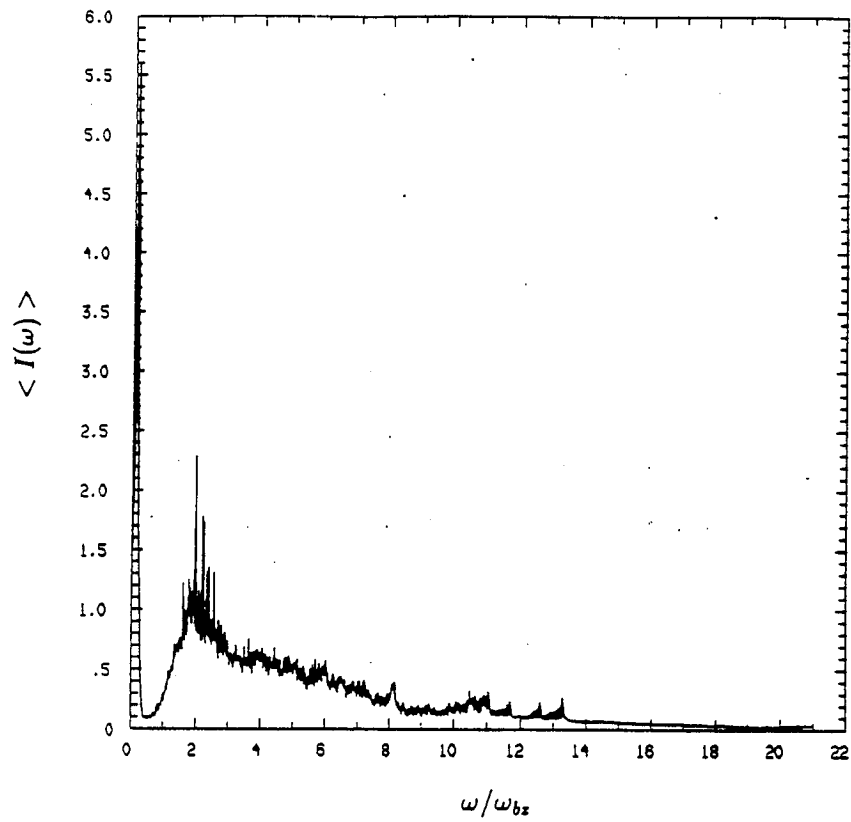


Figure 3.6: Plot of $\langle \hat{C}_{yy}(\omega; \mathbf{X}_0) \rangle$ as a function ω/ω_{bz} .

Chapter 4

Chapter 4. Collisionless Conductivity

Magnetospheric substorms are triggered by magnetic reconnection events in the dayside magnetopause and in the central plasma sheet of the geomagnetic tail. In order to have the diffusion of the magnetic field lines necessary for the instability, some kind of resistivity η is needed. In particular, taking the curl of Ohm's law with a scalar conductivity σ ($\eta = 1/\sigma$),

$$\mathbf{J} = \sigma(\mathbf{E} + \mathbf{U} \times \mathbf{B}), \quad (4.1)$$

the evolution of the magnetic field \mathbf{B} in a medium of conductivity σ is given by

$$\frac{\partial \mathbf{B}}{\partial t} = \nabla \times (\mathbf{U} \times \mathbf{B}) + \frac{1}{\mu_0 \sigma} \nabla^2 \mathbf{B}. \quad (4.2)$$

The first term of this equation gives the frozen-in convection of the magnetic field by the medium and the second term describes the effects of diffusion. Only the diffusion term allows for a change of the fields required for reconnection of magnetic field lines.

Let τ represent the characteristic time for magnetic field changes, τ_R be the characteristic resistive diffusion time, τ_A be the characteristic transport time, and L be the characteristic spatial length of \mathbf{B} . Then, Eq. (4.2) can be symbolically written as

$$\frac{1}{\tau} = \frac{1}{\tau_A} + \frac{1}{\tau_R}, \quad (4.3)$$

where

$$\tau_A = \frac{L}{U} \quad (4.4)$$

and

$$\tau_R = \mu_0 \sigma L^2. \quad (4.5)$$

The magnetic Reynolds number R_m is a measure of the importance of the diffusion term relative to the transport term,

$$R_m \equiv \frac{\tau_R}{\tau_A} = \mu_0 \sigma U L. \quad (4.6)$$

The diffusion term in (4.2) can be ignored if

$$R_m \gg 1. \quad (4.7)$$

The simplest example of spontaneous reconnection is the tearing instability of a plane current sheet. The plane current sheet can be viewed as being formed by a set of parallel current filaments. Because of the Lorentz force, the parallel current filaments attract each other and the configuration is unstable against the pinching of current filaments. This instability is called the tearing mode instability.

The growth rate γ of tearing modes in a plane current sheet layer is given by [Furth *et al.*, 1963]

$$\gamma \sim \tau_A^{-2/5} \tau_R^{-3/5} = \tau_A^{-1} R_m^{-3/5}. \quad (4.8)$$

The hybrid time scale of $\tau_A^{2/5}$ and $\tau_R^{3/5}$ arises from dynamics in Eq. (4.2) that is localized in a boundary layer of width $\Delta z/L_z = (\tau_R/\tau_A)^{3/10}$. In this boundary layer the resistive decay of the magnetic field energy is converted into flow $\frac{1}{2}\rho U^2$ and thermal energy.

In the mid-tail the lobe magnetic field is $B_{x0} \approx 20$ nT and the proton density is $n_0 \approx 10^6$ m⁻³. The Alfvén velocity $v_A(z)$ for the Harris sheet model is

$$v_A(z) = \frac{B_{x0}}{\sqrt{\mu_0 m_i n_0}} \left| \sinh \left(\frac{z}{L_z} \right) \right|. \quad (4.9)$$

Averaging $v_A(z)$ in the field reversal region we obtain

$$v_A = \int_0^{L_z} \frac{dz}{L_z} v_A(z) \approx \frac{1}{2} \frac{B_{x0}}{\sqrt{\mu_0 m_i n_0}} = 200 \text{ km/s} \quad (4.10)$$

and, given that the characteristic spatial length of the current sheet is $L_z \sim 1 R_E$, the Alfvén time is

$$\tau_A = \frac{L_z}{v_A} = 30 \text{ s}. \quad (4.11)$$

Typical growth rates of geomagnetic activity during the onset phase of a magnetospheric substorm are of the order of $\gamma \sim 0.2 \text{ min}^{-1}$, which, according to (4.8), corresponds to $R_m = 200$ and to $\sigma = 6 \times 10^{-5}$ mho/m. Note however that if electrons carry the current then

$$\sigma = \frac{nq^2}{m_e} \tau_c, \quad (4.12)$$

where τ_c is the collisional time. For $R_m = 200$ the collisional time is $\tau_c = 2 \times 10^{-3}$ s compared with $2\pi/\omega_{ce} = 1.6 \times 10^{-3}$ s. If ions carry the current, then the collisional time is $\tau_c = 4$ s compared with $2\pi/\omega_{ci} = 3$ s. On the other hand, for $T_e = 0.1$ keV, the *Spitzer* [1962] conductivity is $\sigma = 1 \times 10^6$ mho/m which corresponds to a collisional time $\tau_c \sim 1$ year and thus a collisionless resistivity is required. For the Spitzer conductivity $R_m^{Sp} = 2 \times 10^{12}$.

Currently there are two approaches to account for the collisionless resistivity. One approach assumes that the momentum of the particles is scattered by turbulent plasma waves. However, *Anderson* [1984] found, through

satellite crossings of the current sheet, that turbulent wave activity is negligible at the center of the current sheet. A second approach is to assume that the collisionless conductivity is due to charged particle dynamics in the current sheet. Examples of this approach are the *Lyons-Speiser* [1985] conductivity σ^{L-S} due to particle inertia and the *Horton-Tajima* [1990, 1991a, b] conductivity σ^{H-T} based on the decay of the velocity correlations due to chaotic particle motion of the ions.

The Horton-Tajima conductivity formula is

$$\sigma^{H-T} = \frac{nq^2}{m_i} \frac{\epsilon^{1/2}}{c_1 |\omega_{cz}|}, \quad (4.13)$$

where $c_1 \approx 10$ is a constant determined by simulations, ω_{cz} is the cyclotron frequency of the ions for the component of the magnetic field normal to the current sheet (B_z) and $\epsilon = \rho/L$ is the finite Larmor radius parameter for the ions. Ion temperatures in the central plasma sheet are in the range $T_i = 1 - 5 \text{ keV}$. For $T_i = 1 \text{ keV}$ the conductivity is $\sigma^{H-T} = 1 \times 10^{-5} \text{ mho/m}$ which corresponds to $R_m = 330$. The Horton-Tajima conductivity is valid for vanishing B_y . In the $B_y = 0$ case the electrons are tied to the magnetic field lines and cannot move across them in the y -direction in response to the E_y field. When $B_y \neq 0$, as considered in the next chapter, the electrons can move along y and start playing an important role [*Hernández et al.*, 1993].

In Section 4.1 we introduce the dielectric tensor, the conductivity tensor, the dielectric response function, and the Kramers-Kronig relations. The topics covered in Section 4.1 are standard textbook material [*Ichimaru*, 1991; *Landau and Lifshitz*, 1960; *Stix*, 1992] and are included here to make the present dissertation self-contained. In Section 4.2 we derive the spectral velocity cor-

relations (SVC) formalism. The SVC formalism, which is used for the calculation of the collisionless conductivity, is the central result of the present chapter. Finally, we discuss the relationship between the SVC formalism and the fluctuation-dissipation theorem.

4.1 The Dielectric Tensor

In the study of macroscopic media it is convenient to use both the displacement vector \mathbf{D} and the electric field \mathbf{E} , which are related through

$$\mathbf{D} = \epsilon_0 \mathbf{E} + \mathbf{P}, \quad (4.14)$$

with the polarization vector \mathbf{P} satisfying

$$\nabla \cdot \mathbf{P} = -\rho_p \quad \text{and} \quad \frac{\partial \mathbf{P}}{\partial t} = \mathbf{J}_p, \quad (4.15)$$

which are consistent with the continuity equation

$$\frac{\partial \rho_p}{\partial t} + \nabla \cdot \mathbf{J}_p = 0. \quad (4.16)$$

The most general causal linear relationship between \mathbf{D} and \mathbf{E} is given by

$$\mathbf{D}(\mathbf{r}, t) = \epsilon_0 \mathbf{E}(\mathbf{r}, t) + \epsilon_0 \int_{-\infty}^t dt' \int d^3 r' \mathbf{K}(\mathbf{r}, \mathbf{r}', t, t') \cdot \mathbf{E}(\mathbf{r}', t'), \quad (4.17)$$

where the domain $(-\infty, t)$ of the t' integration reflects the causal relation between \mathbf{E} and \mathbf{D} . The linear relation of Eq. (4.17) is nonlocal in both space and time. This nonlocality arises from the fact that the motion of particles in collisionless plasmas depends on the field values along their trajectories. For a stationary plasma the 3×3 matrix kernel \mathbf{K} depends on t and t' through the

time difference $\tau \equiv t - t'$. Furthermore, if the plasma is homogeneous, then \mathbf{K} becomes a function of $\boldsymbol{\rho} \equiv \mathbf{r} - \mathbf{r}'$ and (4.17) can be written as

$$\mathbf{D}(\mathbf{r}, t) = \epsilon_0 \mathbf{E}(\mathbf{r}, t) + \epsilon_0 \int_0^\infty d\tau \int d^3\rho \mathbf{K}(\boldsymbol{\rho}, \tau) \cdot \mathbf{E}(\mathbf{r} - \boldsymbol{\rho}, t - \tau). \quad (4.18)$$

Expanding Eq. (4.18) in terms of plane waves we get

$$\mathbf{D}(\mathbf{k}, \omega) = \epsilon(\mathbf{k}, \omega) \cdot \mathbf{E}(\mathbf{k}, \omega), \quad (4.19)$$

where the dielectric tensor ϵ is

$$\epsilon(\mathbf{k}, \omega) = \epsilon_0 \mathbf{I} + \int_0^\infty d\tau \int d^3\rho \mathbf{K}(\boldsymbol{\rho}, \tau) e^{-i(\mathbf{k} \cdot \boldsymbol{\rho} - \omega\tau)}. \quad (4.20)$$

The dependence of the dielectric tensor on the wave vector and on the frequency is referred to as spatio-temporal dispersion. Dispersion is a consequence of the nonlocality of the relation between \mathbf{E} and \mathbf{D} .

From the reality of the fields $\mathbf{E}(\mathbf{r}, t)$ and $\mathbf{D}(\mathbf{r}, t)$ it follows that

$$\epsilon^*(\mathbf{k}, \omega) = \epsilon(-\mathbf{k}, -\omega). \quad (4.21)$$

Denoting the real and imaginary parts of ϵ by ϵ' and by ϵ'' , (4.21) can be written as

$$\epsilon'(\mathbf{k}, \omega) = \epsilon'(-\mathbf{k}, -\omega), \quad \epsilon''(\mathbf{k}, \omega) = -\epsilon''(-\mathbf{k}, -\omega). \quad (4.22)$$

Similar linear response equations to that in Eq. (4.17) give the causal relationship between $\mathbf{J}(\mathbf{r}, t)$ and $\mathbf{E}(\mathbf{r}, t)$, which defines the conductivity tensor. The conductivity tensor is a functional of the distribution of the particle orbits, as will be considered in the next section. In the linear approximation, \mathbf{J} is given in terms of \mathbf{E} through the conductivity tensor $\boldsymbol{\sigma}$,

$$\mathbf{J}(\mathbf{k}, \omega) = \boldsymbol{\sigma}(\mathbf{k}, \omega) \cdot \mathbf{E}(\mathbf{k}, \omega), \quad (4.23)$$

From (4.14), (4.15), and (4.19) we find that the dielectric tensor is related to the conductivity tensor by

$$\epsilon(\mathbf{k}, \omega) = \epsilon_0 \mathbf{I} - \frac{\boldsymbol{\sigma}(\mathbf{k}, \omega)}{i\omega}, \quad (4.24)$$

where \mathbf{I} is the identity tensor.

4.1.1 Longitudinal Response Function

When an external electrostatic perturbation,

$$\delta\phi_{ext}(\mathbf{r}, t) = \delta\phi_{ext}(\mathbf{k}, \omega) e^{i(\mathbf{k}\cdot\mathbf{r} - \omega t)}, \quad (4.25)$$

is applied to a uniform plasma, it induces density fluctuations which translate into an induced potential $\delta\phi$. In the linear approximation, the induced potential is related to the external potential through

$$\delta\phi(\mathbf{k}, \omega) = \left[\frac{\epsilon_0}{\epsilon(\mathbf{k}, \omega)} - 1 \right] \delta\phi_{ext}(\mathbf{k}, \omega), \quad (4.26)$$

where $\epsilon(\mathbf{k}, \omega)$ is the dielectric response function. To give a physical interpretation to $\epsilon(\mathbf{k}, \omega)$ consider the total potential $\delta\phi_t$ in a uniform plasma:

$$\delta\phi_t = \delta\phi_{ext} + \delta\phi. \quad (4.27)$$

Substituting (4.26) into (4.27) we find that the external potential is screened by the dielectric factor $\epsilon_0/\epsilon(\mathbf{k}, \omega)$ in the medium:

$$\delta\phi_t(\mathbf{k}, \omega) = \frac{\epsilon_0}{\epsilon(\mathbf{k}, \omega)} \delta\phi_{ext}. \quad (4.28)$$

The dielectric response is given in terms of the dielectric tensor by

$$\epsilon(\mathbf{k}, \omega) = \frac{\mathbf{k} \cdot \boldsymbol{\epsilon} \cdot \mathbf{k}}{k^2}, \quad (4.29)$$

which is obtained from the continuity equation (4.16), from (4.23), and from (4.24).

4.1.2 Energy Dissipation and Stored Energy

The mean energy Q absorbed by the medium per unit time and unit volume is

$$Q = \langle \mathbf{J} \cdot \mathbf{E} \rangle = \frac{1}{2} \text{Re} [\mathbf{J}(\mathbf{k}, \omega) \cdot \mathbf{E}^*(\mathbf{k}, \omega)], \quad (4.30)$$

where angle brackets denote a space-time average. Substituting (4.23) into (4.30) we get

$$Q = \frac{1}{2} \mathbf{E}^* \cdot \boldsymbol{\sigma}^H \cdot \mathbf{E}, \quad (4.31)$$

where $\boldsymbol{\sigma}^H$ is the Hermitian part of the conductivity tensor,

$$\sigma_{\alpha\beta}^H = \frac{1}{2} (\sigma_{\alpha\beta} + \sigma_{\beta\alpha}^*). \quad (4.32)$$

Thus, dissipation in the medium is given by the Hermitian component of the conductivity tensor. The anti-Hermitian part of the conductivity tensor,

$$\sigma_{\alpha\beta}^A = \frac{1}{2} (\sigma_{\alpha\beta} - \sigma_{\beta\alpha}^*), \quad (4.33)$$

corresponds to its reactive part and contributes to the reversible or stored energy through [e.g., *Stix, 1992*]

$$\frac{1}{4\pi} \mathbf{E}^* \cdot \frac{\partial(\omega \boldsymbol{\epsilon}^H)}{\partial \omega} \cdot \mathbf{E}. \quad (4.34)$$

Expression (4.34) for the stored energy has been criticized by *Morrison* [1994] because, in a Vlasov context, it neglects the effects of resonant particles.

From (4.24) we have that the Hermitian and anti-Hermitian parts of the dielectric tensor are

$$\boldsymbol{\epsilon}^H = \epsilon_0 \mathbf{I} - \frac{\boldsymbol{\sigma}^A}{i\omega} \quad (4.35)$$

and

$$\boldsymbol{\epsilon}^A = -\frac{\boldsymbol{\sigma}^H}{i\omega}. \quad (4.36)$$

In a medium with no dissipation the dielectric tensor is Hermitian and the conductivity tensor is anti-Hermitian ($\sigma^H = 0$).

The dielectric tensor $\epsilon(\mathbf{k}, \omega)$ is transformed with a one-sided Fourier transform

$$\epsilon(\mathbf{k}, \omega) = \epsilon_0 \mathbf{I} + \epsilon_0 \int_0^\infty d\tau \mathbf{K}(\mathbf{k}, \tau) e^{i\omega\tau}, \quad (4.37)$$

which is a consequence of the causality imposed on (4.17). Regarding ω as a complex variable ($\omega = \omega_r + i\omega_i$), the integration in (4.37) converges only if $\omega_i > 0$. It follows that $\epsilon(\mathbf{k}, \omega)$ is analytic in the upper half of the complex ω -plane and is continued analytically into the lower half of the ω -plane, where it generally has singularities.

The second term in (4.37) is responsible for the establishment of the electric polarization. The tensor $\mathbf{K}(\mathbf{k}, \tau)$ is finite for all τ and $\mathbf{K}(\mathbf{k}, \tau) \rightarrow 0$ as $\tau \rightarrow \infty$. This is to insure that $\mathbf{D}(t)$ is not affected by values of $\mathbf{E}(t)$ in the infinitely remote past. In a plasma or in metals with a dc conductivity, we have $\mathbf{K}(\tau) - \sigma^{dc}/\epsilon_0 \rightarrow 0$ when $\tau \rightarrow \infty$, and $\epsilon(\mathbf{k}, \omega)$ has a pole at $\omega = 0$. When $\omega \rightarrow \infty$ in the upper half of the ω -plane, the integral in (4.37) vanishes and $\epsilon(\mathbf{k}, \infty) = \epsilon_0 \mathbf{I}$.

Consider the integral

$$\int_C \frac{\epsilon(\mathbf{k}, \omega') - \epsilon_0 \mathbf{I}}{\omega' - \omega} d\omega', \quad (4.38)$$

where ω is some real value and the contour C is shown in Fig. 4.1. Since $\epsilon(\mathbf{k}, \omega')$ is analytic in the upper half-plane and since the points $\omega' = 0$ and $\omega' = \omega$ have been excluded from the integration region, the integrand in (4.38) is analytic everywhere inside the contour C and the integral (4.38) is therefore zero.

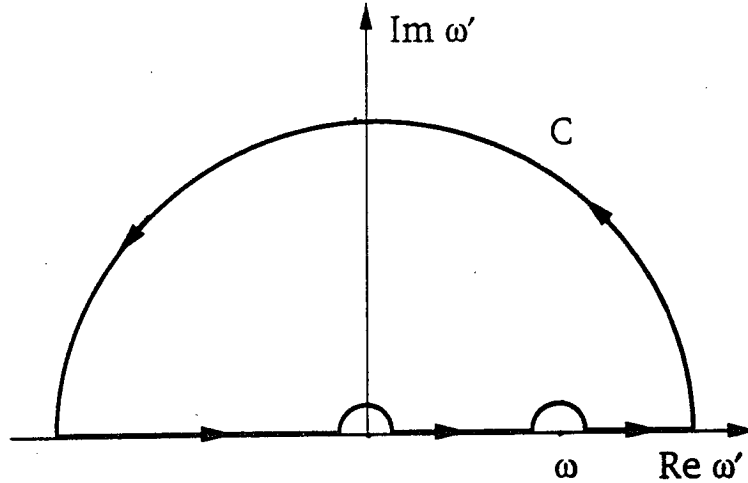


Figure 4.1: Integration Contour for (4.38). The finite semicircle at $\omega = 0$ has been included to account for the case in which the conductivity has a dc component as occurs in metals and in plasmas.

The contribution to the integral from the semicircle at infinity is zero, the contribution from the finite semicircle centered at $\omega' = 0$ is $-\pi\sigma^{dc}/\omega$, and the contribution from the semicircle around ω is $-i\pi[\epsilon(\mathbf{k}, \omega) - \epsilon_0\mathbf{I}]$. Then

$$\epsilon(\mathbf{k}, \omega) = \epsilon_0\mathbf{I} + i\frac{\sigma^{dc}}{\omega} - \frac{i}{\pi}\mathcal{P}\int_{-\infty}^{\infty} \frac{\epsilon(\mathbf{k}, \omega') - \epsilon_0\mathbf{I}}{\omega' - \omega} d\omega'. \quad (4.39)$$

Separating the dielectric tensor into its real and imaginary parts we get

$$\text{Re } \epsilon(\mathbf{k}, \omega) - \epsilon_0\mathbf{I} = \frac{1}{\pi}\mathcal{P}\int_{-\infty}^{\infty} \frac{\text{Im } \epsilon(\mathbf{k}, \omega')}{\omega' - \omega} d\omega', \quad (4.40)$$

$$\text{Im } \epsilon(\mathbf{k}, \omega) = \frac{\sigma^{dc}}{\omega} - \frac{1}{\pi}\mathcal{P}\int_{-\infty}^{\infty} \frac{\text{Re } \epsilon(\mathbf{k}, \omega') - \epsilon_0\mathbf{I}}{\omega' - \omega} d\omega'. \quad (4.41)$$

Similar relations hold between the Hermitian and anti-Hermitian parts of the dielectric tensor.

Relations such as (4.41) are known as Kramers-Kronig relations or dispersion relations. The only important property of $\epsilon(\mathbf{k}, \omega)$ used in the derivation

of the dispersion relations is that $\epsilon(\mathbf{k}, \omega)$ is analytic in the upper half-plane. Hence the Kramers-Kronig relations are a direct consequence of the causality principle.

4.2 Collisionless Conductivity in Magnetic Field Reversals

The rate of conversion of electromagnetic energy into mechanical or thermal energy is given by

$$\int d^3x \mathbf{J} \cdot \mathbf{E}, \quad (4.42)$$

which is the total power transferred by the fields to the sources in a finite volume.

Energy conservation for a system of sources and fields in a finite volume is given by Poynting's theorem,

$$\int d^3x \frac{\partial u}{\partial t} + \oint d\mathbf{a} \cdot \mathbf{S} = - \int d^3x \mathbf{J} \cdot \mathbf{E}, \quad (4.43)$$

where u is the energy density of the electromagnetic field,

$$u = \frac{\epsilon_0 E^2}{2} + \frac{B^2}{2\mu_0}, \quad (4.44)$$

and \mathbf{S} , the Poynting vector, represents the energy flow,

$$\mathbf{S} = \frac{\mathbf{E} \times \mathbf{B}}{\mu_0}. \quad (4.45)$$

Expression (4.43) means that the total work done by the fields on the sources in a volume is balanced with the rate of change of electromagnetic energy in the volume and with radiation losses through the boundary.

For fields varying harmonically in time, $e^{-i\omega t}$, energy conservation can be written as

$$\frac{1}{2} \int d^3x \mathbf{J}_\omega^* \cdot \mathbf{E}_\omega + 2i\omega \int d^3x (u_e - u_m) + \oint d\mathbf{a} \cdot \mathbf{S}_\omega = 0, \quad (4.46)$$

where

$$u_e = \frac{\epsilon_0 |E_\omega|^2}{4}, \quad (4.47)$$

$$u_m = \frac{|B_\omega|^2}{4\mu_0}, \quad (4.48)$$

and

$$\mathbf{S}_\omega = \frac{\mathbf{E}_\omega \times \mathbf{B}_\omega^*}{2\mu_0}. \quad (4.49)$$

The complex Poynting theorem (4.46) is useful because it can be used to determine the complex input impedance, $Z = R - iX$, of a general, two-terminal, electromagnetic system [Fano *et al.*, 1960]. In particular, the conversion rate of electromagnetic energy into particle energy is

$$Q_\omega = \frac{1}{2} \text{Re} \int d^3x \mathbf{J}_\omega^* \cdot \mathbf{E}_\omega \quad (4.50)$$

and the reactive or stored energy and its alternating flow is given by the imaginary part of (4.46),

$$\frac{1}{2} \text{Im} \int d^3x \mathbf{J}_\omega^* \cdot \mathbf{E}_\omega + 2\omega \int d^3x (u_e - u_m) = 0. \quad (4.51)$$

In order to determine the dissipation (4.50) necessary for magnetic reconnection in tail-like magnetic field reversals, we consider the perturbed current density $\delta\mathbf{J}$ produced as a response of the medium to tearing-like perturbations of the form

$$\delta\mathbf{A}(x, z, t) = \delta\mathbf{A}(z)e^{i(kx - \omega t)} + c.c., \quad (4.52)$$

$$\delta\phi(x, z, t) = \delta\phi(z)e^{i(kx - \omega t)} + c.c.. \quad (4.53)$$

In the linear approximation, the perturbed distribution function f_j for particle species j can be written as

$$f_j = f_{0j} + \delta f_j, \quad (4.54)$$

where the equilibrium distribution satisfies

$$\mathbf{v} \cdot \frac{\partial f_{0j}}{\partial \mathbf{r}} + \frac{q_j}{m_j} (\mathbf{v} \times \mathbf{B}) \cdot \frac{\partial f_{0j}}{\partial \mathbf{v}} = 0, \quad (4.55)$$

and where the perturbed part of the distribution function satisfies the linearized Vlasov equation

$$\frac{\partial \delta f_j}{\partial t} + \mathbf{v} \cdot \frac{\partial \delta f_j}{\partial \mathbf{r}} + \frac{q_j}{m_j} (\mathbf{v} \times \mathbf{B}) \cdot \frac{\partial \delta f_j}{\partial \mathbf{v}} = -\frac{q_j}{m_j} [\delta \mathbf{E} + \mathbf{v} \times \delta \mathbf{B}] \cdot \frac{\partial f_{0j}}{\partial \mathbf{v}}. \quad (4.56)$$

The formal solution to (4.56) is

$$\delta f_j(x, z, \mathbf{v}, t) = -\frac{q_j}{m_j} \int_{-\infty}^t dt' [\delta \mathbf{E}' + \mathbf{v}' \times \delta \mathbf{B}'] \cdot \frac{\partial f'_{0j}}{\partial \mathbf{v}'}, \quad (4.57)$$

where the integration is performed along the unperturbed trajectories $(\mathbf{x}', \mathbf{v}')$, which satisfy the initial conditions $\mathbf{x}'(t' = t) = \mathbf{x}$ and $\mathbf{v}'(t' = t) = \mathbf{v}$. The primes in the integrand of (4.57) mean that all the quantities are evaluated at time t' . Note also that the integration domain $(-\infty, t)$ is such as to satisfy the causality principle, which states that the correction δf cannot precede the perturbation $(\delta \mathbf{E}, \delta \mathbf{B})$.

The perturbed part of the current density, $\mathbf{J} = \mathbf{J}_0 + \delta \mathbf{J}$, is given by

$$\delta \mathbf{J}(x, z, t) = \sum_j q_j \int d^3 v \mathbf{v} \delta f_j, \quad (4.58)$$

which upon substitution of (4.57) into (4.58) becomes

$$\delta \mathbf{J}(x, z, t) = -\sum_j \frac{q_j^2}{m_j} \int d^3 v \mathbf{v} \int_{-\infty}^t dt' [\delta \mathbf{E}' + \mathbf{v}' \times \delta \mathbf{B}'] \cdot \frac{\partial f'_{0j}}{\partial \mathbf{v}'}. \quad (4.59)$$

The equilibrium distribution is a function of the constants of the motion $f_0 = f_0(H, P_y)$, with

$$H = \frac{1}{2} m v^2 + q \phi(x, z) \quad (4.60)$$

and

$$P_y = mv_y + qA_y(x, z). \quad (4.61)$$

Thus we have

$$\frac{\partial f_0}{\partial \mathbf{v}} = m \frac{\partial f_0}{\partial P_y} \hat{\mathbf{e}}_y + m \frac{\partial f_0}{\partial H} \mathbf{v}, \quad (4.62)$$

which for the Harris distribution,

$$f_0 = n_0 \left(\frac{m}{2\pi T} \right)^{3/2} \exp \left(-\frac{1}{T} [H - U_y P_y] \right), \quad (4.63)$$

becomes

$$\frac{\partial f_0}{\partial \mathbf{v}} = -\frac{m}{T} (\mathbf{v} - U_y \hat{\mathbf{e}}_y) f_0. \quad (4.64)$$

Substituting (4.64) into (4.59) we get

$$\delta \mathbf{J} = \sum_j \frac{q_j^2}{T_j} \int d^3 v \mathbf{v} f_{0j} \int_{-\infty}^t dt' [\delta \mathbf{E}' + \mathbf{v}' \times \delta \mathbf{B}'] \cdot (\mathbf{v}' - U_{yj} \hat{\mathbf{e}}_y), \quad (4.65)$$

where the constancy of f_{0j} along the unperturbed trajectories,

$$\left(\frac{df_{0j}}{dt} \right)_{unpert.} = 0, \quad (4.66)$$

has been used to take it out of the temporal integration.

From (4.65) we have that $\delta \mathbf{J}$ can be split into two parts,

$$\delta \mathbf{J} = \delta \mathbf{J}^{ad} + \delta \mathbf{J}^d, \quad (4.67)$$

where the adiabatic correction to the current, $\delta \mathbf{J}^{ad}$, is given by

$$\delta \mathbf{J}^{ad} = - \sum_j \frac{q_j^2 U_{yj}}{T_j} \int d^3 v \mathbf{v} f_{0j} \int_{-\infty}^t dt' [\delta \mathbf{E}' + \mathbf{v}' \times \delta \mathbf{B}'] \cdot \hat{\mathbf{e}}_y \quad (4.68)$$

and the dissipative part of the perturbed current is

$$\delta \mathbf{J}^d = \sum_j \frac{q_j^2}{T_j} \int d^3 v \mathbf{v} f_{0j} \int_{-\infty}^t dt' \mathbf{v}' \cdot \delta \mathbf{E}'. \quad (4.69)$$

First consider $\delta\mathbf{J}^{ad}$. Expanding the term enclosed by square brackets in Eq. (4.68) in terms of the perturbed potentials of Eq. (4.53), we get

$$[\delta\mathbf{E} + \mathbf{v} \times \delta\mathbf{B}] \cdot \hat{\mathbf{e}}_y = -\frac{d\delta A_y}{dt}. \quad (4.70)$$

Substituting Eq. (4.70) into Eq. (4.68), we obtain that $\delta\mathbf{J}^{ad}$ is given by

$$\delta\mathbf{J}^{ad} = \left(\sum_j \frac{q_j^2 U_{yj}}{T_j} \int d^3v \mathbf{v} f_{0j} \right) \delta A_y. \quad (4.71)$$

On the other hand,

$$\begin{aligned} \frac{\partial J_{0y}}{\partial A_y} &= \sum_j q_j \int d^3v v_y \frac{\partial f_{0j}}{\partial A_{0y}} \\ &= \sum_j \frac{q_j^2 U_{yj}}{T_j} \int d^3v v_y f_{0j}. \end{aligned} \quad (4.72)$$

Substituting (4.72) into (4.71) we get

$$\begin{aligned} \delta\mathbf{J}^{ad}(x, z, t) &= \frac{\partial J_{0y}}{\partial A_y} \delta A_y \hat{\mathbf{e}}_y \\ &= -\frac{1}{\mu_0 B_x(z)} \frac{d^2 B_x(z)}{dz^2} \delta A_y \hat{\mathbf{e}}_y. \end{aligned} \quad (4.73)$$

If in the Harris distribution of Eq. (4.63) we include both the unperturbed and perturbed parts of the vector potential in the expression for the canonical momentum of Eq. (4.61) and expand the resulting expression, then

$$\delta f_j^{ad} = \frac{q_j U_{yj}}{T_j} f_{0j} \delta A_y. \quad (4.74)$$

Multiplying Eq. (4.74) by $q_j \mathbf{v}$, integrating over the velocities, and summing over the species we recover Eq. (4.71). This is the reason for referring to $\delta\mathbf{J}^{ad}$ as the adiabatic part of the perturbed current density.

The power associated with $\delta\mathbf{J}^{ad}$ is given by

$$Q^{ad}(k, \omega) = \frac{1}{2} \int d^3x \delta\mathbf{J}_{k, \omega}^{ad} \cdot \delta\mathbf{E}_{k, \omega}^* = i \frac{\omega}{2} \int d^3x \frac{\partial J_{0y}}{\partial A_y} |\delta A_y(k, \omega, z)|^2, \quad (4.75)$$

where we have used Eq. (4.73). The quantity Q^{ad} is purely imaginary, that is, Q^{ad} corresponds to the reactive part of energy transfer and is reversible. Q^{ad} is related to the adiabatic change of current filament interaction energy.

The energy dissipated per unit time is given by

$$Q(k, \omega) = \frac{1}{2} \operatorname{Re} \int d^3x \delta\mathbf{J}_{k, \omega} \cdot \delta\mathbf{E}_{k, \omega}^* = \frac{1}{2} \operatorname{Re} \int d^3x \delta\mathbf{J}_{k, \omega}^d \cdot \delta\mathbf{E}_{k, \omega}^*. \quad (4.76)$$

Hence, the time-averaged dissipated power is

$$\bar{Q} = \frac{1}{2} \operatorname{Re} \left(\lim_{T \rightarrow \infty} \int_{-T/2}^{T/2} \frac{dt}{T} \int d^3x \delta\mathbf{J}^d \cdot \delta\mathbf{E}^* \right), \quad (4.77)$$

where the time average removes the reversible part of the power transfer in $\delta\mathbf{J} \cdot \delta\mathbf{E}$. Introducing the effective conductivity σ given by

$$\sigma_{\alpha\beta}(k, \omega) = \lim_{T \rightarrow \infty} \frac{\int_{-T/2}^{T/2} \frac{dt}{T} \int d^3x \delta\mathbf{J}^d \cdot \delta\mathbf{E}^*}{\int_{-T/2}^{T/2} \frac{dt}{T} \int d^3x \delta E_\alpha^* \delta E_\beta}, \quad (4.78)$$

we find that the time averaged dissipated power is

$$\bar{Q}(k, \omega) = \frac{1}{2} \sigma_{\alpha\beta}^H(k, \omega) \lim_{T \rightarrow \infty} \int_{-T/2}^{T/2} \frac{dt}{T} \int d^3x \delta E_{\alpha k, \omega}^* \delta E_{\beta k, \omega}. \quad (4.79)$$

From Eq. (4.69) we have that

$$\begin{aligned} \lim_{T \rightarrow \infty} \int_{-T/2}^{T/2} \frac{dt}{T} \int d^3x \delta\mathbf{J}^d \cdot \delta\mathbf{E}^* &= \sum_j \frac{q_j^2}{T_j} \int d^6X_0 f_{0j} \lim_{T \rightarrow \infty} \int_{-T/2}^{T/2} \frac{dt}{T} \\ &\times \int_{-\infty}^t dt' \delta\mathbf{E}^*(z) \cdot \mathbf{v}\mathbf{v}' \cdot \delta\mathbf{E}(z') \\ &\times e^{i[k(x'-x) - \omega(t'-t)]}, \end{aligned} \quad (4.80)$$

where the phase space integration is performed over the initial conditions \mathbf{X}_0 ,

$$\mathbf{X}_0 \equiv (\mathbf{x}_0, \mathbf{v}_0), \quad (4.81)$$

and where

$$\mathbf{x} \equiv \mathbf{x}(t; \mathbf{X}_0) \text{ and } \mathbf{v} \equiv \mathbf{v}(t; \mathbf{X}_0). \quad (4.82)$$

are the position and velocity at time t of a charge moving in the unperturbed fields with initial conditions \mathbf{X}_0 .

Dissipation occurs due to the resonant interaction of the particles with the fluctuations. Outside the current sheet layer, that is, in the lobes of the geomagnetic tail, the magnetic field prevents the $\omega = \mathbf{k} \cdot \mathbf{v}$ resonance between the particles and the waves at low frequencies. At high frequencies ($\omega \sim \omega_{cx0}$) the resonance condition is given by a delta function $\delta(\omega - kv_x - l\omega_{cx0})$, with $l = 0, \pm 1, \pm 2, \dots$. Thus dissipation in the lobes occurs only at high frequencies. On the other hand, in the current sheet the magnetic fields are weak and the charges interact resonantly with low frequency waves. In particular, if we assume that the charges are streaming freely in the current sheet, the resonance condition becomes $\delta(\omega - kv_x)$.

Dissipation for low frequency phenomena ($\omega \ll \omega_{cx0}$), such as tearing modes, occurs only in the narrow layer where the effect of the lobe magnetic field can be neglected. The thickness of the resistive layer can be estimated by determining the critical value of z , Δ , which satisfies the condition

$$\rho_c = \Delta, \quad (4.83)$$

where ρ_c is the Larmor radius evaluated at $z = \Delta$. Approximating the magnetic field in the current sheet layer by $B_x(z) = B_{x0}z/L_z$, we get

$$\Delta = (\rho_0 L_z)^{1/2}, \quad (4.84)$$

where

$$\rho_0 = \frac{v_{th}}{\omega_{cx0}}. \quad (4.85)$$

4.2.1 Conductivity Formula

From the above considerations we have that for low frequency phenomena, dissipation occurs in the resistive layer with the characteristic half-thickness given by (4.84). Since the main contribution to (4.80) comes from the resistive layer with $|z| \lesssim \Delta$, the fields can be approximated by their values at $z = 0$ and taken out from the temporal integration in (4.80). Hence, the low frequency conductivity is given by

$$\begin{aligned} \sigma_{\alpha\beta}(k, \omega) &= \sum_j \frac{q_j^2}{T_j} \int d^6 X_0 f_{0j} \int_0^\infty d\tau e^{i\omega\tau} \\ &\quad \times \lim_{T \rightarrow \infty} \int_{-T/2}^{T/2} \frac{dt}{T} v_\alpha(t; \mathbf{X}_0) v_\beta(t - \tau; \mathbf{X}_0) \\ &\quad \times e^{ik[x(t-\tau; \mathbf{X}_0) - x(t; \mathbf{X}_0)]}, \end{aligned} \quad (4.86)$$

where the change of variables from t' to $\tau \equiv t - t'$ has been made.

At this point it is convenient to introduce some notation. From now on, the product $v(t; \mathbf{X}_0) e^{-ikx(t; \mathbf{X}_0)}$ will be denoted by $v(k, t; \mathbf{X}_0)$;

$$v(k, t; \mathbf{X}_0) \equiv v(t; \mathbf{X}_0) e^{-ikx(t; \mathbf{X}_0)}. \quad (4.87)$$

Ensemble averages over the initial conditions will be denoted by triangular brackets;

$$\int d^6 X_0 f_{0j} \dots \equiv n_0 \langle \dots \rangle_j. \quad (4.88)$$

Finally, we define single-particle, two-time velocity correlations by

$$C_{\alpha\beta}(k, \tau; \mathbf{X}_0) \equiv \lim_{T \rightarrow \infty} \int_{-T/2}^{T/2} \frac{dt}{T} v_\alpha(k, t; \mathbf{X}_0) v_\beta(-k, t - \tau; \mathbf{X}_0) \quad (4.89)$$

and we denote the one-sided Fourier transform of $C_{\alpha\beta}(k, \tau; \mathbf{X}_0)$ by $C_{\alpha\beta}(k, \omega; \mathbf{X}_0)$, that is,

$$C_{\alpha\beta}(k, \omega; \mathbf{X}_0) \equiv \int_0^{\infty} d\tau e^{i\omega\tau} C_{\alpha\beta}(k, \tau; \mathbf{X}_0). \quad (4.90)$$

Note that \mathbf{X}_0 has been included in the definition of Eq. (4.89) to stress the fact that the single particle velocity correlation tensor depends on the initial conditions. For ergodic systems the time integration in Eq. (4.89) can be replaced by averages over the ensemble of particles and the reference to the initial conditions \mathbf{X}_0 in Eq. (4.89) can be suppressed.

Substituting Eqs. (4.87)–(4.90) into Eq. (4.86), we find that the low frequency conductivity formula (4.86) can be written as

$$\sigma_{\alpha\beta}(k, \omega) = \sum_j \frac{n_j q_j^2}{m_j} \langle C_{\alpha\beta}(k, \omega; \mathbf{X}_0) \rangle_j. \quad (4.91)$$

The dissipative part of the conductivity corresponds to its Hermitian part, which according to Eq. (4.91) is determined by the Hermitian part of the correlation tensor,

$$C_{\alpha\beta}^H(k, \omega) \equiv \frac{1}{2} [C_{\alpha\beta}(k, \omega) + C_{\beta\alpha}^*(k, \omega)]. \quad (4.92)$$

From Eq. (4.89) we have that $C_{\alpha\beta}(k, \tau)$ has the following properties:

$$C_{\alpha\beta}^*(k, \tau) = C_{\alpha\beta}(-k, \tau) \quad (4.93)$$

and

$$C_{\alpha\beta}(k, -\tau) = C_{\beta\alpha}(-k, \tau). \quad (4.94)$$

From these properties it is easily verified that the Hermitian part of $C_{\alpha\beta}(k, \omega)$ is

$$C_{\alpha\beta}^H(k, \omega) = \tilde{C}_{\alpha\beta}(k, \omega), \quad (4.95)$$

where $\tilde{C}_{\alpha\beta}(k, \omega)$ is the Fourier transform of $C_{\alpha\beta}(k, \tau)$,

$$\tilde{C}_{\alpha\beta}(k, \omega) = \int_{-\infty}^{\infty} d\tau e^{i\omega\tau} C_{\alpha\beta}(k, \tau). \quad (4.96)$$

In this work we will refer to $\tilde{C}_{\alpha\beta}(k, \omega)$ as velocity power spectrum or spectral velocity correlations.

From (4.91) and (4.95) it follows that the dissipative part of the conductivity is given by

$$\sigma_{\alpha\beta}^H(k, \omega) = \sum_j \frac{n_j q_j^2}{m_j} \tau_{cj}, \quad (4.97)$$

where the correlation time τ_c (the effective "collisional time") is defined as

$$\tau_{cj} = \frac{1}{2v_{ihj}^2} \langle \tilde{C}_{\alpha\beta}(k, \omega; \mathbf{X}_0) \rangle_j. \quad (4.98)$$

In tail-like magnetic field reversals the conductivity depends on the finite Larmor radius parameter $\epsilon \equiv \rho/L_z$, and on the magnetic field components $b_y \equiv B_y/B_{x0}$ and $b_z \equiv B_z/B_{x0}$;

$$\sigma_{\alpha\beta}(k, \omega) = \sigma_{\alpha\beta}(k, \omega; b_y, b_z, \epsilon). \quad (4.99)$$

Eqs. (4.91), (4.97), and (4.98) are the main results of this chapter.

The relationship between $\sigma_{\alpha\beta}$ and the dielectric tensor is given by (4.24). The low-frequency conductivity formula (4.97) contains all the information about the response of the medium to electromagnetic perturbations and about wave propagation. Once the dissipative part of the conductivity has been determined, its reactive part $\sigma_{\alpha\beta}^A(k, \omega)$ can be determined from the Kramers-Kronig relations (4.41).

4.2.2 Frequency Sum Rule

Consider the integral over all the frequencies of the dissipative part of the conductivity. From (4.97), (4.98), and (4.96) we get

$$\int_{-\infty}^{\infty} d\omega \sigma_{\alpha\beta}^H(k, \omega) = \pi \sum_j \frac{n_j q_j^2}{m_j v_{thj}^2} \langle C_{\alpha\beta}(k, \tau = 0) \rangle_j. \quad (4.100)$$

Noting that

$$\langle C_{\alpha\beta}(k, \tau = 0) \rangle = v_{th}^2 \delta_{\alpha\beta} + U_y^2 \delta_{\alpha y} \delta_{\beta y}, \quad (4.101)$$

we obtain the frequency-sum rule

$$\int_{-\infty}^{\infty} d\omega \sigma_{\alpha\beta}^H(k, \omega) = \pi \sum_j \frac{n_j q_j^2}{m_j} \left[\delta_{\alpha\beta} + \left(\frac{U_y}{v_{th}} \right)_j^2 \delta_{\alpha y} \delta_{\beta y} \right], \quad (4.102)$$

which has been verified in all our numerical experiments.

The frequency-sum rule (4.102) means that regardless of the details of the absorption spectrum the total amount of dissipation is constant. In the lobe region ($|z/L_z| \gg 1$), where the particles execute cyclotron motion around the magnetic field lines, the main contribution to the total dissipation is due to the high frequencies centered around the cyclotron frequency ω_{cx0} for the asymptotic field B_{x0} , as shown in Fig. 5.2. On the other hand, in the dissipative layer ($|z| \leq (\rho L_z)^{1/2}$), chaotic particle motion spreads the dissipation to low frequencies and the frequency-sum rule (4.102) has contributions from a broad band of absorption frequencies. In general, for inhomogeneous systems, dissipation is spread to low frequencies ($\omega \ll \omega_{cx0}$) even if the motion is integrable [Horton *et al.*, 1994]. This is illustrated in Fig. 5.1 which shows the electrical conductivity σ_{yy} in the dissipative layer for the case of a straight magnetic field reversal, where the motion is integrable.

4.2.3 Summary

In this section we have developed the spectral velocity correlations formalism for the calculation of the space-time-averaged conductivity. Numerically, the formalism consists of the following steps:

1. Launch an ensemble of N particles distributed in phase space according to the equilibrium distribution function f_0 .
2. For each particle integrate the equations of motion in the unperturbed fields and compute the corresponding power spectra $\tilde{C}_{\alpha\beta}^{(j)}(k, \omega; \mathbf{X}_{0j})$, $j = 1, 2, \dots, N$.
3. Average over all the particles,

$$\sigma_{\alpha\beta}^H(k, \omega) = \frac{q^2}{mv_{th}^2} \frac{1}{N} \sum_{j=1}^N \tilde{C}_{\alpha\beta}^{(j)}(k, \omega; \mathbf{X}_{0j}). \quad (4.103)$$

4. As a consistency test, check the frequency-sum rule (4.102).

The procedure just described is essential when it is impractical to integrate analytically the motion of the particles or when the dynamics is non-integrable.

In the following sections we illustrate the formalism with several well known examples, apply the formalism to tail-like magnetic field reversals and use the results to estimate tearing mode growth rates.

4.3 Collisionless Conductivity and Fluctuation Dissipation Relations

Based on the idea that for a system close to thermodynamic equilibrium, the evolution towards equilibrium does not depend on whether the system

was set out of equilibrium by an external perturbation or by an spontaneous fluctuation, a link can be established between the microscopic fluctuations and the response functions of the system. In particular, linear response theory leads to the so-called Green-Kubo formulae [eg., *Kubo*, 1957] which are general relations connecting transport coefficients and autocorrelation functions of fluctuating quantities. Taking Fourier transforms of the Green-Kubo formulae, general relations between spectral correlations of microscopic fluctuations and the dissipative part of the transport coefficients are obtained. These general relations are called fluctuation-dissipation relations [*Callen and Welton*, 1951; *Kubo et al.*, 1985; *Landau*, 1969; *Sitenko*, 1982; *Klimontovich*, 1991; *Cable and Tajima*, 1992].

The fluctuation-dissipation theorem was obtained by *Callen and Welton* [1951]. A careful derivation of the theorem is given by *Sitenko* [1982] from time-dependent perturbation theory in the interaction representation, and by *Schram* [1991] from the classical Liouville equation. Here we just state the theorem without proof and discuss its relation to the conductivity formula (4.97).

Consider a system in thermodynamic equilibrium. In the absence of external perturbations, the Hamiltonian is independent of time and is denoted by $H_0(\Gamma)$, where Γ is an abbreviation for the $6N$ independent variables:

$$\Gamma = \{\mathbf{X}_1, \dots, \mathbf{X}_N\}, \quad \mathbf{X}_i \equiv \{\mathbf{x}_i, \mathbf{v}_i\}, \quad (4.104)$$

with \mathbf{x}_i and \mathbf{v}_i the position and the velocity of the i -th particle, respectively. When the system is perturbed by an external agency, the Hamiltonian takes the form

$$H(\Gamma, t) = H_0(\Gamma) + \delta H(\Gamma, t). \quad (4.105)$$

Assume that δH has the form

$$\delta H(\Gamma, t) = - \int d^3x \mathbf{J}(\mathbf{x}, t; \Gamma) \cdot \mathbf{A}(\mathbf{x}, t), \quad (4.106)$$

where $\mathbf{A}(\mathbf{x}, t)$ represents the external agency which is coupled to the system through the microscopic quantity $\mathbf{J}(\mathbf{x}, t; \Gamma)$. For example, in the case of a system of charged particles in the presence of an external electrostatic field $\Phi(\mathbf{x}, t)$, we have

$$\delta H(\Gamma, t) = \int d^3x \rho(\mathbf{x}, t; \Gamma) \Phi(\mathbf{x}, t), \quad (4.107)$$

where $\rho(\mathbf{x}, t; \Gamma)$ is the charge density given by

$$\rho(\mathbf{x}, t; \Gamma) = \sum_{i=1}^N q_i \delta(\mathbf{x} - \mathbf{x}_i(t)). \quad (4.108)$$

For a system of magnetic dipoles in an external magnetic field, we have

$$\delta H(\Gamma, t) = - \int d^3x \mathbf{M}(\mathbf{x}, t; \Gamma) \cdot \mathbf{B}(\mathbf{x}, t), \quad (4.109)$$

where $\mathbf{M}(\mathbf{x}, t; \Gamma)$ is the magnetization

$$\mathbf{M}(\mathbf{x}, t; \Gamma) = \sum_{i=1}^N \boldsymbol{\mu}_i \delta(\mathbf{x} - \mathbf{x}_i(t)). \quad (4.110)$$

Finally, for an electromagnetic perturbation given by the vector potential

$\mathbf{A}(\mathbf{x}, t)$, we have

$$\delta H(\Gamma, t) = - \int d^3x \mathbf{J}(\mathbf{x}, t; \Gamma) \cdot \mathbf{A}(\mathbf{x}, t), \quad (4.111)$$

where $\mathbf{J}(\mathbf{x}, t; \Gamma)$ is the current density

$$\mathbf{J}(\mathbf{x}, t; \Gamma) = \sum_{i=1}^N q_i \mathbf{v}_i(t) \delta(\mathbf{x} - \mathbf{x}_i(t)). \quad (4.112)$$

We will also assume a linear causal response of the medium to the perturbing potential

$$\mathbf{J}(\mathbf{x}, t) = \int_{-\infty}^t dt' \int d^3x' \mathbf{K}(\mathbf{x}, \mathbf{x}', t, t') \cdot \mathbf{A}(\mathbf{x}', t'). \quad (4.113)$$

Then, for the Fourier components of \mathbf{J} and \mathbf{A} we can write

$$\mathbf{J}(\mathbf{k}, \omega) = \mathbf{K}(\mathbf{k}, \omega) \cdot \mathbf{A}(\mathbf{k}, \omega), \quad (4.114)$$

where $K_{\alpha\beta}$ is the response tensor of the medium.

The fluctuation-dissipation theorem relates the spectral correlations of current density fluctuations to the dissipative properties of the medium and is given [Callen and Welton, 1951] by

$$\langle J_{\alpha}^* J_{\beta} \rangle_{\mathbf{k}\omega} = \frac{\hbar}{\exp(\hbar\omega/T) - 1} i \{ K_{\alpha\beta}^*(\mathbf{k}, \omega) - K_{\beta\alpha}(\mathbf{k}, \omega) \}, \quad (4.115)$$

which in the classical limit ($T \gg \hbar\omega$) becomes

$$\langle J_{\alpha}^* J_{\beta} \rangle_{\mathbf{k}\omega} = \frac{T}{\omega} i \{ K_{\alpha\beta}^*(\mathbf{k}, \omega) - K_{\beta\alpha}(\mathbf{k}, \omega) \}. \quad (4.116)$$

In writing Eqs. (4.115) and (4.116) we are assuming that the system is in thermal equilibrium at the temperature T .

In the derivation of (4.115) the average energy absorbed by the medium per unit time Q is calculated using time-dependent perturbation theory, with the perturbation given by (4.106), and by performing two averages: one over the quantum state of the system and one over the statistical distribution of the different quantum states of the system, which for equilibrium states is given by the canonical distribution

$$D(E_n) = \exp\{(F - E_n)/T\}, \quad (4.117)$$

where F is the free energy and T the temperature of the system. The result is

$$Q = \frac{\omega}{4\hbar} [\exp(\hbar\omega/T) - 1] \sum_{\mathbf{k}, \mathbf{k}', \alpha, \beta} A_{\alpha}(\mathbf{k}, \omega) A_{\beta}(\mathbf{k}', \omega) \langle J_{\alpha}^{\dagger}(\mathbf{k}) J_{\beta}(\mathbf{k}') \rangle_{\omega}. \quad (4.118)$$

On the other hand, the change in the internal energy of the system is given by

$$\frac{dH}{dt} = \frac{\partial H}{\partial t} = - \int d^3x \mathbf{J}(\mathbf{x}, t) \cdot \dot{\mathbf{A}}(\mathbf{x}, t). \quad (4.119)$$

Fourier transforming this expression and using (4.114), the average energy absorbed per unit time is

$$Q = \frac{1}{4} i\omega \sum_{\mathbf{k}, \alpha, \beta} (K_{\alpha\beta}^* - K_{\beta\alpha}) A_{\alpha}(\mathbf{k}, \omega) A_{\beta}^*(\mathbf{k}, \omega). \quad (4.120)$$

Comparing Eqs. (4.118) and (4.120), we obtain the fluctuation-dissipation relation of Eq. (4.115) [Sitenko, 1982].

The fluctuation-dissipation theorem can be used in several ways. If the response tensor $K_{\alpha\beta}(\mathbf{k}, \omega)$ is known (for example, the dielectric tensor for a uniform plasma both in the absence and in the presence of a constant magnetic field), then the spectral distribution of \mathbf{J} can be found. On the other hand, if we somehow know the fluctuation spectra of \mathbf{J} , then we can invert (4.115) and determine the response properties of the medium (this is like using the absorption lines in a spectrum to determine the dielectric properties of the medium). The later approach is the one we use in this work: we want to calculate the collisionless conductivity from the numerical computation of the spectral velocity correlations.

For the specific case of electromagnetic perturbations, the response tensor $K_{\alpha\beta}(\mathbf{k}, \omega)$ is given in terms of the electrical conductivity $\sigma_{\alpha\beta}(\mathbf{k}, \omega)$ through

$$K_{\alpha\beta}(\mathbf{k}, \omega) = i\omega\sigma_{\alpha\beta}(\mathbf{k}, \omega), \quad (4.121)$$

and the fluctuation-dissipation relation which follows from substituting (4.121) into (4.116) gives

$$\sigma_{\alpha\beta}^H(\mathbf{k}, \omega) = \sum_j \frac{1}{2m_j v_{thj}^2} \int_{-\infty}^{\infty} d\tau e^{i\omega\tau} \langle J_\alpha(\mathbf{k}, t) J_\beta(-\mathbf{k}, t - \tau) \rangle_j, \quad (4.122)$$

Formula (4.122) is the so-called Kubo conductivity formula [Kubo *et al.*, 1985]. Expression (4.122) has to be compared with expression (4.97) for the collisionless conductivity. The space-time-averaged conductivity formula (4.97) is more general than the statistical equilibrium conductivity formula (4.122). To the extent that the orbits are ergodic so that the ensemble-averaged two-time velocity correlation function $\langle v_\alpha(\mathbf{k}, t) v_\beta(-\mathbf{k}, t - \tau) \rangle$ is the same as the time-averaged velocity correlation function in (4.89), the Kubo conductivity formula is identical to the space-time averaged conductivity (4.97).

4.4 Conductivity for an Unmagnetized Plasma

In order to appreciate the conceptual difference between the space-time-averaged conductivity and the Kubo conductivity formula, we consider the case of a uniform unmagnetized equilibrium plasma. The derivation of the dissipative part of the conductivity from the Kubo formula is given in Sitenko [1982].

4.4.1 Conductivity from Kubo's Formula

Consider a collisionless, uniform, homogeneous, and unmagnetized plasma. There are no forces acting on the system, thus the particles move along straight-line trajectories,

$$\mathbf{x}_i(t) = \mathbf{x}_i(t_0) + \mathbf{v}_i(t - t_0),$$

$$\mathbf{v}_i(t) = \mathbf{v}_i = \text{const.}, \quad (4.123)$$

with the microscopic distribution function

$$F(\mathbf{x}, \mathbf{v}, t; \Gamma) = \frac{1}{N} \sum_{i=1}^N \delta(\mathbf{x} - \mathbf{x}_i(t)) \delta(\mathbf{v} - \mathbf{v}_i(t)). \quad (4.124)$$

One obtains the connection between microscopic quantities and macroscopic quantities by taking averages over ensembles of systems, which differ only in the particle states, and by considering the distribution of the systems in the different states. This distribution is the Liouville distribution $D(\Gamma)$, which is defined as the density of the systems in Γ -space:

$$D(\Gamma) = \lim_{M \rightarrow \infty} \frac{dM_\Gamma}{M}, \quad (4.125)$$

where M is the number of systems in the ensemble and dM_Γ is the number of systems in the element $d\Gamma$.

The Liouville distribution for a system of non-interacting particles reduces to the product of single-particle distribution functions:

$$D(\Gamma) = \prod_{i=1}^N f_0(\mathbf{v}_i), \quad (4.126)$$

where the single-particle distribution $f_0(\mathbf{v}_i)$ does not depend on \mathbf{x}_i and t because the medium is assumed to be spatially homogeneous and stationary. If the system is in thermal equilibrium, then $f_0(\mathbf{v})$ is the Maxwellian distribution, with the parameter $\beta = 1/k_B T$ specifying the thermal equilibrium.

Averaging the microscopic distribution (4.124) over the Liouville distribution (4.126) we obtain

$$\langle F(\mathbf{x}, \mathbf{v}, t; \Gamma) \rangle = f_0(\mathbf{v}). \quad (4.127)$$

The fluctuations of the microscopic distribution (4.124) for a system of non-interacting particles are given by

$$\delta F(\mathbf{x}, \mathbf{v}, t; \Gamma) = F(\mathbf{x}, \mathbf{v}, t; \Gamma) - f_0(\mathbf{v}), \quad (4.128)$$

and the two-time, two-point correlations for the fluctuations in the distribution function are given by

$$\begin{aligned} \langle \delta F(\mathbf{x}, \mathbf{v}, t; \Gamma) \delta F(\mathbf{x}', \mathbf{v}', t'; \Gamma) \rangle &= \langle \sum_i \delta(\mathbf{x} - \mathbf{x}_i(t)) \delta(\mathbf{v} - \mathbf{v}_i) \delta(\mathbf{x}' - \mathbf{x}_i(t')) \\ &\quad \times \delta(\mathbf{v}' - \mathbf{v}_i) \rangle \\ &= \delta[\mathbf{x} - \mathbf{x}' - \mathbf{v}\tau] \delta(\mathbf{v} - \mathbf{v}') f_0(\mathbf{v}), \end{aligned} \quad (4.129)$$

where in going from the first line to the second line we have used Eq. (4.123), and where $\tau = t - t'$.

The meaning of Eq. (4.129) is that fluctuations in the distribution function at two different points, \mathbf{x} and \mathbf{x}' , and at two different times, t and t' , are correlated if a particle with velocity \mathbf{v} can traverse the distance $\mathbf{x} - \mathbf{x}'$ during the time τ .

Taking the Fourier transform of (4.129) we obtain the spectral correlation between fluctuations of the distribution function:

$$\langle \delta F(\mathbf{v}) \delta F(\mathbf{v}') \rangle_{\mathbf{k}\omega} = 2\pi \delta(\omega - \mathbf{k} \cdot \mathbf{v}) \delta(\mathbf{v} - \mathbf{v}') f_0(\mathbf{v}). \quad (4.130)$$

The particle density distribution $n(\mathbf{x}, t; \Gamma)$ is obtained integrating Eq. (4.124) over \mathbf{v} . The result is

$$\begin{aligned} n(\mathbf{x}, t; \Gamma) &= \sum_{i=1}^N \delta(\mathbf{x} - \mathbf{x}_i(t)) \\ &= \sum_{\mathbf{k}} n_{\mathbf{k}}(t) e^{i\mathbf{k} \cdot \mathbf{x}}, \end{aligned} \quad (4.131)$$

where

$$n_{\mathbf{k}}(t) = \sum_{i=1}^N e^{-i\mathbf{k}\cdot\mathbf{x}_i(t)}. \quad (4.132)$$

Similarly, the current density $\mathbf{J}(\mathbf{x}, t; \Gamma)$ is obtained multiplying Eq. (4.124) by $q\mathbf{v}$ and integrating over \mathbf{v} . The result is

$$\begin{aligned} \mathbf{J}(\mathbf{x}, t; \Gamma) &= q \sum_{i=1}^N \mathbf{v}_i(t) \delta(\mathbf{x} - \mathbf{x}_i(t)) \\ &= q \sum_{\mathbf{k}} \mathbf{v}_{\mathbf{k}}(t) e^{i\mathbf{k}\cdot\mathbf{x}}, \end{aligned} \quad (4.133)$$

where

$$\mathbf{v}_{\mathbf{k}}(t) = \sum_{i=1}^N \mathbf{v}_i(t) e^{-i\mathbf{k}\cdot\mathbf{x}_i(t)}. \quad (4.134)$$

The spectral correlations between density fluctuations are obtained integrating Eq. (4.130) twice over the velocities,

$$\langle \delta n^2 \rangle_{\mathbf{k}\omega} = 2\pi \int d^3v \delta(\omega - \mathbf{k} \cdot \mathbf{v}) f_0(\mathbf{v}). \quad (4.135)$$

Similarly, the spectral correlations between current density fluctuations are obtained multiplying Eq. (4.130) by $\mathbf{v}\mathbf{v}'$ and integrating twice over the velocities,

$$\langle J_{\alpha} J_{\beta} \rangle_{\mathbf{k}\omega} = 2\pi q^2 \int d^3v v_{\alpha} v_{\beta} \delta(\omega - \mathbf{k} \cdot \mathbf{v}) f_0(\mathbf{v}). \quad (4.136)$$

Taking the distribution $f_0(\mathbf{v})$ to be the Maxwellian distribution function $f_M(\mathbf{v})$,

$$f_M(\mathbf{v}) = n_0 \frac{1}{(2\pi)^{3/2} v_{th}^3} \exp[-v^2/2v_{th}^2], \quad (4.137)$$

substituting (4.137) into (4.136) and substituting the result into Kubo's conductivity formula (4.122), we obtain the well-known result

$$\text{Re}\sigma = \sqrt{\frac{\pi}{2}} \frac{n_0 q^2}{m |k| v_{th}} \begin{pmatrix} \frac{\omega^2}{k^2 v_{th}^2} & 0 & 0 \\ 0 & 1 & 0 \\ 0 & 0 & 1 \end{pmatrix} \exp\left(-\frac{\omega^2}{2k^2 v_{th}^2}\right), \quad (4.138)$$

where we have taken the wave vector \mathbf{k} to be along the x -axis.

4.4.2 Conductivity from the Spectral Velocity Correlations Formalism

For comparison with the Kubo formula method we now consider the calculation of the conductivity from the spectral velocity correlations formalism of Section 4.2.

Substituting (4.123) into (4.89) and substituting the result into (4.96), we obtain the single-particle spectral correlation

$$\tilde{C}_{\alpha\beta} = 2\pi v_{\alpha} v_{\beta} \delta(\omega - \mathbf{k} \cdot \mathbf{v}). \quad (4.139)$$

Averaging (4.139) over the Maxwellian distribution and substituting the result into (4.98), we recover the conductivity formula (4.138).

The numerical calculation of the conductivity formula from the spectral velocity correlations formalism is illustrated in Fig. 4.2. Fig. 4.2 displays plots for (a) the transverse and (b) the longitudinal components of the dissipative part of the conductivity for the unmagnetized plasma. We obtained both plots by launching $N = 3000$ particles according to a Maxwellian distribution and following the spectral velocity correlations formalism described at the end of Section 4.2. The impulse lines in the plots correspond to our numerical results (4.103) for the discrete frequency components, and the solid curves correspond to the analytical result (4.138). We can see that the numerical results are in good agreement with the analytical formula in this limit of straight line trajectories. The frequency sum rule was verified for both the transverse and longitudinal components of the conductivity since the numerical values 3.04 and 3.028 were obtained, which are close to π , within $1/30$, as desired.

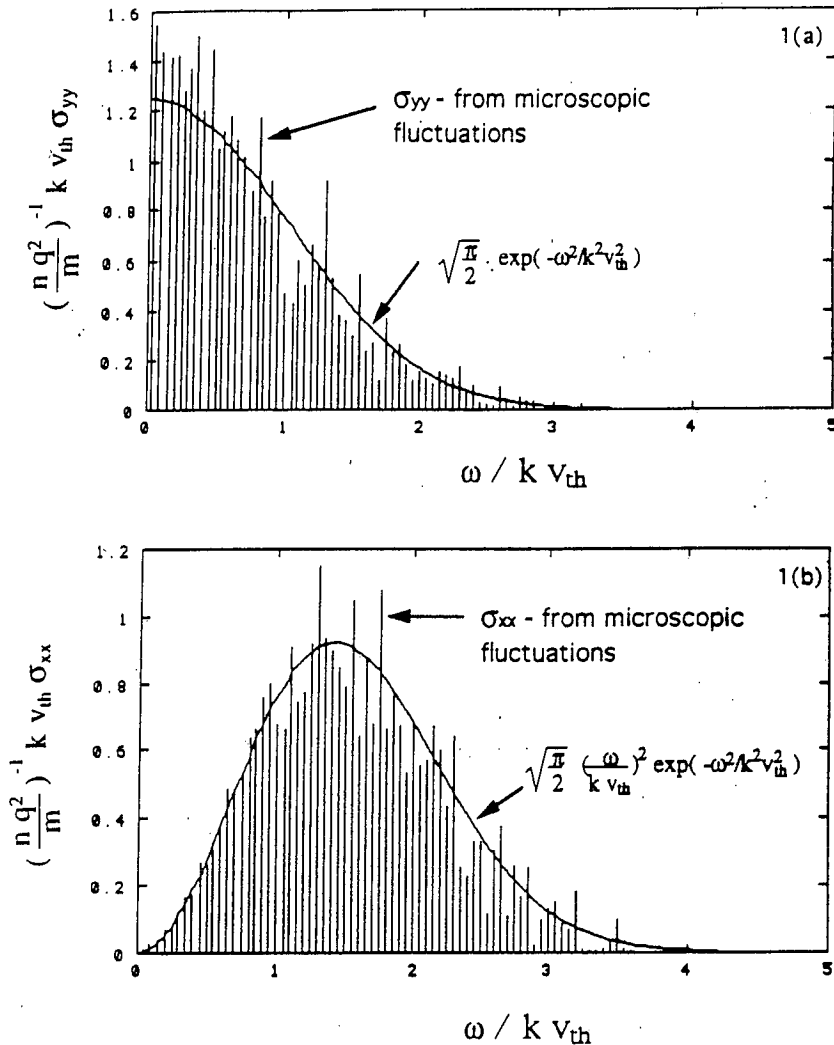


Figure 4.2: Conductivity for unmagnetized plasma. (a) Transverse and (b) longitudinal components of the dissipative part of the conductivity for perturbations propagating along the x -axis. In both plots the solid curves represent the theoretical conductivities (4.138) and the impulse lines represent the conductivities from microscopic fluctuations obtained numerically with the SVC formalism of Section 4.2. We generated the results by launching $N = 3000$ particles distributed according to a Maxwellian distribution in velocity and uniformly distributed along the x -axis from $x = 0$ up to $x = 2\pi/k$.

4.5 Kaufman Conductivity for Inhomogeneous Systems

Kaufman and coworkers [*Kaufman and Nakayama*, 1970; *Kaufman*, 1971] have studied the collisionless conductivity for inhomogeneous systems that support integrable motion. In particular, here we follow closely *Kaufman and Nakayama* [1970] who considered the case of a one-dimensional system of charged particles confined by an electrostatic potential $\Phi(x)$.

The Hamiltonian of the system is

$$H(x, p, t) = \mathcal{E}(x, p) + q\phi(x, p, t), \quad (4.140)$$

where the unperturbed energy is

$$\mathcal{E}(x, p) = \frac{p^2}{2m} + q\Phi(x) \quad (4.141)$$

and where $\phi(x, p, t)$ is a time-dependent electrostatic perturbation.

The linearized Vlasov equation is

$$\frac{\partial \delta f}{\partial t} + v \frac{\partial \delta f}{\partial x} - q \frac{d\Phi}{dx} \frac{\partial \delta f}{\partial v} = - \frac{\partial f_0}{\partial \mathcal{E}} qv E(x, t), \quad (4.142)$$

where $f_0(x, p) = f_0(\mathcal{E})$ is the equilibrium distribution function and $f_0 + \delta f(x, p, t)$ is the linear approximation to the perturbed distribution function.

Let μ denote the initial conditions in phase space, $\mu \equiv (x_0, p_0)$, of an unperturbed trajectory which at time t is at (x, p) . The current density at x' and time t for a particle with initial conditions μ is given by

$$J(x', t; \mu) \equiv qv(t; \mu) \delta[x' - x(t; \mu)]. \quad (4.143)$$

From (4.143) we have that the right hand side of (4.142) can be written as

$$- f_{0,\mathcal{E}} qv E(x, t) = - f_{0,\mathcal{E}} \int dx' J(x', t; \mu) E(x', t) \quad (4.144)$$

and the solution of (4.142) is

$$\delta f(t; \mu) = -f_{0,\varepsilon} \int_0^\infty d\tau \int dx' J(x', t - \tau; \mu) E(x', t - \tau). \quad (4.145)$$

On the other hand, the average current density is given by

$$J(x, t) \equiv \int d\mu J(x, t; \mu) \delta f(t; \mu) \quad (4.146)$$

and the conductivity is defined through the relation

$$J(x, t) = \int_0^\infty d\tau \int dx' \sigma(x, x', \tau) E(x', t - \tau). \quad (4.147)$$

Inserting (4.145) into (4.146) and comparing the resulting expression with (4.147), we have that the conductivity kernel is given by

$$\sigma(x, x', \tau) = - \int d\mu f_{0,\varepsilon} J(x, t; \mu) J(x', t - \tau; \mu), \quad (4.148)$$

which generalizes the Kubo conductivity formula for an inhomogeneous, one-dimensional, Vlasov system. If the steady-state distribution f_0 is a Maxwellian, then (4.148) reduces to the Kubo-like relation

$$\sigma(x, x', \tau) = \frac{1}{mv_{th}^2} \langle J(x, t) J(x', t - \tau) \rangle_0. \quad (4.149)$$

From (4.147) we obtain

$$J(x, \omega) = \int dx' \sigma(x, x', \omega) E(x', \omega), \quad (4.150)$$

where $E(x, \omega)$ is the Fourier transform of $E(x, t)$ and $\sigma(x, x', \omega)$ is the one-sided Fourier transform of $\sigma(x, x', t)$.

The dissipative part of the conductivity is given by its Hermitian part

$$\begin{aligned} \sigma^H(x, x', \omega) &= \frac{1}{2} [\sigma(x, x', \omega) + \sigma^*(x, x', \omega)] \\ &= \lim_{T \rightarrow \infty} \left[-\frac{1}{2T} \int d\mu f_{0,\varepsilon} J(x, \omega; \mu) J^*(x', \omega; \mu) \right], \end{aligned} \quad (4.151)$$

where

$$J(x, \omega; \mu) \equiv \lim_{T \rightarrow \infty} \int_{-T/2}^{T/2} dt e^{i\omega t} J(x, t; \mu). \quad (4.152)$$

Introducing the action-angle variables in the unperturbed system,

$$I = \oint p dx \quad (4.153)$$

and

$$\nu(I) = \frac{d\mathcal{E}}{dI}, \quad (4.154)$$

the Hermitian part of the conductivity is given by

$$\sigma^H(x, x', \omega) = 2q^2 \int dI f_{0,I} \sin(\omega\tau_L) \sin(\omega\tau_R) \frac{1}{\omega_b(I)} \sum_{\ell} \delta(\ell\omega_b(I) - \omega), \quad (4.155)$$

where τ_L is the time it takes for a particle with action I to go from its left turning point to the smaller of x and x' , τ_R is the time from the right turning point to the greater of x and x' , and $\omega_b(I) \equiv 2\pi\nu(I)$ is the bounce frequency. From (4.155) we have that the particles transfer energy to the waves if their bounce frequency is an integral sub-multiple of the wave frequency.

The explicit evaluation of the conductivity, such as in (4.155), is possible only if particle motion in the undisturbed system is integrable. If particle motion in the unperturbed system is chaotic, then the orbital mixing of frequencies, which is reflected in a broad band power spectrum, eliminates the δ -functions and the transfer of energy between the particles and the waves can occur for a broad band of frequencies. Thus, chaotic particle motion has the potential of increasing the band width of dissipation, as will be illustrated in the next Chapter.

Even in the case of integrable orbits the problem of determining $\omega_b(I)$ and $\sigma(x, x', \omega)$ can often only be determined numerically. In this case the

spectral velocity correlations formalism gives a fast, flexible, physically based procedure for calculating transport properties of the system.

Chapter 5

Chapter 5. Conductivity for the Central Plasma Sheet with Applications to Tearing Modes

5.1 Collisionless Conductivity for the Harris Sheet

Because of the presence of an electric field E_y in the tail, we are interested in the dawn-dusk component of the collisionless conductivity σ_{yy} . Inside the $\Delta \equiv (\rho L_z)^{1/2}$ layer, charged particles stream freely and their motion can be approximated with straight-line orbits

$$\begin{aligned} \mathbf{x} &= \mathbf{x}_0 + \mathbf{v}t, \\ \mathbf{v} &= \mathbf{v}_0. \end{aligned} \tag{5.1}$$

Under the straight-line approximation (5.1) the dawn-dusk component of the velocity correlations is given by

$$C_{yy}(k, \tau) = v_y^2 e^{-ikv_x \tau} \tag{5.2}$$

and the power spectrum is given by

$$\tilde{C}_{yy}(k, \omega) = 2\pi v_y^2 \delta(\omega - kv_x). \tag{5.3}$$

Taking the ensemble average of (5.3);

$$\langle \tilde{C}_{yy}(k, \omega) \rangle_j = \int_{-\Delta_j}^{\Delta_j} \frac{dz}{L_z} \int d^3v f_j(z, \mathbf{v}) \tilde{C}_{yy}(k, \omega), \tag{5.4}$$

and substituting the result into (4.97) we obtain the following expression for the dissipative part of the collisionless conductivity

$$\sigma_{yy}(k, \omega) = \left(\frac{\pi}{2}\right)^{1/2} \sum_j \frac{n_j q_j^2}{m_j} \frac{\epsilon_j^{1/2}}{k v_{thj}} \left(1 + \frac{U_{yj}^2}{v_{thj}^2}\right) \exp(-\omega^2/2k^2 v_{thj}^2), \quad (5.5)$$

where the main contribution to the conductivity comes from the electrons.

In the dc limit ($\omega = 0$) and neglecting $U_y/v_{th} = 2\epsilon \ll 1$, where $\epsilon \equiv \rho/L_z$, we reduce Eq. (5.5) to

$$\sigma_{yy} = \epsilon_e^{1/2} \sigma^{G-Z}, \quad (5.6)$$

where σ^{G-Z} is the *Galeev and Zelenyi* [1979] conductivity

$$\sigma^{G-Z} = \left(\frac{\pi}{2}\right)^{1/2} \frac{n_e e^2}{m_e} \frac{1}{|k| v_{the}}, \quad (5.7)$$

and where we obtain the weighting factor $\epsilon_e^{1/2}$ by noting that σ^{G-Z} vanishes outside the Δ_e layer and averaging over z . Taking $k = 1/2L_z$ and using the reference parameters of Table 1.1, we find that the correlation time is $\tau_{ce}^{G-Z} \approx 1$ s, the half-width of the unmagnetized layer is $(\rho_e L_z)^{1/2} = 160$ km, and the conductivity is $\sigma^{G-Z} \sim 10^{-2}$ mho/m. For substorm time scales we require $\tau_{ce}^{G-Z} \sim 10^{-3}$ sec and $\sigma^{G-Z} \sim 10^{-5}$ mho/m.

Fig. 5.1 is a plot of the dissipative part of the conductivity produced by the microscopic fluctuations from charged particles trapped in the plasma sheet. We obtained the plot by launching $N = 1000$ particles distributed according to the Harris distribution of Eq. (4.63) with number density $n(z) = n_0 \text{sech}^2(z/L_z)$ for $|z/L_z| < 1$, with $U_y/v_{th} = 2\epsilon = 0.08$, $\omega_{ce0}/\omega_{bz} = 5$, and with $k v_{th}/\omega_{bz} = 0.02$. Note that the dc value of the conductivity is nothing else than the value expected from the Galeev-Zelenyi conductivity (5.7) with the weighting factor $\epsilon^{1/2} = 0.2$.

Fig. 5.2 displays the dissipative part of the conductivity produced by the microscopic fluctuations from charged particles located away from the plasma sheet, that is, well into the region where the magnetic field is nearly uniform, $\mathbf{B}(z) \approx B_{x0}\hat{\mathbf{e}}_x$. Initially the particles were uniformly distributed in the range $3 \leq z/L_z \leq 4$, where the magnetic field is uniform to within 0.5%. The rest of the simulation parameters are the same as those in Fig. 5.1. Note that the only significant contribution to the conductivity occurs for $\omega \approx \omega_{cx0}$, which is in agreement with the assumption that the low-frequency component of the conductivity arises from particles in the current sheet.

The possibility of collisionless magnetic reconnection in a straight magnetic field reversal was proposed by *Coppi et al.* [1966]. These authors showed that the Harris sheet is tearing-unstable for long wavelength ($kL_z \ll 1$) perturbations for which the energy released by the pinching of the current filaments exceeds the energy spent in the creation of the perturbed magnetic field. The mechanism for energy dissipation is given by the transfer of energy from the plasma to a fraction of the electrons through the resonant interaction of the waves with the particles in the layer of thickness $\Delta_e = (\rho_e L_z)^{1/2}$, where the particles stream freely.

From Ampère's law we have that the perturbed vector potential and the perturbed current density are related through

$$\nabla^2 \delta A_y = -\mu_0(\delta J_y^{ad} + \delta J_y^d). \quad (5.8)$$

Substituting (4.73) into (5.8) we get

$$\left[\frac{d^2}{dz^2} - k^2 - \frac{B_x''(z)}{B_x(z)} \right] \delta A_y(z) = -\mu_0 \delta J_y^d, \quad (5.9)$$

where the primes denote derivatives with respect to z .

In the outer region we have $\delta J_y^d = 0$, and $\delta A_y(z)$ satisfies the homogeneous equation

$$\left[\frac{d^2}{dz^2} - k^2 - \frac{B_x''(z)}{B_x(z)} \right] \delta A_y(z) = 0, \quad (5.10)$$

which has the even-parity solution

$$\delta A_y(z) = \delta A_y(0) e^{-k|z|} \left[1 + \frac{1}{kL_z} \tanh \left(\frac{|z|}{L_z} \right) \right], \quad (5.11)$$

satisfying the boundary conditions

$$\lim_{|z| \rightarrow \infty} \delta A_y(z) = 0. \quad (5.12)$$

The odd modes $\delta A_y(-z) = -\delta A_y(z)$ describe a flopping or kinking of the current sheet.

The matching between the inner and outer regions is achieved through the matching parameter Δ' defined by

$$\Delta' \equiv \left(\frac{d \ln(\delta A_y(z))}{dz} \right)_{-\Delta_e}^{+\Delta_e}, \quad (5.13)$$

which for the solution (5.11) is given by

$$\Delta'_k L_z = \frac{2}{kL_z} (1 - k^2 L_z^2). \quad (5.14)$$

Integrating (5.9) with respect to z in the $\Delta_e \equiv (\rho_e L_z)^{1/2}$ layer yields the tearing mode growth rate

$$\gamma = \frac{\Delta'_k}{2\mu_0 \sigma^{G-Z} \Delta_e}, \quad (5.15)$$

where the $\epsilon_e^{1/2}$ weighting factor of the conductivity (5.6) has been suppressed because the integration is performed in the Δ_e layer.

Using the pressure balance formula

$$n = \frac{B_{x0}^2}{2\mu_0} \frac{1}{T_i + T_e} \quad (5.16)$$

to determine the plasma density in terms of the lobe magnetic field strength, we find that the Galeev-Zelenyi conductivity formula (5.7) takes the form

$$\sigma^{G-Z} = \left(\frac{\pi}{2}\right)^{1/2} \frac{\omega_{cx0e}^2}{2\mu_0 \left(1 + \frac{T_i}{T_e}\right) kv_{the}^3} \quad (5.17)$$

and, substituting Eq. (5.17) into Eq. (5.15), we find that the collisionless tearing mode growth rate takes the form

$$\frac{\gamma}{\omega_{cx0e}} = \frac{2^{3/2}}{\pi^{1/2}} \left(1 + \frac{T_i}{T_e}\right) \epsilon_e^{5/2} (1 - k^2 L_z^2), \quad (5.18)$$

and the mode is unstable for $kL_z < 1$. For the reference parameters given in Table 1.1 the growth rate of the instability is $\gamma = 9.6 \times 10^{-5} \text{ sec}^{-1}$, and the growth time is $\tau \sim 1$ day. The observed growth phase of a substorm lasts 0.5 – 1 hr. Thus, this electron mechanism is not considered as plausible.

5.2 Collisionless Conductivity for Parabolic-Like Magnetic Field Reversals

In reality the magnetotail has a small component of the magnetic field normal to the current sheet layer, $B_z \ll B_{x0}$. The B_z component magnetizes the electrons, which perform gyromotion around B_z in the current sheet layer, and thus the main contribution to the low-frequency dissipative part of the conductivity is due to the unmagnetized ions. This is the principle of the plasma ion-diode [Golden *et al.*, 1977 and 1981], where the perpendicular magnetic field in the diode is adjusted to magnetize the electrons ($\epsilon_e \ll 1$), leaving the ions,

with $\epsilon_i \gtrsim 1$, to carry the current in the diode. Ion diodes are used for the generation and propagation of intense ion beams [Dreike *et al.*, 1976].

In parabolic-like magnetic field reversals with $B_z \ll B_{x0}$, ion motion may become chaotic. Chaotic particle motion is due to the continuous mixing of orbital frequencies, which leads to a continuous broad band power spectrum and to the decay of the velocity correlations. That is, chaotic particle motion smears the resonance peaks at the orbital frequencies, thus allowing the exchange of energy between particles and waves for a continuum of frequencies.

The conductivity formula can be motivated if we follow the picture of *Lyons and Speiser* [1985]. The main pickup of energy from $v_y E_y$ occurs when the particles are in the $\Delta_i \equiv (\rho_i L_z)^{1/2}$ layer and when $\omega_{cz} < \omega_{bz}$. In this regime the orbits enter into the Δ_i layer, make rapid north-south oscillations, make a large section of approximately one-half of the cyclotron orbit around B_z , and then escape to the lobes. Particles are coherently accelerated by E_y when they are in the Δ_i layer. Taking the residence or correlation time in the layer to be on the order of one-half of the cyclotron period, π/ω_{cz} , the low-frequency conductivity is given by the *Lyons-Speiser* formula

$$\sigma^{L-S} = \frac{n_0 q^2}{m} \frac{\pi}{|\omega_{cz}|}. \quad (5.19)$$

Horton and Tajima [1990,1991a] noted that the conductivity (5.19) acquires its value only in the Δ_i layer and thus the height-integrated conductivity for the current sheet is given by

$$\sigma^{H-T} = \epsilon^{1/2} \sigma^{L-S}. \quad (5.20)$$

Formula (5.20) has the important property that as m/e (or the gyroradius) vanishes so that the particles are tied to the field lines, the conductivity vanishes.

This is in contrast to Eq. (5.19) where σ is independent of m/e .

When the period $\Delta t \equiv \pi/|\omega_{cz}|$ is shorter than the streaming time $1/kv_{th}$, the cyclotron frequency at $z = 0$ determines the correlation time and the conductivity, rather than the phase mixing rate kv_{th} . Combining the characteristics given above we obtain the conductivity formula

$$\begin{aligned}\sigma^{H-T} &= \frac{nq^2}{m} \frac{\epsilon^{1/2}}{c_1|\omega_{cz}| + c_2|k|v_{th}} \\ &= \frac{nq^2}{m|\omega_{cx0}|} \frac{\epsilon^{1/2}}{c_1 b_z + c_2|k|\rho},\end{aligned}\quad (5.21)$$

where c_1 and c_2 are constants of order unity which are determined by the simulations. Note that in the limit that $\epsilon = \rho/L_z \rightarrow 0$, the particle motion becomes strictly adiabatic, executing only $\mathbf{E} \times \mathbf{B}$ drift motion, and the low-frequency conductivity (5.21) and the mobility vanish. Note also that for long wavelengths, $kv_{th} \lesssim \omega_{cz}$, the conductivity (5.21) reduces to the Lyons-Speiser conductivity (5.19) in the Δ_i layer.

The variation of the conductivity (5.21) with ϵ , b_z , and kL_z has been tested [Horton and Tajima, 1991a] by numerically computing the conductivity given by $\langle J_y E_y \rangle / \langle E_y^2 \rangle$. Good agreement with Eq. (5.21) has been obtained with $c_1 \approx 10$ and $c_2 \approx 2$. The relatively large value of the ratio c_1/c_2 implies that the Speiser and the chaotic orbits are more effective than the phase mixing from the Landau resonance at $v = \omega/k$ in determining the low-frequency conductivity.

Outside the Δ_i layer the particles are magnetized and the current is given by the polarization current

$$J_y = \frac{nq^2}{m\omega_{cx}^2} \frac{dE_y}{dt}, \quad (5.22)$$

which is completely reversible or reactive and does not contribute to the time-averaged $\langle J_y E_y \rangle$ and thus not to the time-averaged conductivity.

The reconnection growth rate obtained from the substitution of (5.21) into (5.15) is given by

$$\frac{\gamma}{|\omega_{cx0}|} = \epsilon^{3/2} \frac{c_1 b_z + c_2 k L_z \epsilon}{k L_z} \left(1 + \frac{T_e}{T_i} \right). \quad (5.23)$$

Thus the widely used collisionless ion tearing mode growth rate $\gamma^{G-Z} = |\omega_{cx0}| \epsilon^{5/2}$ of Galeev and Zelenyi [1976] increases to $\gamma = c_1 b_z |\omega_{cx0}| \epsilon^{3/2}$, due to the lower value of the conductivity (5.21). For $k L_z \gg c_1 b_z / c_2 \epsilon$ the growth rate reduces to the Galeev-Zelenyi value

$$\frac{\gamma^{G-Z}}{|\omega_{cx0}|} \approx c_2 \epsilon^{5/2} \quad (5.24)$$

with $1/\gamma^{G-Z} \sim 1$ hour. For $k L_z \gtrsim b_z$ the growth rate is increased to

$$\frac{\gamma}{|\omega_{cx0}|} \approx c_1 \epsilon^{3/2} \quad (5.25)$$

with $1/\gamma \sim 1$ min.

For the reference parameters of Table 1.1 and for $k L_x = 0.5$ the correlation time is

$$\tau_c = \frac{\epsilon^{1/2} |\omega_{cx0}|^{-1}}{c_1 b_z + c_2 k \rho} = 0.15 \text{ sec}, \quad (5.26)$$

the unmagnetized layer half-width is $\Delta_i = (\rho_i L_z)^{1/2} = 980$ km, the conductivity is $\sigma^{H-T} = 1.2 \times 10^{-6}$ mho/m, the growth rate is $\gamma = 0.9 \text{ min}^{-1}$, and the growth time is $\tau_\gamma \equiv 2\pi/\gamma = 7$ min.

5.3 Collisionless Conductivity for Sheared Parabolic Magnetic Field Reversals

The main effect of adding a constant cross-tail magnetic field component B_y to a parabolic-like magnetic field reversal is to introduce a tilt on the field lines away from the meridian. The tilt on the field lines increases the effective field line length in the quasineutral layer and, because of the tendency of the particles to follow the magnetic field lines, the particles remain for longer times in the Δ_i layer with a consequent increase in the mobility. Here we derive an approximate formula for comparison with the simulations.

In the presence of B_y it is convenient to write the y -component of the velocity in the following way:

$$\begin{aligned} v_y(t) &= v_{\parallel y}(t) + v_{\perp y}(t) \\ &= v_{\parallel}(t) \left(\frac{B_y}{B} \right) + v_{\perp y}(t), \end{aligned} \quad (5.27)$$

where $v_{\parallel y}$ is the projection along the y -axis of the component of the velocity parallel to the magnetic field, and $v_{\perp y}(t)$ is the y -component of the perpendicular component of the velocity.

From (5.27) we have that the dawn-dusk component of the velocity correlation function can be written as

$$C_{yy}(\tau) = C_{\parallel y}(\tau) + C_{\perp y}(\tau) + C_{\parallel, \perp}(\tau), \quad (5.28)$$

where $C_{\parallel y}(\tau)$ and $C_{\perp y}(\tau)$ are the correlation functions for $v_{\parallel y}$ and $v_{\perp y}$, respectively, and $C_{\parallel, \perp}(\tau)$ is the mixed correlation function

$$C_{\parallel, \perp}(\tau) = \lim_{T \rightarrow \infty} \int_{-T/2}^{T/2} \frac{dt}{T} (v_{\parallel y}(t)v_{\perp y}(t - \tau) + v_{\parallel y}(t - \tau)v_{\perp y}(t)). \quad (5.29)$$

Since the mixed correlation function of Eq. (5.29) is the time-averaged product of the fast varying $v_{\perp y}(t)$ and the smoothly varying $v_{\parallel y}(t)$, which averages to a small value, we will neglect the term $C_{\parallel, \perp}(\tau)$ in Eq. (5.28).

Thus the dc part of the electrical conductivity can be written as

$$\sigma_{yy} = \frac{nq^2}{m} (\tau_{c\parallel y} + \tau_{c\perp y}), \quad (5.30)$$

where the correlation time associated with $v_{\parallel y}$ is given by

$$\tau_{c\parallel y} = \frac{1}{2v_{th}^2} \left\langle \int_{-\infty}^{\infty} d\tau C_{\parallel y}(\tau) \right\rangle \quad (5.31)$$

and where $\tau_{c\perp y}$ is defined as

$$\tau_{c\perp y} = \frac{1}{2v_{th}^2} \left\langle \int_{-\infty}^{\infty} d\tau C_{\perp y}(\tau) \right\rangle. \quad (5.32)$$

Consider first the contribution to the conductivity from the parallel component of the motion. From (5.31) we have that

$$\begin{aligned} \tau_{c\parallel y}(\tau) &= \frac{1}{2v_{th}^2} \left\langle \int_{-\infty}^{\infty} d\tau \int_{-T/2}^{T/2} \frac{dt}{T} v_{\parallel}(t) v_{\parallel}(t - \tau) \left(\frac{B_y}{B} \right)^2 \right\rangle \\ &\approx \frac{1}{2v_{th}^2} \left\langle \int_{-\infty}^{\infty} d\tau C_{\parallel}(\tau) \right\rangle \left(\frac{B_y}{B} \right)_{rl}^2 \\ &= \left(\frac{B_y}{B} \right)_{rl}^2 \tau_{c\parallel}, \end{aligned} \quad (5.33)$$

where $(B_y/B)_{rl}$ is the average value of (B_y/B) in the Δ_i layer,

$$\left(\frac{B_y}{B} \right)_{rl}^2 = \int_{-\Delta_i}^{\Delta_i} \frac{dz}{2\Delta_i} \left(\frac{B_y}{B(z)} \right)^2. \quad (5.34)$$

Approximating $(B_y/B(z))_{rl}$ by its value at $z = \Delta_i$ we obtain

$$\left(\frac{B_y}{B} \right)_{rl}^2 = \frac{b_y^2}{b_y^2 + b_z^2 + \epsilon_i}. \quad (5.35)$$

Similarly, we can approximate $\tau_{c\parallel}$ by

$$\tau_{c\parallel} \approx \frac{l}{v_{th}}, \quad (5.36)$$

where l is the effective field line length within the Δ_i layer,

$$\begin{aligned} l &= \int_{-\Delta_i}^{\Delta_i} dz \frac{B(z)}{B_z} \\ &\approx 2\Delta_i \frac{B(\Delta_i)}{B_z} \\ &= 2\Delta_i \left(\frac{b_y^2 + b_z^2 + \epsilon_i}{b_z^2} \right)^{1/2}. \end{aligned} \quad (5.37)$$

Substituting (5.35)-(5.37) into (5.33) and substituting the result into (5.30) we find that the contribution to the conductivity from the parallel component of the motion is given by

$$\sigma_{\parallel} = \frac{nq^2}{m} \frac{\kappa}{\omega_{bz}} \left(\frac{b_y}{b_z} \right)^2 \epsilon^{1/2}, \quad (5.38)$$

where we have used the definition $\kappa = b_z/\epsilon^{1/2}$ and where we have taken into account that the dissipative part of the low-frequency conductivity is nonnegligible only inside the Δ_i layer.

The contribution from the perpendicular component of the motion to the low-frequency conductivity can be approximated by the Lyons-Speiser conductivity (5.19) with the reduction factor $\epsilon^{1/2}$. That is,

$$\sigma_{\perp} = \frac{nq^2}{m|\omega_{cz}|} \epsilon^{1/2}. \quad (5.39)$$

Substituting Eq. (5.38) and Eq. (5.39) into Eq. (5.30) we find that the low-frequency conductivity can be approximated as

$$\sigma = \frac{nq^2}{m|\omega_{cz}|} \left[a_1 + a_2 \kappa^2 \left(\frac{b_y}{b_z} \right)^2 \right] \epsilon^{1/2}, \quad (5.40)$$

Table 5.1: Sensitivity of Numerical Results to Changes in the Integration Parameters

Numerical Parameters $N, T, \Delta t$	$\langle \tilde{C}(\omega_{\min}) \rangle$
1000, 600, 0.2	0.38
500, 600, 0.2	0.39
500, 600, 0.1	0.36
500, 600, 0.05	0.36
500, 1200, 0.2	0.40
500, 1200, 0.1	0.38

where a_1 and a_2 are numerical constants to be determined from the simulations.

Fig. 5.3 is a plot of the correlation time τ_c as a function of b_y/b_z for $b_z = 0.05$, $\omega = \omega_{\min}$, $\kappa = 0.18$, and $\epsilon = 0.08$. Fig. 5.3 was generated with the magnetic field model of Eq. (2.126) for a total integration time $T = 600\omega_{b_z}^{-1}$ (≈ 20 min), a time step $dt = 0.3\omega_{b_z}^{-1}$ (≈ 0.6 s), and the total number of particles $N = 1000$. From the parabolic fitting of our numerical data we have $a_1 \approx 0.1$ and $a_2 \approx 0.6$. In Table 5.1 we illustrate the negligible sensitivity of our numerical results to changes in the total number of particles N , the total integration time T , and the time step by considering the variations in the value of $\langle \tilde{C}(\omega_{\min}) \rangle$ for fixed $\kappa = 0.18$, $b_y = 0.1$, and $b_z = 0.05$.

Table 5.2 displays numerical data for the *dc* part of the power spectrum, $\langle \tilde{C}(\omega = 0) \rangle$, corresponding to three values of κ_i : $\kappa_1 = 0.09$, $\kappa_2 = 0.18$,

$$\omega_{b_z} \tau_c = \frac{\epsilon^{1/2}}{\kappa} \left[a_1 + a_2 \kappa^2 \left(\frac{b_y}{b_z} \right)^2 \right]$$

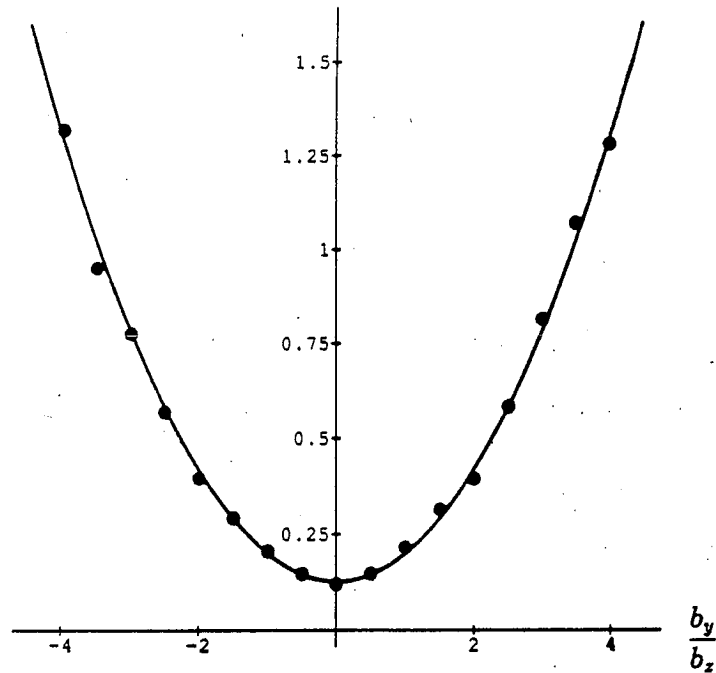


Figure 5.3: Plot of $\tau_c(\omega; \kappa, b_y, b_z, \epsilon)$ as a function of b_y/b_z . We obtained the plot by evaluating $\tilde{C}(\omega = \omega_{min})$ for different values of b_y keeping $b_z = 0.05$ and $\kappa = 0.18$ fixed. The points correspond to our numerical results and the solid curve represents the best fitting parabola. The values of the weighting factors are $a_1 \approx 0.1$ and $a_2 \approx 0.6$.

and $\kappa_3 = 0.36$. The purpose of Table 5.2 is to check the validity of the new conductivity formula (5.40)

In the case with no cross-tail magnetic field, Eq. (5.40) reduces to the z -averaged Lyons-Speiser conductivity formula (5.39). However, for $b_y \neq 0$ the conductivity formula opens a whole new range of interesting regimes.

From (5.40) we can find a critical value of the cross-tail parameter, b_{yc} , such that for $b_y > b_{yc}$ the longitudinal conductivity from parallel streaming along the tilted magnetic field dominates over the Speiser orbit cross-field conductivity. Equating the longitudinal and perpendicular contributions in (5.40) we get the critical b_{yc} value

$$b_{yc} = \left(\frac{a_1}{a_2}\right)^{1/2} \frac{b_z}{\kappa} = \left(\frac{a_1}{a_2}\right)^{1/2} \epsilon^{1/2}, \quad (5.41)$$

which for our simulation reference parameters is $b_{yc} = 2.27$.

Comparing b_{yc} for the ions and the electrons,

$$b_{yce} = \left(\frac{\kappa_i}{\kappa_e}\right) b_{yci} = \left(\frac{\rho_e}{\rho_i}\right)^{1/2} b_{yci}, \quad (5.42)$$

we see that for the electrons the longitudinal conductivity dominates over the perpendicular component for small values of the cross-tail parameter b_y . This B_y -dependent effect opens the possibility of stabilizing the collisionless tearing modes with increasing values of B_y .

Noting that the coefficient $n_0 q^2 / (m |\omega_{cz}|)$ in Eq. (5.40) is the same for the electrons as for the ions, we can compare the ion and electron conductivities;

$$\frac{\sigma_i}{\sigma_e} = \left(\frac{\epsilon_i}{\epsilon_e}\right)^{1/2} \frac{a_1 + a_2 \kappa_i^2 (b_y/b_z)^2}{a_1 + a_2 \kappa_e^2 (b_y/b_z)^2} = \left(\frac{\kappa_e}{\kappa_i}\right) \frac{a_1 + a_2 \kappa_i^2 (b_y/b_z)^2}{a_1 + a_2 \kappa_e^2 (b_y/b_z)^2}. \quad (5.43)$$

Table 5.2: Low Frequency Limit of Correlation Time

B_y/B_x	$\langle \bar{C}(\omega = 0; \kappa_1 = 0.09) \rangle$	$\langle \bar{C}(\omega = 0; \kappa_2 = 0.18) \rangle$	$\langle \bar{C}(\omega = 0; \kappa_3 = 0.36) \rangle$	$\langle \bar{C}(\omega = 0, \kappa_2) \rangle$	$\langle \bar{C}(\omega = 0, \kappa_1) \rangle$	$\langle \bar{C}(\omega = 0, \kappa_3) \rangle$
0.0	0.483	0.106	0.027	—0—	—0—	—0—
0.5	0.991	0.560	0.442	0.9	0.9	0.9
1.0	2.693	1.835	1.482	0.8	0.8	0.8
1.5	5.463	3.891	2.127	0.8	0.8	0.6
2.0	9.208	6.648	5.016	0.8	0.8	0.8
2.5	13.840	9.261	7.446	0.7	0.7	0.8
3.0	19.610	11.987	11.017	0.6	0.6	0.9

In particular, we can find a second critical value for the cross-tail magnetic field parameter, b_{yie} , for which σ_i and σ_e coincide. This value is given by

$$b_{yie} = \left(\frac{a_1}{a_2}\right)^{1/2} \left(\frac{1}{\kappa_i \kappa_e}\right)^{1/2} b_z. \quad (5.44)$$

For $|b_y|/b_{yie} > 1$ the electron conductivity is larger than the ion conductivity; on the other hand, if $|b_y|/b_{yie} < 1$, then the electron conductivity is smaller than the ion conductivity.

Assume, for example, that $T_e = T_i/10$ and that $\kappa_i = 0.18$. In this case, we have $\kappa_e = (\rho_i/\rho_e)^{1/2} \kappa_i = 2.1$, $b_{yce} = 0.2 b_z$, $b_{yie} = 0.7 b_z$, and $b_{yci} = 2.6 b_z$. So we have that as soon as the dawn-dusk magnetic field is turned on, the electron conductivity starts playing a very important role.

Fig. 5.4 is a plot of σ_i and σ_e as a function of b_y for fixed b_z . The solid portions of the curves represent the σ_{\perp} -dominated phase and the dashed portions of the curves represent the σ_{\parallel} -dominated phase.

We can obtain an estimate of the effect of B_y on the growth rate γ of the tearing modes by integrating Ampère's law in the Δ_i layer and assuming that the solution is approximately constant ($\delta A_y(z) \approx \delta A_y(0)$) in that layer. Thus we have that

$$\begin{aligned} \Delta'_k \delta A_y(0) &= -\mu_0 \int_{-\Delta_i}^{\Delta_i} J_y dz = -\mu_0 \left\{ \int_{-\Delta_i}^{\Delta_i} \sigma_i \delta E_y dz + \int_{-\Delta_e}^{\Delta_e} \sigma_e \delta E_y dz \right\} \\ &\approx 2\mu_0 \gamma \Delta_i \left[\sigma_i + \left(\frac{\rho_e}{\rho_i}\right)^{1/2} \sigma_e \right] \delta A_y(0), \end{aligned} \quad (5.45)$$

where we have taken into account that the electron conductivity σ_e acquires its value only in the small region $|z| < \Delta_e$.

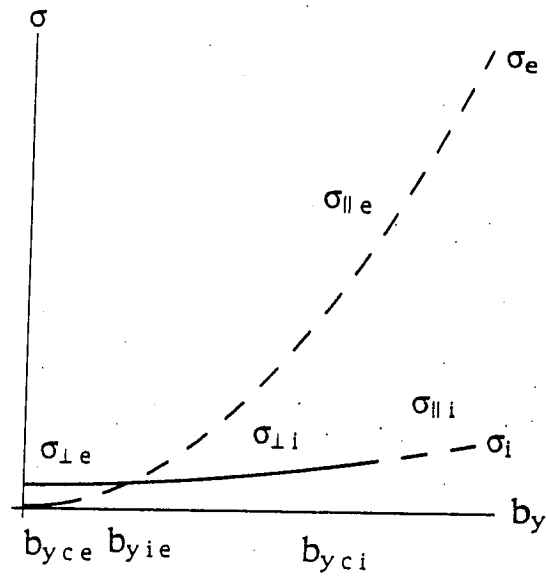


Figure 5.4: Qualitative behavior of the conductivity of Eq. (5.40) for both ions and electrons. The solid (dashed) portions of the curves are the σ_{\perp} (σ_{\parallel})-dominated parts of the conductivity. The critical values b_{yce} , b_{yie} , and b_{yic} are obtained by setting $\sigma_{\perp e} = \sigma_{\parallel e}$, $\sigma_e = \sigma_i$, and $\sigma_{\perp i} = \sigma_{\parallel i}$, respectively.

Suppressing the $\epsilon^{1/2}$ -factor in Eq. (5.40), since we are considering the contribution from the inner layer, we have that

$$\sigma_i + \left(\frac{\rho_e}{\rho_i}\right)^{1/2} \sigma_e \approx \frac{n_0 q^2}{m |\omega_{cz}|} \left[a_1 + a_2 \kappa_i \kappa_e \left(\frac{b_y}{b_z}\right)^2 \right], \quad (5.46)$$

and substituting (5.46) into (5.45) we get the growth rate

$$\gamma = \frac{m |\omega_{cz}|}{2\mu_0 n_0 q^2} \frac{\Delta'_k}{\Delta_i [a_1 + a_2 \kappa_i \kappa_e (b_y/b_z)^2]}. \quad (5.47)$$

Furthermore, taking

$$n_0 = \frac{B_{x0}^2}{2\mu_0 (T_i + T_e)}, \quad (5.48)$$

and substituting into (5.47), we obtain for the growth rate

$$\frac{\gamma}{\omega_{cx0}} = b_z \left(\frac{\rho_i}{L_z}\right)^{3/2} \left(1 + \frac{T_e}{T_i}\right) \frac{L \Delta'_k}{a_1 + a_2 \kappa_i \kappa_e (b_y/b_z)^2}, \quad (5.49)$$

where the stabilizing effect of the electrons when $B_y \neq 0$ is evident.

The values of τ_e , σ , γ , and the tearing mode growth rate time τ_γ for the different conductivity formulae are summarized in Table 5.3. We obtain these results with the use of the reference parameters of Table 1.1 and taking $B_y = B_z$ for (5.40). The results obtained from the Horton-Tajima conductivity (5.20) and from (5.40) are consistent with the substorm time scales.

The effect of a magnetic shear on the current sheet stability has been considered by several authors. *Drake and Lee* [1977] showed the destabilizing effect of a magnetic shear in the absence of a normal magnetic field component. *Wang et al.* [1990] generalized the results of *Drake and Lee* [1977] for the case of a sheared magnetic field reversal and very small normal magnetic field. *Büchner et al.* [1991] showed that a shear of the tail magnetic field may cause a tail tearing mode instability even for realistically large values of the

Table 5.3: Correlation time τ_c , conductivity σ , tearing mode growth rate γ , and growth time τ_r for the different conductivity formulae

Conductivity	τ_c	σ (mho/m)	γ (min ⁻¹)	τ_r
Spitzer (electron)	1 year	10^6	6×10^{-7}	20 years
Galeev-Zelenyi (396)	10^{-3} s	10^{-5}	6×10^{-3}	1 day
Horton-Tajima (410)	0.15 s	10^{-6}	0.9	7 min
Hernández <i>et al.</i> (429)	0.7 s	6×10^{-6}	0.4	16 min

normal magnetic field B_z . The reduction of the tearing mode growth rates with increasing values of B_y , as shown in Eq. (5.49), has been observed in the numerical simulations of *Tajima* [1981].

5.4 Results of Parametric Studies to Verify the $B_y - \kappa$ Dependence of the Mobility Formula

In order to check the validity of the mobility formula (5.40) as a function of the κ -parameter, consider Table 5.2. This table shows numerical data for the dc part of the power spectrum, $\langle \tilde{C}(\omega = 0, \kappa_i, b_y, b_z) \rangle$, for different values of the parameter b_y with $b_z = 0.05 = \text{const.}$, and for three different values of κ_i :

$$\kappa_1 = 0.09, \kappa_2 = 0.18, \kappa_3 = 0.36. \quad (5.50)$$

In the conductivity formula (5.40), the contribution to the time τ_c from the component of the motion perpendicular to the magnetic field $\tau_{c\perp}$ is given by

$$\tau_{c\perp} = a_1 \frac{\epsilon^{1/2}}{\kappa} = a_1 \frac{b_z}{\kappa^2}, \quad (5.51)$$

and the contribution from the parallel motion is given by

$$\tau_{c\parallel} = a_2 \epsilon^{1/2} \kappa \left(\frac{b_y}{b_z} \right)^2 = a_2 \frac{b_y^2}{b_z}. \quad (5.52)$$

With the use of Table 5.2 we can check, for fixed $b_z = 0.05$, the κ^{-2} scaling of $\tau_{c\perp}$ and the independence of $\tau_{c\parallel}$ on κ . In particular, from (5.51) we must have

$$\frac{\tau_{c\perp}(\kappa_3 = 0.36)}{\tau_{c\perp}(\kappa_2 = 0.18)} = \frac{\tau_{c\perp}(\kappa_2 = 0.18)}{\tau_{c\perp}(\kappa_1 = 0.09)} = \frac{1}{4}; \quad (5.53)$$

and from (5.52) and keeping $b_z = \text{const.}$ we must have

$$\frac{\tau_{c\parallel}(\kappa_3, b_y)}{\tau_{c\parallel}(\kappa_2, b_y)} = \frac{\tau_{c\parallel}(\kappa_2, b_y)}{\tau_{c\parallel}(\kappa_1, b_y)} = 1. \quad (5.54)$$

We can verify Eq. (5.53) by noting that $\tau_c(\kappa, b_y)$ is proportional to $\langle \tilde{C}(\omega = 0, \kappa, b_y) \rangle$ and thus the relationships

$$\frac{\tau_{c\perp}(\kappa_3)}{\tau_{c\perp}(\kappa_2)} = \frac{\langle \tilde{C}_{\perp}(\omega = 0; \kappa_3) \rangle}{\langle \tilde{C}_{\perp}(\omega = 0; \kappa_2) \rangle}, \quad (5.55)$$

and

$$\frac{\tau_{c\perp}(\kappa_2)}{\tau_{c\perp}(\kappa_1)} = \frac{\langle \tilde{C}_{\perp}(\omega = 0; \kappa_2) \rangle}{\langle \tilde{C}_{\perp}(\omega = 0; \kappa_1) \rangle}, \quad (5.56)$$

must hold. From the data in Table 5.2 we have

$$\frac{\langle \tilde{C}_{\perp}(\omega = 0; \kappa_3) \rangle}{\langle \tilde{C}_{\perp}(\omega = 0; \kappa_2) \rangle} = \frac{0.027}{0.106} = 0.255, \quad (5.57)$$

and

$$\frac{\langle \tilde{C}_{\perp}(\omega = 0; \kappa_2) \rangle}{\langle \tilde{C}_{\perp}(\omega = 0; \kappa_1) \rangle} = \frac{0.106}{0.483} = 0.219, \quad (5.58)$$

which are in excellent agreement with (5.53).

In order to verify (5.54) we note that

$$\langle \tilde{C}_{\parallel}(\omega = 0; \kappa_i, b_y) \rangle = \langle \tilde{C}(\omega = 0; \kappa_i, b_y) \rangle - \langle \tilde{C}_{\perp}(\omega = 0; \kappa_i) \rangle \quad (5.59)$$

and thus

$$\frac{\langle \tilde{C}_{\parallel}(\omega = 0; \kappa_3, b_y) \rangle}{\langle \tilde{C}_{\parallel}(\omega = 0; \kappa_2, b_y) \rangle} = \frac{\langle \tilde{C}_{\parallel}(\omega = 0; \kappa_2, b_y) \rangle}{\langle \tilde{C}_{\parallel}(\omega = 0; \kappa_1, b_y) \rangle} = 1 \quad (5.60)$$

must hold. From the last two columns of Table 5.2 we observe that the values are slightly less than unity, probably because of the approximations made in the derivation of the mobility formula (5.40).

Chapter 6

Chapter 6. Conclusions and Discussion

The current sheet of the central plasma sheet in the geomagnetic tail is an important region for the storage and release of plasma and energy. In order to explain magnetic reconnection in the central plasma sheet, it is necessary to have a finite electrical conductivity. The value of this conductivity should be anomalously low to be consistent with substorm time scales. However, the geomagnetic tail is a highly collisionless environment and turbulent wave activity is negligible at the center of the current sheet. Thus, it is necessary to find another source of dissipation.

We have shown that the finite collisionless conductivity in the current sheet of the central plasma sheet is due to the decay of the velocity correlations produced by chaotic particle motion. In particular, for tail-like magnetic field reversals the velocity correlations exhibit a power law decay, which is similar to the power law decay of the velocity correlations in a molecular Lorentz gas.

We have developed, from linearized Vlasov theory, a physically motivated, direct, and flexible formalism for the calculation of the dissipative part of the conductivity: the spectral velocity correlations (SVC) formalism. The formalism is equivalent to inferring the dielectric properties of a medium from the observation of the absorption lines in the spectrum. For systems in thermodynamic equilibrium the SVC formalism is reduced to the well known Kubo conductivity formula.

An important property of the SVC formalism is that it is particularly useful in situations where the charged particle motion is a mixture of both chaotic and integrable motion. Another advantage of the SVC formalism is that we are able to calculate directly the dissipative linear conductivity. This must be contrasted with the earlier work of *Doxas et al.* [1990] and *Horton and Tajima* [1991a]. In these works, the conductivity is estimated through the calculation of irreversible heating rates from the perturbed orbits in the actual electric field, which necessarily has finite amplitude.

We also discuss and test numerically the frequency-sum rule, which dictates that the total amount of power absorbed by the medium over all frequencies is constant depending only on the plasma density and being independent of the particular inhomogeneous magnetic field. For integrable motion, such as the motion in the presence of a constant magnetic field, all the power is absorbed at the resonances. However, for chaotic motion the power is absorbed over a continuum of frequencies. The broad band of absorption frequencies for the plasma sheet is in direct contrast with the conductivity in the lobe plasma and in the near-Earth magnetosphere, where the drift-cyclotron orbits produce sharp absorption lines.

In the SVC formalism the effective collisional time τ_c is proportional to $\langle \tilde{C}(k, \omega; \mathbf{X}_0) \rangle$, where $\tilde{C}(k, \omega; \mathbf{X}_0)$ is the single particle velocity power spectrum for a particle with initial conditions $\mathbf{X}_0 = (\mathbf{x}_0, \mathbf{v}_0)$, and $\langle \dots \rangle$ denotes average over the ensemble of particles. In systems where chaotic and integrable motion coexist, the broad bandwidth structure of $\langle \tilde{C}(k, \omega; \mathbf{X}_0) \rangle$ has contributions from both phase mixing (Landau damping) and the broad band structure of the single particle power spectrum for chaotic orbits.

We have derived explicit expressions for the low frequency conductivity in both parabolic and sheared parabolic magnetic field reversals. We have computed the conductivity in mho/m and used the resulting values to estimate the growth rates of linear tearing modes. The values obtained for the growth times (~ 5 min) of linear tearing modes are consistent with the measured substorm time scales.

Earlier studies of collisionless energization processes in parabolic-like magnetic field reversals give: (a) the Galeev-Zelenyi (GZ) conductivity formula [Galeev and Zelenyi, 1976], and (b) the Lyons-Speiser (LS) conductivity formula [Lyons and Speiser, 1985]. In the GZ model the particles are treated as unmagnetized in the $\Delta_s = (\rho_s L_z)^{1/2}$ layer. The GZ conductivity arises from the phase mixing, produced by the spread of the velocity $\Delta v_x = v_{th}$, in the collisionless Landau resonance of Eq. (5.3). The GZ conductivity is proportional to the phase mixing rate $(|k|v_{th})^{-1}$. On the other hand, the LS conductivity is based on the acceleration of the transient-type orbits in the dawn-dusk electric field. The LS conductivity is proportional to the time that the transient orbits spend in the neutral sheet and the residence time is approximated by $\pi/|\omega_{cz}|$. Here we have calculated the conductivity in detail, including all the orbits in local Maxwellian distributions filling the magnetotail flux tubes. Our conductivity formulae are given in Eqs. (5.21) and (5.40). Typical values for the conductivity and for the associated growth rate of linear tearing modes are given in Table (5.3).

Our parametric studies show that the space-time-averaged conductivity formula varies inversely with b_z , as expected from the LS formula. However, we show that the averaged conductivity drops strongly because of the short

correlation time from the chaotic orbits. We also show that the LS formula misses the finite gyroradius $\epsilon_s = \rho_s/L_z$ dependence of the averaged conductivity, $\sigma \sim \epsilon_s^{1/2}/b_z$, describing the fact that the low-frequency dissipation is negligible in the limit that the gyroradius vanishes. The new factor of $\epsilon_s^{1/2}$ is also critical for comparing the relative electron and ion current contributions when the B_y field is introduced.

The SVC formalism has been used to extend the conductivity formulae to new regimes. In particular, we consider the case of a sheared parabolic magnetic field reversal. In this case, we have shown that the conductivity has a new term which scales as $(B_y/B_z)^2$; that there is a critical value of B_y for which the contribution of the electrons to the conductivity becomes dominant; and that increasing values of B_y reduce the growth rate of linear tearing modes.

Our conductivity formulae can be used in resistive MHD simulations of magnetospheric dynamics. In fact, a magnetic Reynolds number $R_m = \mu_0 L_z v_a \sigma \sim 200$ is often used in the simulations [e.g., *Birn and Hesse, 1990*]. The value 200 is chosen to give the reconnection e-folding time on the order of a few minutes, as observed in magnetospheric substorms. If one computes R_m with the use of Eq. (5.40), one obtains $R_m \approx 100 - 300$, depending on the specific field and plasma parameters.

References

- Akasofu, S.-I., A.T.Y. Lui, C.I. Meng, and M. Haurwitz, Need for a three-dimensional analysis of magnetic fields in the magnetotail during substorms, *Geophys. Res. Lett.*, **5**, 283, 1978.
- Alder, B.J., and T.E. Wainwright, Decay of velocity autocorrelation function, *Phys. Rev. A*, **1**, 18, 1970.
- Anderson, R.R., Plasma waves at and near the neutral sheet, Proceedings of the Conference on Achievements of the IMS, *Eur. Space Agency Spec. Publ., ESA SP-217*, 199, 1984.
- Benettin, G., L. Galgani, and J-M Strelcyn, Kolmogorov Entropy and Numerical Experiments, *Phys. Rev. A*, **14**, 2338, 1976.
- Birn, J., R. Sommer, and K. Schindler, Open and closed magnetospheric tail configurations and their stability, *Astrophys. Space Sci.*, **35**, 389, 1975.
- Birn, J., Magnetotail equilibrium theory: The general three dimensional solution, *J. Geophys. Res.*, **92**, 11101, 1987.
- Birn, J., The distribution of the magnetotail equilibrium structure by a net cross-tail magnetic field, *J. Geophys. Res.*, **95**, 8019, 1990.
- Birn, J., and M. Hesse, The magnetic topology of the plasmoid flux rope in a MHD-simulation of magnetotail reconnection, in

- Physics of Magnetic Flux Ropes*, Geophys. Monogr. Ser., 58, 655, AGU, Washington, D.C., 1990.
- Büchner, J. and L.M. Zelenyi, Deterministic chaos in the dynamics of charged particles near a magnetic field reversal, *Phys. Lett. A.*, 92, 13,395, 1986.
- Büchner, J. and L.M. Zelenyi, Chaotization of the electron motion as the cause of an internal magnetotail instability and substorm onset, *J. Geophys. Res.*, 92, 13,456, 1987.
- Büchner, J. and L.M. Zelenyi, Regular and chaotic charged particle motion in magnetotail-like field reversals; 1. Basic theory of trapped motion, *J. Geophys. Res.*, 94, 11,821, 1989.
- Büchner, J. and L.M. Zelenyi, Regular and chaotic particle motion in sheared magnetic field reversals, *Adv. Space Res.*, 11, (9) 177, 1991.
- Büchner, J., M. Kusnetzova, and L.M. Zelenyi, Sheared field tearing mode instability and creation of flux ropes in the Earth magnetotail, *Geophys. Res. Lett.*, 18, 385, 1991.
- Burkhart, G.R., and J. Chen, Differential memory in the earth's magnetotail, *J. Geophys. Res.*, 96, 14,031, 1991.
- Burkhart, G.R., R.F. Martin, P.B. Dusenbery, and T.W. Speiser, Neutral line chaos and phase space structure, *Geophys. Res. Lett.*, 18; 1591, 1991.
- Cable, S., and T. Tajima, Low-frequency fluctuations in plasma magnetic fields, *Phys. Rev. A*, 46, 3413, 1992.

- Callen, H.B., and T.A. Welton, Irreversibility and generalized noise, *Phys. Rev.*, **83**, 34, 1951.
- Cattel, C.A., F.S. Mozer, E.W. Hones, Jr., R.R. Anderson, and R.D. Sharp, ISEE observations of the plasma sheet boundary, plasma sheet and neutral sheet, 1, electric field, magnetic field, plasma and ion composition, *J. Geophys. Res.*, **91**, 5663, 1986.
- Chen, J., Nonlinear dynamics of charged particles in the magnetotail, *J. Geophys. Res.*, **97**, 15,011, 1992.
- Chen, J. and P.J. Palmadesso, Chaos and nonlinear dynamics of single-particle orbits in a magnetotail-like magnetic field, *J. Geophys. Res.*, **91**, 1499, 1986.
- Chirikov, B.V., A universal instability of many-dimensional oscillator systems, *Phys. Rep.*, **52**, 263, 1979.
- Coppi, B., G. Laval, and R. Pellat, Dynamics of the geomagnetic tail, *Phys. Rev. Lett.*, **16**, 1207, 1966.
- Coroniti, F.V., On the tearing mode of quasineutral sheets, *J. Geophys. Res.*, **85**, 6719, 1980.
- Cowley, S.C., M. Kulsrud, and T.S. Hahm, Linear stability of tearing modes, *Phys. Fluids*, **29**, 3230, 1986.
- Cowley, S.W.H., Magnetospheric and ionospheric flow and the interplanetary magnetic field, in *The Physical Basis of the Ionosphere in the Solar-Terrestrial System*, pp.4.1-4.4, AGARD, Neuilly sur Seine, France, 1982.

- Dorfman, R., and E.G.D. Cohen, Velocity correlation functions in two and three dimensions, *Phys. Rev. Lett.*, **25**, 1257, 1970.
- Doxas, I., W. Horton, K. Sandusky, T. Tajima, and R. Steinfolson, Numerical study of the current sheet and plasma sheet boundary layer in a magnetotail model, *J. Geophys. Res.*, **95**, 12033, 1990.
- Drake, J.F., and Y.C. Lee, Kinetic theory of tearing instabilities, *Phys. Fluids*, **20**, 1341, 1977.
- Dreike, P.L., C. Eischenberger, S. Humphries, Jr., and R.N. Sudan, Production of intense proton fluxes in a magnetically insulated diode, *J. Appl. Phys.*, **47**, 2382, 1976.
- Dungey, J.W., Interplanetary magnetic field and the auroral zones, *Phys. Rev. Lett.*, **6**, 47, 1961.
- Dusenbery, P.B., and R.F. Martin, Single particle dynamics and chaos in current sheets, *Chaos*, 1994.
- Ernst, M.H., and A. Weyland, Long-time behavior of the velocity auto-correlation function in a Lorentz gas, *Phys. Lett.*, **34 A**, 39, 1971.
- Esarey, E., and K. Molvig, A turbulent mechanism for substorm onset in the earth's magnetotail, *Geophys. Res. Lett.*, **14**, 367, 1987.
- Fairfield, D.H., The average configuration of the geomagnetic tail, *J. Geophys. Res.*, **84**, 1950, 1979.
- Fano, R.M., L.J. Chiu, and R.B. Adler, *Electromagnetic Fields, Energy, and Forces*, Wiley, New York, NY, 1960.

- Furth, H.P., J. Killeen, and M.N. Rosenbluth, Finite resistive instabilities of a sheet pinch, *Phys. Fluids*, **6**, 459, 1963.
- Galeev, A.A., Spontaneous reconnection of magnetic field lines in a collisionless plasma, in *Handbook of Plasma Physics*, Vol. 2, ed. by M.N. Rosenbluth and R.Z. Sagdeev (North-Holland, New York, 1984), 305-335.
- Galeev, A.A. and L.M. Zelenyi, Tearing instability in plasma configurations, *Sov. Phys. JETP*, **43**, 1113, 1976.
- Golden, J., C.A. Kapetanacos, S.J. Marsh, and S.J. Stephanakis, Generation of 0.2-TW proton pulses, *Phys. Rev. Lett.*, **38**, 130, 1977.
- Golden, J., C.A. Kapetanacos, J.A. Pasour, and R.A. Mahaffey, The generation and application of intense pulsed ion beams, *Am. Sci.*, **69**, 130, 1981.
- Guckenheimer, J., and P. Holmes, *Nonlinear Oscillations, Dynamical Systems, and Bifurcations of Vector Fields*, p.25, Springer-Verlag, New York, NY, 1985.
- Harris, E.G., On a plasma sheath separating regions of oppositely directed magnetic field, *Nuovo Cim.*, **23**, 115, 1962.
- Hénon, M., and C. Heiles, The applicability of the third integral of motion, *Astron. J.*, **69**, 73, 1964.
- Hernández, J.V., W. Horton, and T. Tajima, Low-frequency mobility response functions for the central plasma sheet with ap-

- plications to tearing modes, *J. Geophys. Res.*, **98**, A4, 5893, 1993.
- Hones, E.W., Jr., Transient phenomena in the magnetotail and their relation to substorms, *Space Sci. Rev.*, **23**, 393, 1979.
- Horton, W. and T. Tajima, Decay of correlations and the collisionless conductivity in the geomagnetic tail, *Geophys. Res. Lett.*, **17**, 123, 1990.
- Horton, W. and T. Tajima, Collisionless conductivity and stochastic heating of the plasma sheet in the geomagnetic tail, *J. Geophys. Res.*, **96**, 15811, 1991a.
- Horton, W., and T. Tajima, Transport from chaotic orbits in the geomagnetic tail, *Geophys. Res. Lett.*, **18**, 1583, 1991b.
- Horton, W., J. Hernández, J.Y. Kim, and T. Tajima, Orbital stability, transport, and convective heating in the current sheet plasma, in *Physics of Space Plasmas* (1991), SPI Conference Proceedings and Reprint Series, Number II, T. Chang, G.B. Crew, and J.R., eds. (Scientific Publishers, Cambridge, MA, 1992).
- Horton, W., J.V. Hernández, T. Tajima, and A. Dykhne, Fluctuation dissipation relations for plasmas in strongly inhomogeneous magnetic fields, *Physica D*, **71**, 249, 1994.
- Huba, J.D., N.T. Gladd, and K. Papadopoulos, Lower hybrid drift wave turbulence in the distant magnetotail, *J. Geophys. Res.*, **83**, 5217, 1978.

- Ichimaru, S., *Statistical Plasma Physics*, Addison-Wesley Publishing Company, 1991.
- Karimabadi, H., P.L. Pritchett, and F.V. Coroniti, Particle orbits in two-dimensional equilibrium models for the magnetotail, *J. Geophys. Res.*, **95**, 17153, 1990.
- Kaufman, A.N., and T. Nakayama, Interaction of waves and particles in an inhomogeneous one-dimensional plasma, *Phys. Fluids*, **13**, 956, 1970.
- Kaufman, A.N., Resonant interaction between particles and normal modes in a cylindrical plasma, *Phys. Fluids*, **14**, 387, 1971.
- Klimontovich, Yu.L., *Turbulent Motion and the Structure of Chaos*, pp. 135-183, Kluwer Academic Publishers, Boston, Mass, 1991.
- Kubo, R., Statistical-mechanical theory of irreversible processes: 1, General theory and simple applications to magnetic conduction problems, *J. Phys. Soc. Japan*, **12**, 570, 1957.
- Kubo, R., M. Toda, and N. Hashitsume, *Statistical Physics II*, pp. 167-174, Springer-Verlag, New York, NY, 1985.
- Landau, L.D., and E.M. Lifshitz, *Electrodynamics of Continuous Media*, Pergamon Press, Oxford, 1960.
- Landau, L.D., and E.M. Lifshitz, *Statistical Physics*, Pergamon Press, Oxford, 1969.
- Lembege, B., and R. Pellat, Stability of a thick two-dimensional quasineutral sheet, *Phys. Fluids*, **25**, 1995, 1982.

- Lichtenberg, A.J., and M.A. Lieberman, *Regular and Stochastic Motion*, pp. 262-285, Springer-Verlag, New York, NY, 1982.
- Lui, A.T., A synthesis of magnetospheric substorm models, *J. Geophys. Res.*, **96**, A2, 1849, 1991.
- Lyons, L.R. and T.W. Speiser, Ohm's law for a current sheet, *J. Geophys. Res.*, **90**, 8543, 1985.
- Martin, R.F., Jr., Chaotic particle dynamics near a two-dimensional magnetic neutral point with applications to the geomagnetic tail, *J. Geophys. Res.*, **91**, 11,985, 1986.
- Morrison, P.J., The energy of perturbations for Vlasov plasmas, *Inst. for Fusion Studies Rep.*, IFSR 641, 1994.
- Sakurai, J.J., *Modern Quantum Mechanics*, p.236, Addison-Wesley Publishing Company, 1985.
- Schindler, K., A self-consistent theory of the tail of the magnetosphere, in *Earth's Magnetospheric Processes*, p. 200, B.M. McCormack and D. Reidel, eds., Hingham, Mass, 1972.
- Schram, P.P.J.M., *Kinetic Theory of Gases and Plasmas*, pp. 234-253, Kluwer Academic Publishers, 1991.
- Sitenko, A.G., *Fluctuations and Non-linear Wave Interaction in Plasmas*, Pergamon Press, Oxford, 1982.
- Speiser, T.W., Particle trajectories in model current sheets, 1, Analytical solutions, *J. Geophys. Res.*, **70**, 4219, 1963.
- Spitzer, L., *Physics of Fully Ionized Gases*, 2nd ed., Interscience publishers, New York, NY, 1962.

- Sonnerup, B.U.Ö., Adiabatic particle orbits in a magnetotail null sheet, *J. Geophys. Res.*, **76**, 8211, 1971.
- Swift, D.W., and C. Allen, Interaction of the plasma sheet with the lobes of the earth magnetotail, *J. Geophys. Res.*, **90**, 10,015, 1987.
- Stix, T.H., *Waves in Plasmas*, p.75, AIP, New York, NY, 1992.
- Tajima, T., Tearing and Reconnection, in *Fusion Energy 1981*, IAEA, B. Mac Namara, ed., Trieste, 1981.
- Tajima, T., S. Cable, K. Shibata, and R.M. Kulsrud, On the origin of cosmological magnetic fields, *The Astrophys. J.*, **390**, 1992.
- Tsurutani, B.T., and W.D. Gonzalez, The causes of geomagnetic storms during solar maximum, *EOS Trans. AGU*, **75**, 49, 1994.
- Wang, X., Bhattacharjee, A., and A.T.Y. Lui, Collisionless tearing instability in magnetotail plasmas, *J. Geophys. Res.*, **95**, 15047, 1990.
- Zwingmann, W., Self-consistent magnetotail theory: equilibrium structures including arbitrary variations along the tail axis, *J. Geophys. Res.*, **88**, 9101, 1983.

VITA

José Valente Hernández Ochoa was born in México, D.F., on June 6, 1963, the son of Arnulfo and Alicia Hernández. After graduating from the Colegio de Bachilleres High School, he went to Mexico's National Autonomous University (UNAM) where he completed his senior thesis under the guidance of Dr. Mariano Bauer and the kindly help of Dr. Julio Herrera. In October 1987 he graduated with a B.S. in Physics. The following fall he entered The University of Texas at Austin as a graduate student in physics with the generous financial support from UNAM. He was married to Verónica Hernández on January 7, 1989. He has been a research assistant to Prof. Wendell Horton since January 1991.

Permanent address: Cerrada del Estribo 10
Rincón Colonial
Atizapán, Edo. de México
CP 52996
México

This dissertation was typeset with \LaTeX by the author.